# Quantitative Measurement of pH in Stroke Using Chemical Exchange Saturation Transfer Magnetic Resonance Imaging

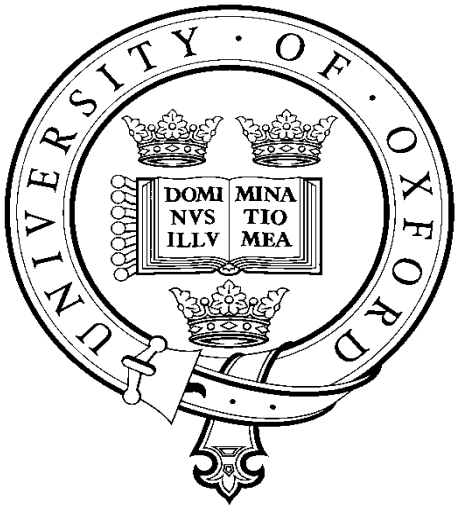


**Yee Kai Tee**

Wolfson College

Department of Engineering Science

Jointly supervised by
Dr Stephen Payne
Dr Michael Chappell

This dissertation is submitted in partial fulfilment of the requirements for the degree of Doctor of Philosophy at the University of Oxford

Submitted: Trinity Term 2013

# Quantitative Measurement of pH in Stroke Using Chemical Exchange Saturation Transfer Magnetic Resonance Imaging

**Yee Kai Tee** **Wolfson College**
**DPhil Thesis** **Trinity Term 2013**

## Abstract

Stroke is one of the leading causes of death and adult disability worldwide. The major therapeutic intervention for acute ischemic stroke is the administration of recombinant tissue plasminogen activator (rtPA) to help to restore blood flow to the brain. This has been shown to increase the survival rate and to reduce the disability of ischemic stroke patients. However, rtPA is associated with intracranial haemorrhage and thus its administration is currently limited to only about 5% of ischemic stroke patients. More advanced imaging techniques can be used to better stratify patients for the rtPA treatment.

One new imaging technique, chemical exchange saturation transfer (CEST) magnetic resonance imaging, can potentially image intracellular pH and since tissue acidification happens prior to cerebral infarction, CEST has the potential to predict ischemic injury and hence to improve patient selection. Despite this potential, most studies have generated pH-weighted rather than quantitative pH maps; the most widely used metric to quantify the CEST effect is only able to generate qualitative contrast measurements and suffers from many confounds. The greatest clinical benefit of CEST imaging lies in its ability to non-invasively measure quantitative pH values which may be useful to identify salvageable tissue.

The quantitative techniques and work presented in this thesis thus provide the necessary analysis to determine whether a threshold for the quantified CEST effect or for pH exists to help to define tissue outcome following stroke; to investigate the potential of CEST for clinical stroke imaging; and subsequently to facilitate clinical translation of CEST for acute stroke management.

# Acknowledgement

I would like to express my sincere gratitude to my supervisors, Dr. Stephen Payne and Dr. Michael Chappell, for their useful advice, kind support and encouragement throughout the DPhil period, leading to the submission of this thesis. It is hard to imagine what will happen without their valuable inputs to my DPhil research.

Dr Irwin Jacobs, founding chairman and ex-CEO of Qualcomm Incorporated, is the next person I would like to thank. Although he has not provided any insightful idea and useful discussion towards this work, his generosity in setting up the Qualcomm Scholarships has benefitted many and I am extremely lucky to be one of them. Without his kind financial support, studying for a DPhil degree at Oxford University is probably a dream to me. I would also like to thank Sloane-Robinson Foundation for giving me a scholarship to do an MSc at Oxford University because I would be financially handicapped without this award and thus not eligible for the DPhil scholarship.

Next, thank you Professor Alison Noble for accepting me into MSc in Biomedical Engineering course and subsequently CDT in Healthcare Innovation program, Dr Gari Clifford who is the current director of CDT and all the academic staff of the program. Without the excellent training in the first year, I might need extra months or years to acquire the skills required to conduct an independent research.

I would also like to acknowledge the help from Dr George Harston, Dr Alexandr Khrapichev, Dr Nicholas Blockley, Dr Nicola Sibson, Dr James Kennedy and Professor Peter Jezzard for developing the MRI sequences and collecting the data for me, Dr Heiko Schiffter for teaching me how to build pH phantoms, Dr Jingyi Xie for kindly sharing her arterial spin

labelling codes to me to kick start the project and everyone in the PUMMA and QUBIC research group, especially Dr Amit Mehndiratta, Dr Claire Lucas and Mr Chris Harrison.

Last but not least, I would like to thank my parents and girlfriend for their love and support. To each of these people, this is as much yours as it is mine.

!!**THANK YOU FOR EVERYTHING**!!

# Contents

**Abstract** ..... **i**

**Acknowledgement** ..... **ii**

**Contents** ..... **iv**

**Glossary** ..... **viii**

**List of Figures** ..... **xi**

**List of Tables** ..... **xviii**

**List of Publications** ..... **xix**

**Chapter 1: Introduction** ..... **1**

1.1 Stroke Statistics ..... 2

1.2 Pathophysiology of Stroke ..... 2

1.3 Stroke Treatment and its Challenges ..... 4

1.4 pH Imaging for Stroke ..... 5

1.5 Thesis Outline ..... 6

**Chapter 2: Basics of MRI and Literature Review of CEST Imaging** ..... **8**

2.1 Basics of MRI ..... 9

2.1.1 Spin and Precession ..... 9

2.1.2 Equilibrium Magnetization ..... 10

2.1.3 Radio Frequency (RF) Pulses ..... 10

2.1.4 Relaxation ..... 11

2.2 CEST Imaging ..... 12

2.2.1 CEST Mechanism ..... 12

2.2.2 Types of CEST Imaging ..... 14

2.2.3 The General Modified Bloch Equations ..... 19

2.2.4 Potential Clinical Applications of CEST Imaging ..... 21
2.2.5 CEST Imaging and pH ..... 24
2.2.6 APT Imaging as a Marker of Tissue pH ..... 24
2.2.7 APT Imaging for Clinical Stroke ..... 28
2.2.8 APT Quantification Methods ..... 30
2.3 Limitations of APT Quantification Methods ..... 34
2.3.1 Magnetic Field Strength ..... 34
2.3.2 $B_0$ and $B_1$ Field Inhomogeneity ..... 35
2.3.3 Inherent Asymmetry in the *In Vivo* Z-spectrum ..... 39
2.3.4 Physiological Changes after Stroke ..... 41
2.4 Summary ..... 43
**Chapter 3: Optimal Sampling Schedule for CEST ..... 44**
3.1 Introduction ..... 45
3.2 Theory ..... 47
3.2.1 Application of Optimal Design to CEST Imaging ..... 47
3.2.2 Quantification of CEST Effect for Model-based Analysis ..... 48
3.3 Materials and Methods ..... 49
3.3.1 Numerical Simulation ..... 49
3.3.2 *In Vitro* ..... 53
3.4 Results ..... 56
3.4.1 Numerical Simulation ..... 56
3.4.2 *In Vitro* ..... 58
3.5 Discussion ..... 62
3.6 Summary ..... 66

**Chapter 4: Evaluating the Use of a Continuous Approximation for Model-based Quantification of Pulsed CEST ..... 68**

4.1 Introduction ..... 69

4.2 Materials and Methods ..... 71

4.2.1 Numerical Simulation ..... 71

4.2.2 *In Vitro* ..... 73

4.3 Results ..... 76

4.3.1 Numerical Simulation ..... 76

4.3.2 *In Vitro* ..... 77

4.4 Discussion ..... 81

4.5 Summary ..... 86

**Chapter 5: Comparing Different Methods of Quantifying MRI APT Effect in Hyper-acute Stroke Patients ..... 87**

5.1 Introduction ..... 88

5.2 Theory ..... 90

5.2.1 Asymmetry Analysis ..... 90

5.2.2 Model-based Analysis ..... 91

5.3 Materials and Methods ..... 92

5.3.1 Subject Recruitment ..... 92

5.3.2 MRI Experiment ..... 93

5.3.3 Data Processing and Analysis ..... 94

5.3.4 Healthy Subjects ..... 97

5.3.5 Stroke Patients ..... 98

5.4 Results ..... 99

5.5 Discussion ..... 106

5.6 Summary ..... 112

**Chapter 6: Conclusions and Future Work ..... 113**

6.1 Conclusions ..... 114

6.2 Future Work ..... 117

6.2.1 NOE ..... 118

6.2.2 Tumour Detection ..... 120

**References ..... 124**

**Appendix ..... 136**

A1 2-pool Exchange Model ..... 136

A2 3-pool Exchange Model ..... 137

A3 Quantification of Amide Proton Transfer Effect Pre- and Post-Gadolinium Contrast Agent Administration ..... 139

A3.1 Introduction ..... 139

A3.2 Materials and Methods ..... 140

A3.3 Results ..... 144

A3.4 Discussion ..... 148

A3.5 Conclusion ..... 151

A3.6 Supplementary Figures ..... 152

# Glossary

| | |
|---|---|
| **AF** | **A**verage **F**ield |
| **AP** | **A**verage **P**ower |
| **APT** | **A**mide **P**roton **T**ransfer |
| **APTR** | **APT R**atio |
| **AVIC** | **A**cute **V**ascular **I**maging **C**entre |
| **BET** | **B**rain **E**xtraction **T**ool |
| **BF** | **B**lood **F**low |
| **CEST** | **C**hemical **E**xchange **S**aturation **T**ransfer |
| **CNR** | **C**ontrast-to-**N**oise **R**atio |
| **CSF** | **C**erebro**S**pinal **F**luid |
| **CV** | **C**oefficient of **V**ariation |
| **CW** | **C**ontinuous **W**ave |
| **DC** | **D**uty **C**ycle |
| **DWI** | **D**iffusion-**W**eighted **I**mage/**I**maging |
| **EDS** | **E**venly **D**istributed **S**ampling schedule |
| **EPI** | **E**cho **P**lanar **I**maging |
| **FA** | **F**lip **A**ngle |
| **FAST** | **FMRIB**'s **A**utomated **S**egmentation **T**ool |
| **FDA** | **F**ood and **D**rug **A**dministration |
| **FLIRT** | **FMRIB**'s **L**inear **I**mage **R**egistration **T**ool |
| **FOV** | **F**ield **O**f **V**iew |

| | |
|---|---|
| **Gd** | **Gad**olinium contrast agents |
| **GM** | **G**rey **M**atter |
| **LDA** | **L**orentzian **D**ifference **A**nalysis |
| **MCAO** | **M**iddle **C**erebral **A**rtery **O**cclusion |
| **MR** | **M**agnetic **R**esonance |
| **MRI** | **MR I**maging |
| **MRS** | **MR S**pectroscopy |
| **MT** | **M**agnetization **T**ransfer |
| **MTR** | **MT R**atio |
| **$MTR_{asym}$** | **MTR asym**metry |
| **$MTR_{asym_comp}$** | **$MTR_{asym}$ comp**lementary |
| **NA** | **N**umber of **A**cquisitions |
| **NIHSS** | **N**ational **I**nstitute of **H**ealthy **S**troke **S**cale |
| **NMR** | **N**uclear **M**agnetic **R**esonance |
| **NOE** | **N**uclear **O**verhauser **E**ffect |
| **OSS** | **O**ptimal **S**ampling **S**chedule |
| **PARACEST** | **PARA**magnetic **CEST** |
| **PWI** | **P**erfusion-**W**eighted **I**mage/**I**maging |
| **RF** | **R**adio **F**requency |
| **RMS** | **R**oot **M**ean **S**quare |
| **ROI** | **R**egion **O**f **I**nterest |
| **rtPA** | **r**ecombinant **t**issue **P**lasminogen **A**ctivator |
| **SAR** | **S**pecific **A**bsorption **R**ate |

| | |
|---|---|
| **SNR** | **S**ignal to **N**oise **R**atio |
| **TE** | **E**cho **T**ime |
| **TR** | **R**epetition **T**ime |
| **WASSR** | **WA**ter **S**aturation **S**hift **R**eferencing |
| **WM** | **W**hite **M**atter |
| **WEX** | **W**ater **EX**change |

# List of Figures

**Figure 1.1**: Estimated cerebral blood flow thresholds for metabolic (left) and electrophysiological (right) disturbances. The brain image on the right is used to illustrate the infarct core and penumbra, where the former is the region in which blood flow is below the threshold of energy failure and the latter is the region of reduced blood supply but where the energy state is preserved. SEP = somatically evoked potentials; EEF = electroencephalogram. Modified from [6]. ..... 3

**Figure 2.1**: Longitudinal (left) and transverse (centre) relaxation of protons after RF irradiation, and the combined relaxation (right). $T_1$ refers to the time constant for the longitudinal magnetization to reach 63 % of its equilibrium magnetization and $T_2$ is the time constant for the transverse magnetization to decay to 37 % of its initial transverse magnitude. ..... 12

**Figure 2.2**: (left) Gadolinium enhanced $T_1$-weighted image and (right) $T_2$-weighted image of a patient with glioblastoma [25] (reproduced in part with permission from Springer). The relaxation properties are not only different between the healthy and pathological tissue, but also within the healthy tissues in the different compartment of the brain. ..... 12

**Figure 2.3**: Schematic representation of the CEST process. The top row (a – c) shows the distribution of spins/protons, aligned with and against the main magnetic field, $B_0$, and their respective simulated NMR spectra of two chemically distinct pools of nuclei during the CEST process are shown in the bottom row (d –f). The numbers in the figure represent the sequence of CEST. Pool *A* is the bulk water pool and pool *B* represents a labile pool that contains CEST agents involved in chemical exchange with the water pool when a $B_1$ is applied at the resonance frequency of pool *B*. ..... 14

**Figure 2.4**: Schematic sequence of different type of CEST RF irradiation schemes at a particular frequency offset. Crusher gradients are used to suppress residual transverse magnetization and to avoid unwanted echo formation. ..... 15

**Figure 2.5**: Simulated z-spectra of CEST imaging, where the blue and red-dotted lines are the saturated magnetization of 1- and 2-pool exchange system, respectively, and the green line is the initial magnetization. The z-spectrum can also be viewed as the inverted NMR spectra at different frequency offsets, where the water resonance is at 4.7 ppm in the spectroscopy scale. For the CEST spectrum, the water resonance is commonly rescaled with reference to 0 ppm. ..... 16

**Figure 2.6**: Different MRI modalities applied on an ischemic rat brain: a) $T_2$-weighted image; b) isotropic diffusion-weighted image; c) magnetization transfer ratio asymmetric analysis at 3.5 ppm; d) absolute pH-weighted image; e) histology of the rat brain after 8 hours of induced stroke, where the ischemic region is pointed by the blue arrows; f) schematic plot shows the classic definition of cerebral blood flow (pink), pH-weighted (yellow) and apparent diffusion coefficient (black) deficit mismatch. The right-most plot is the average z-spectra acquired during normocapnia (green) and cardiac arrest (red). Pictures (a-e) and the z-spectrum plot are taken from [22] (reproduced in part with permission from Nature Publishing Group)... 27

**Figure 2.7**: Various published APT results taken from some of the references in Table 2.2, where the red arrows indicate the ischemic area: a) APT image of a patient on day 5 post-onset, the black arrow points to an artefact [53]; b) APT images of a patient scanned 62 hours after the onset, two different slices of the brain are shown [94]; c) APT result of a patient on day 2 post-onset [95]; d) APT image of a patient with right middle cerebral artery infarction 48 hours after onset [96]; e) patient data from [97], where red area shows the FLAIR result at one month follow-up and green area is the acute time-to-peak lengthening; their corresponding z- and asymmetry spectra are shown using the respective colours in the plots next to it. Light blue area refers to the acute DWI hyper-intensity and the black plots refer to the signal from the healthy white matter which have higher APT signal than the red (ischemic tissue which progress to infarction at follow-up). Reproduced a) with permission from John Wiley and Sons, and b), c), d) and e) with permission from The International Society for Magnetic Resonance in Medicine (ISMRM). ..... 30

**Figure 2.8**: The influence of $B_0$ inhomogeneity. Top row shows the uncorrected $MTR_{asym}$ and z-spectrum. When there is a shift regarding the water centre frequency, $MTR_{asym}$ spectrum (red) cannot detect the presence of CEST agents in the phantoms. For the corrected z-

spectrum at the same voxel, the $MTR_{asym}$ spectrum clearly shows the presence of amine protons at 1.9 ppm. ..... 37

**Figure 2.9**: Unsaturated APT, $MTR_{asym}$ and $MTR_{asym_comp}$ images of a healthy subject scanned at 7T, where the asymmetry analyses have negative amplitude due to a broad saturation effect at the negative offsets; z-spectra of a region of interest in white matter of a healthy subject scanned at 3 and 7T, and their respective zoomed in z-spectra indicated by the red dashed rectangular boxes are plotted directly below them. The sampling interval of 3T z-spectrum is bigger (0.3 ppm) than the 7T counterpart (0.1 ppm). ..... 40

**Figure 3.1**: Simulated z-spectra using a 2-pool exchange model (water and amine protons). The parameter values used were set according to Sun et al. [99], unless otherwise stated: (a) varying the amine proton exchange rate while setting the amine to water proton concentration ratio to 1/247; and (b) changing the amine to water proton concentration ratio with amine proton exchange rate set to 30 $s^{-1}$. When either of the parameters varied, there was negligible change on the z-spectra at all the frequency offsets, except near the resonance frequency of amine pool (1.9 ppm). ..... 46

**Figure 3.2**: Normalized sensitivity function for (a) amine proton exchange rate, $k_{cest}$; (b) amine proton concentration, $M_{cest0}$; and (c) water center frequency shift, $\omega_w$, for a 2-pool exchange model. The parameters of interest were set as $k_{cest}$ = 50 $s^{-1}$, $M_{cest0}$ = 0.27 and $\omega_w$ = 0, other model parameter values were as given in the Materials and Methods section (sensitivity function was normalized to the highest magnitude of the function). ..... 57

**Figure 3.3**: OSS found from 1000 random samples (NA = 77). The z-spectrum (dots) was simulated using the parameter values applied to generate the results in Figure 3.2. The bar graph (vertical lines) represents the sampling points and the height of the bars refers to the number of samples for the OSS. The OSS sampling points from right to left are -0.6 to 0.7 and 1.3 to 2.4 ppm with intervals of 0.1 ppm. ..... 57

**Figure 3.4**: Normalized RMS errors (RMS errors/number of spectra) of the fitted model parameters within (top row) and beyond (bottom row) the optimized ranges for amine proton exchange rate, $k_{cest}$; amine proton concentration, $M_{cest0}$; and water centre frequency shift, $\omega_w$; for different SNR and NA studies. The percentage values above each bar are the differences

between the RMS errors of EDS and OSS, where a positive value means OSS was more accurate. ^ refers to the study with NA = 20 which was formed by proportionally reducing the OSS found from the search algorithm with NA = 77. ..... 58

**Figure 3.5**: Measured z-spectra of (a) different creatine concentration phantoms at pH 6.4 and (b) 125 mM creatine phantoms with different pH values. Water centre frequency shift was corrected using the WASSR map. ..... 59

**Figure 3.6**: WASSR maps (b and d) and model fitted water centre frequency shifts (c and e). Both the fitted results matched well to the WASSR maps. The arrangement of the phantoms is labelled in (a), where the top numbers represent the creatine concentration and the bottom ones refer to its pH value. ..... 60

**Figure 3.7**: Fitted amine proton exchange rate, $k_{cest}$ (a and c) and concentration, $M_{cest0}$ (b and d) using EDS and OSS for the tissue-like phantoms. ..... 61

**Figure 3.8**: Equilibrium magnetization image labelled with creatine concentration and pH of each sample. b) Conventional $MTR_{asym}$ obtained from the EDS data and CESTR* of (c) EDS and (d) OSS calculated from the fitted model parameters. The CESTR* variations for each phantom are shown in (e); the percentage value on top of each bar is the difference between the standard deviations in CESTR* of EDS and OSS. ..... 62

**Figure 3.9**: Simulated pulsed CEST normalized sensitivity function plots: (a) amine proton exchange rate, $k_{cest}$; (b) amine proton concentration, $M_{cest0}$; and (c) water center frequency shift, $\omega_w$, for a 2-pool exchange model. $k_{cest}$ and $M_{cest0}$ were most sensitive around the chemical shift of creatine (1.9 ppm) and $\omega_w$ was found to be very sensitive around ± 0.5 ppm. The plots were generated using the same parameter values used to produce Figure 3.2 (sensitivity function was normalized to the highest magnitude of the function). ..... 66

**Figure 4.1**: Simulated z-spectra using continuous approximation (AF and AP) and discretization method. The green circles highlight the major differences between the different methods. The right inlet plot shows a single Gaussian pulse with its equivalent AF and AP. 76

**Figure 4.2**: The minimal number of discretization, *N*, required to achieve normalized RMS error to be less than 0.1% when compared with the benchmark (1024 segments) for different

set of pulsed parameters. This four dimensional relationship (FA (*x*), $T_{pd}$ (*y*), DC (*z*) and *N* (color)) can be read by following the grid lines along each axis: there will always be 6 'balls' along the *z* direction which represent DC values from 30 to 80 %. ..... 77

**Figure 4.3**: (a) Measured z-spectra of different creatine concentration phantoms at pH 6.5. (b) Measured z-spectra of 125 mM creatine phantoms with different pH values. The asymmetry analysis spectra are plotted underneath the z-spectra in each plot. (c) $MTR_{asym}$ image at 1.9 ppm and (d) the means and standard deviations of $MTR_{asym}$(1.9 ppm)..... 78

**Figure 4.4**: (a) Measured data of phantom with 125 mM creatine concentration at pH 6 and continuous (AP) and discretized model fitted z-spectra. The residuals are plotted below the fitted spectra (dotted lines). (b) Normalized sum of square error plot of continuous (AP) and discretized model fitting for phantoms with different pH values and concentrations. ..... 79

**Figure 4.5**: Fitted values of water center frequency shift, $\omega_w$, using (a) discretized and (b) AP continuous model-based analysis, (c) is the $B_0$ map generated using WASSR. ..... 80

**Figure 4.6**: Fitted values of amine proton exchange rate, $k_{cest}$, using (a) discretized and (b) AP continuous model-based analyses. The mean and standard deviation of fitted $k_{cest}$ using different methods are shown in (c). The P values displayed above the bars are the results of the two-tail t-tests ($P < 0.05$)..... 80

**Figure 4.7**: The other sets of pulsed parameters which should produce equivalent quantitative fitting results (white circles) for the important model parameters investigated when AP approximation is used. Black circles represent the sets of pulsed parameters that had a sum of square and $MTR_{asym}$ difference bigger than the benchmark (the one used in the phantom study)..... 85

**Figure 5.1**: Measured z-spectra after $B_0$ correction and model fits in the different ROIs of patient 3 (top row) and 4 (bottom row), where the red area indicates the ischemic tissue (hyper-intensity on DWI data (b = 1000) acquired during admission) and the blue region refers to the contralateral normal appearing tissue. Very good fits were obtained in the ROIs with the coefficient of determinant, $R^2 \geqslant 98.6$ %. The vertical black dashed lines represent the

chemical shift of amide protons and the blue/red dashed lines underneath the fits and measured data are the residual..... 99

**Figure 5.2**: APT unsaturated images and calculated maps of APTR*, $MTR_{asym}$ and $MTR_{asym_comp}$ of healthy volunteers. Tissue masks generated from FAST have been used to mask out the non-tissue areas such as CSF; thus, the colour scale does not reflect the quantified APT effect in these areas. The bar graphs and error bars are the means and standard deviations, respectively, of each metric in the GM and WM. CV stands for coefficient of variation and C refers to the contrast between the GM and WM. ..... 100

**Figure 5.3**: Patient 3 data (APT, $T_1$, DWI (b = 1000) and PWI) and the processed APT results (APTR*, $MTR_{asym}$ and $MTR_{asym_comp}$) on admission, and follow-up FLAIR image on day 7. Tissue masks generated from FAST have been used to mask out the non-tissue areas such as CSF; thus, the scale bar does not reflect the quantified APT effect in these areas..... 101

**Figure 5.4**: Patient 4 data (APT, $T_1$ and DWI (b = 1000)) and the processed APT tissue results (APTR*, $MTR_{asym}$ and $MTR_{asym_comp}$) on admission, and follow-up FLAIR image on day 7. PWI was not acquired in the initial scan due to technical and time constraint. Tissue masks generated from FAST have been used to mask out the non-tissue areas such as CSF; thus, the scale bar does not reflect the quantified APT effect in these areas. ..... 102

**Figure 5.5**: Results of unpaired t-tests at a 5% significance level between the infarct core and contralateral normal appearing tissue region of APTR*, $MTR_{asym}$ and $MTR_{asym_comp}$, where the '++' symbols represent the non-significant differences found and the unlabelled results refer to significant differences and the 'group' label represents the average results of all the patients. The bar graphs and error bars refer to the means and standard deviations of each metric, respectively. Bounded results indicate only $MTR_{asym}$ smaller than 0 and $MTR_{asym_comp}$ within -1.5 and 0 were included, whereas unbounded refers to the results studied directly on all the calculated values. ..... 103

**Figure 5.6**: (Top-left) A logarithmic relationship between pH and amide proton exchange rate proposed by Zhou et al. [22]. (Top-right) The pH vs APTR* relationship formed by simulations; very good fits were obtained ($R^2$ = 99.94%) for the pH values from 6.4 to 7.5. The middle and bottom row shows the quantitative pH map of healthy subjects and patients presented in

Figure 5.3 and Figure 5.4, respectively, generated using the pH and APTR* relationship found. The pH scale was set based on the logarithmic relationship study [22], where pH values of 7.1 and above were normal (green), 7.1 to 6.9 were hypercapnia (light green) and below 6.9 was ischemic (pink to red). The blue lines in the patient images represent the area of infarction observed on day 7 follow-up FLAIR data. Tissue masks generated from FAST have been used to mask out the non-tissue areas such as CSF; thus, the colour scale does not reflect the quantified APT effect in these areas. ..... 105

**Figure 6.1**: pH maps generated based on the methods proposed in chapter 5. The growth of pH deficit area at a later time points may be an indication of poor clinical outcome, where a very large abnormality was observed in the follow up FLAIR data. The NIHSS at <6 hours was 24, at 24 hours was 25 and on day 7 follow-up was 28 (higher score indicates a more severe stroke and less likely to have a good outcome). . ..... 118

**Figure 6.2**: APTR*, NOE*, DWI (b = 1000) and follow up FLAIR images of patient 4 in chapter 5, where the previous three were acquired around hyper-acute period and the latter was collected 7 days after the ischemic onset. ..... 120

**Figure 6.3**: $MTR_{asym}$ and the measured z-spectra in the tumour (red) and contralateral tissue (blue) of a rat brain at 9.4 T using a moderate saturation power (~1.8 μT). The black dashed lines are the resonance frequence of amide protons and the right most plot is the zoomed in z-spectra. ..... 122

# List of Tables

**Table 2.1**: Overview of studies using endogenous CEST contrasts in humans. Most of the details are taken from [66]. Abbreviations: No. Pat. = number of patients; and No. Vol. = number of healthy volunteers. ..... 23

**Table 2.2**: Application of APT imaging in ischemic stroke patients..... 29

**Table 3.1**: Difference in CV ($CV_{EDS} – CV_{OSS}$) of the fitted amine proton exchange rate, $k_{cest}$, and concentration, $M_{cest0}$. A positive difference indicates the model fitted results from OSS were more precise than EDS. ..... 60

**Table 4.1**: Coefficient of determination, $R^2$ (mean ± standard deviation, %), for discretized model fitting. ..... 79

**Table 4.2**: Difference of coefficient of variation (CV) for the fitted amine proton exchange rate ($k_{cest}$) using discretized and continuous (AP) model-based analysis. * Positive values mean that discretized fitted results have smaller variation. ..... 80

**Table 5.1**: Summary of details and clinical symptoms of the patients recruited in this study, where TACS stands for total anterior circulation stroke. ..... 92

**Table 5.2**: Model parameters with prior values expressed as mean and standard deviation (SD) of a normal distribution, modified from [44]..... 95

**Table 5.3**: Contrast (C) between infarct core and contralateral normal appearing tissue, and coefficient of variation (CV) in the contralateral tissue of APTR*, $MTR_{asym}$ and $MTR_{asym_comp}$ of each patient. All the results are expressed in percent (%); only bounded $MTR_{asym}$ and $MTR_{asym_comp}$ are included. ..... 104

# List of Publications

**Journal articles**

*Evaluating the use of a continuous approximation for model-based quantification of pulsed chemical exchange saturation transfer (CEST)*
**Y.K. Tee**, A.A Khrapichev, N.R. Sibson, S.J. Payne, and M.A. Chappell
*Journal of Magnetic Resonance*, 222: 88-95, 2012.

*Optimal sampling schedule for chemical exchange saturation transfer*
**Y.K. Tee**, A.A Khrapichev, N.R. Sibson, S.J. Payne, and M.A. Chappell
*Magnetic Resonance in Medicine*, 70:1251-1262, 2013.

*Quantification of amide proton transfer effect pre- and post-gadolinium contrast agent administration*
**Y.K. Tee**, M.J. Donahue, G. Harston, S.J. Payne, and M.A. Chappell
*Journal of Magnetic Resonance Imaging*, in press.

*Comparing different analysis methods for quantifying the MRI amide proton transfer (APT) effect in hyperacute stroke patients*
**Y.K. Tee**, G.WJ. Harston, N.P. Blockley et al.
*NMR in Biomedicine*, in press

*Ventricular extension of intracerebral hemorrhage during intravenous thrombolysis*
G.WJ. Harston, **Y.K. Tee** et al.
*Cerebrovascular Diseases*, 36:324-325, 2013.

*Quantitative Bayesian model-based analysis of amide proton transfer MRI*
M.A. Chappell, M.J. Donahue, **Y.K. Tee** et al.
*Magnetic Resonance in Medicine*, 70:556–567, 2013.

**Conference abstracts**

*Assessing different amide proton transfer (APT) quantification methods in hyper-acute stroke patients*
**Y.K. Tee**, G.WJ. Harston, N.P. Blockley et al.
*22th ISMRM-ESMRMB*, May 2014, Milan, Italy

*Generating quantitative pH maps in hyper-acute stroke patients using amide proton transfer (APT) imaging*
**Y.K. Tee**, G.WJ. Harston, N.P. Blockley et al.
*22th ISMRM-ESMRMB*, May 2014, Milan, Italy

*Moving towards quantitative amide proton transfer (APT) imaging for stroke diagnosis*
**Y.K. Tee**, G.WJ. Harston, N.P. Blockley et al.
*CEST 2014 Workshop*, May 2014, Bioindustry Park, Colleretto Giacosa, Italy

*Does it affect the quantification if amide proton transfer imaging is performed pre- or post-gadolinium contrast agent administration?*
**Y.K. Tee**, M.J. Donahue, S.J. Payne, and M.A. Chappell
*21th ISMRM*, April 2013, Salt Lake City, USA

*Optimal sampling for model-based quantification of CEST*
**Y.K. Tee**, S.J. Payne, and M.A. Chappell
*OctoberCEST Workshop*, Oct 2012, Annapolis, USA

*Analyze the important fitted parameters using pulsed fitting and continuous CEST approximation for pulsed CEST*
**Y.K. Tee**, A.A Khrapichev, N.R. Sibson, S.J. Payne, and M.A. Chappell
*20th ISMRM*, May 2012, Melbourne, Australia

*Analyzing the minimum discretization of pulses required to speed up model-based analysis for pulsed CEST*
**Y.K. Tee**, A.A Khrapichev, M.J. Donahue, N.R. Sibson, S.J. Payne, and M.A. Chappell
*20th ISMRM*, May 2012, Melbourne, Australia

*CEST sensitivity functions based sampling schedule*
**Y.K. Tee**, M.A. Chappell, J. Xie and S.J. Payne
*19thISMRM*, May 2011, Montreal, Canada

*PH-weighted imaging in acute stroke using amide proton CEST*
G. Harston, **Y. K. Tee,** N. Blockley et al.
*22th ISMRM-ESMRMB*, May 2014, Milan, Italy

*Tissue outcome prediction in ischaemic stroke with diffusion, perfusion and pH sensitive CEST imaging at three different time points*
J. Levman, G. Harston, **Y. K. Tee** et al.
*22th ISMRM-ESMRMB*, May 2014, Milan, Italy

*Prospective motion correction with EPI volume navigators for chemical exchange saturation transfer (CEST) imaging*
R. Frost, A.T. Hess, N.P. Blockley, **Y.K. Tee** et al.
*22th ISMRM-ESMRMB*, May 2014, Milan, Italy

*pH-weighted imaging in acute stroke: how does it compare to conventional techniques?*
G.WJ. Harston, **Y.K. Tee** et al.
BRAIN, May 2013, Shanghai, China

*pH-weighted imaging in acute stroke: can metabolic imaging help us better understand the penumbra?*

G.WJ. Harston, **Y.K. Tee** et al.
European Stroke Conference, May 2013, London, UK

*Diffusion tensor imaging to identify structural change following lacunar stroke*
G.WJ. Harston, T. Okell, N. Blockley, M.A. Chappell, J. Levman, **Y.K. Tee** et al.
*European Stroke Conference,* May 2013, London, UK

*Tissue outcome in acute ischemic stroke: how useful is perfusion?*
G.W.J. Harston, T. Okell, M.A. Chappell, N. Blockley, **Y.K. Tee**, J. Levman, et al.
*European Stroke Conference*, May 2013, London, UK

*Glycogen chemical exchange effects in $^{1}$H-MRS and glyco-CEST at 3T and 7T*
R. Ouwerkerk, **Y.K. Tee**, C.K. Jones.
*21$^{th}$ ISMRM*, April 2013, Salt Lake City, USA

*Quantitative model-based analysis of amide proton transfer MRI*
M.A. Chappell, M.J. Donahue, **Y.K. Tee** et al.
*19$^{th}$ISMRM*, May 2011, Montreal, Canada

# Chapter 1

# Introduction

## 1.1 Stroke Statistics

Stroke is a pathology associated with rapid loss of brain function due to a sudden disruption of blood supply to the brain, resulting from ischemia or haemorrhage. An ischemic stroke is caused by a blocked blood vessel and a haemorrhagic stroke is triggered by internal bleeding, for example the rupture of a cerebral aneurysm. According to the Stroke Association, 85% of strokes are caused by ischemia and the remainder are due to haemorrhage [1].

Each year approximately 15 million people worldwide have a stroke and it is one of the leading causes of death worldwide, being the second leading cause of death in Europe after cancer [2] and fourth in the UK behind cancer, heart and respiratory disease [3]. In the UK, there are approximately 152, 000 strokes every year [3]: that is more than one every five minutes.

According to a recent stroke statistic published by the Stroke Association, one in five strokes is fatal [1]. In 2010, stroke caused almost 50, 000 deaths in the UK [3]. Stroke is also one of the leading causes of adult disability, causing many stroke survivors to be left dependent on others for their daily activities [4] and at least 450,000 people are severely disabled as a result of this in England [5]. The estimated direct and indirect economic cost of stroke to the UK is in the range of £ 3.7 - 7 billion every year [3, 5].

## 1.2 Pathophysiology of Stroke

In a healthy brain, the glucose and oxygen demand of tissues are provided by blood flow. When an acute ischemic stroke happens, the blood flow is impeded. An imbalance arises

as a result of low or no metabolic supply, leading to hypoxia and finally cerebral infarction which has been defined as brain cell death due to prolonged ischemia [6-8].

The metabolic and ionic disturbances in the periphery of focal ischemia (confined to a certain region of the brain) are illustrated in Figure 1.1 and have been proposed to evolve in the following order [6-8]:

1) initially protein synthesis is inhibited at a blood flow (BF) threshold of about 0.55 ml/g/min (~ 55%);
2) followed by stimulation of anaerobic glycolysis that causes the accumulation of lactate (BF below 0.35 ml/g/min or ~ 35%);
3) when the BF drops to about 0.2 ml/g/min (~ 20%), the energy state breaks down (the energy transformation processes stop);
4) finally, anoxic depolarisation of the cell membrane happens if the flow continues to decrease below 0.15 ml/g/min (~ 15%).

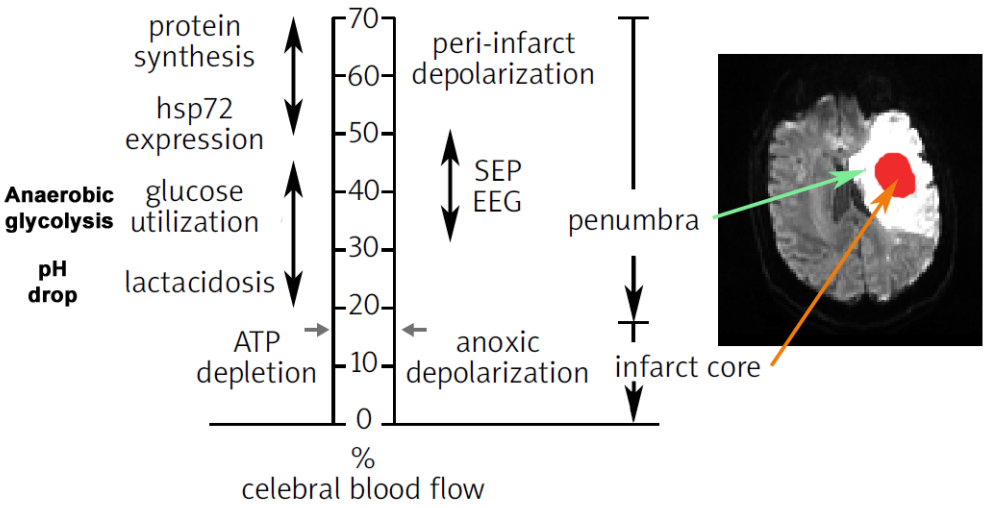


**Figure 1.1: Estimated cerebral blood flow thresholds for metabolic (left) and electrophysiological (right) disturbances. The brain image on the right is used to illustrate the infarct core and penumbra, where the former is the region in which blood flow is below the threshold of energy failure and the latter is the region of reduced blood supply but where the energy state is preserved. SEP = somatically evoked potentials; EEF = electroencephalogram. Modified from [6].**

After anoxic depolarisation of the cell membrane, the cell is infarcted. Cerebral infarction progresses to the surrounding cells if no intervention is taken and the progression can be differentiated into acute, sub-acute and delayed phase [7].

In the acute phase, ischemia-induced energy failure and the resulting terminal depolarisation of cell membranes are the direct consequence of tissue injury. This generally happens after a few minutes of ischemic stroke.

The sub-acute phase starts when anoxic depolarisation of the cell membrane occurs, resulting in the cell releasing a large amount of potassium and excitatory amino acids which trigger spreading depression-like depolarisation in the surrounding tissue through diffusion or astrocyte inter-connections [9]. This is one of the mechanisms in the sub-acute phase which causes the infarct core to expand into the peri-infarct penumbra (salvageable tissues if blood supply and energy state can be restored). Without timely reperfusion, the expansion will become congruent with the penumbra. The spreading depression and a multitude of cell biological disturbances are collectively referred to as molecular injury. In this phase, the largest increment of infarct volume can be observed.

The third phase is the delayed phase of injury which may last for days or weeks. During this phase, a number of secondary phenomena such as inflammation, oedema formation, reperfusion injury and apoptosis may aggravate the severity of the cerebral infarction.

## 1.3 Stroke Treatment and its Challenges

Recent progress in acute stroke treatment has shown that thrombolysis - the treatment of breaking up and dissolving the blood clots - increases the survival rate and reduces the disability of ischemic stroke patients. Currently, the recombinant tissue

plasminogen activator (rtPA) is the only Food and Drug Administration (FDA) approved thrombolytic treatment. The rtPA has a therapeutic window of 3 hours after the onset of ischemia [10]. Due to the restrictive therapeutic window of rtPA administration, only approximately 1 to 2 % of acute stroke patients are estimated to receive this therapy [11, 12].

Many clinical trials have been carried out to expand the time window of successful thrombolysis and some have shown a positive response even up to nine hours after the occurrence of stroke [13]. These findings together with more efficient clinical protocols in stroke management have increased the number of patients treated with rtPA. In 2010, about 5% of stroke patients received thrombolytic treatment in England, Wales and Northern Ireland, though it could have potentially benefited 14% of them [1].

Clearly, there are some obstacles preventing the wider clinical use of thrombolysis, which has been shown to greatly benefit ischemic stroke patients [11, 14-16]. The restricted therapeutic time window and the complications of thrombolytic therapy - intracranial haemorrhage - are some of the main reasons which limit the widespread use of the clot busting treatment. The incident rate of intracranial haemorrhage caused by the treatment ranges from 5 to 10% and the mortality rates as a result of the complication vary from 50 to 83% [10, 17, 18], about a 10-fold increase compared to the untreated (placebo) group in some studies [10]. More recently, the intracranial haemorrhagic side-effect was reported to be as high as 58% after intravenous rtPA administration [19].

## 1.4 pH Imaging for Stroke

During ischemic oxygen depletion, metabolism in the unperfused brain tissue area is initially sustained by anaerobic glycolysis, which is a process that transforms glucose into

energy when limited amounts of oxygen are available, and produces lactate as a by-product [20, 21].

However, anaerobic glycolysis is not efficient in producing energy and cannot supply cellular metabolism over a long period of time. Therefore, without timely reperfusion within the four to nine-hour window, cells will ultimately depolarize and die as previously described [6-8]. The accumulation of lactate during anaerobic glycolysis causes the intracellular pH to decrease. This decrease has been shown to be correlated to the exchange rate of protons attached to amide groups with water protons, and can be measured using magnetic resonance imaging (MRI) through a mechanism known as chemical exchange saturation transfer (CEST) [22].

Since there is a haemorrhagic risk associated with the use of rtPA, it is very important to better identify those acute ischemic stroke patients that are more likely to respond to thrombolytic treatment to outweigh the risk. CEST imaging, which can image pH qualitatively, quantitatively and non-invasively, can play a vital role in the stroke diagnosis because lactacidosis happens prior to cerebral infarction, based on the metabolic change shown in Figure 1.1; thus by assessing the metabolic state of the tissue, more specifically pH changes, it is hypothesized that pH imaging may potentially offer improved prediction of ischemic injury.

## 1.5 Thesis Outline

This thesis focuses on improving CEST imaging for clinical stroke diagnosis, seeking means for quantifying pH by using a quantitative and reproducible measure, optimizing CEST experimental protocols and finally applying it in hyper-acute ischemic stroke patients to study

which quantification method has the best potential to be used to improve clinical stroke imaging. The following chapters are structured as below:

**Chapter** 2 covers the basics of MRI and a literature review of CEST imaging, discusses the CEST mechanism, the types of CEST imaging and the role of CEST imaging as a potential marker of tissue pH. The chapter also introduces various quantification methods for the CEST signal and lists the limitations of each of them.

**Chapter** 3 discusses a novel CEST data acquisition scheme that enables confident selection of sampling points for the experiment. This is done to optimize the information available in the collected data for the parameters of interest such as amide proton exchange rate, which correlates to the tissue pH, to improve the CEST experimental protocols for clinical translation.

**Chapter** 4 details the differences between pulsed and continuous CEST imaging using tissue-like phantoms, assesses methods to quantify the CEST effect and studies ways to speed up the analysis, with the aim to quantify pH by moving from a qualitative to a more quantitative and reproducible measure.

**Chapter** 5 demonstrates the application of CEST imaging in hyper-acute stroke patients and compares the efficacy of some commonly used metrics to determine which quantification method is more suitable for improving acute stroke diagnosis to facilitate clinical translation.

**Chapter** 6 summarises the findings of this thesis and proposes areas for potential future work and improvement.

# Chapter 2

# Basics of MRI and Literature Review of CEST Imaging

This chapter is related to the basics of MRI and covers a literature review of CEST imaging, discusses the CEST mechanism, the types of CEST imaging and the role of CEST imaging as a potential marker of tissue pH. The chapter also introduces various quantification methods for the CEST effect and lists the limitations of each of them for clinical stroke imaging.

# 2.1 Basics of MRI

## 2.1.1 Spin and Precession

Atoms consist of 3 fundamental particles: protons (positive charge), neutrons (no charge) and electrons (negative charge). All these particles possess an intrinsic angular momentum referred to as spin which is a fundamental property of nature similar to electrical charge and mass.

A nucleus, where the protons and neutrons are, is continuously precessing about an axis that is perpendicular to the direction of rotation at a constant rate. A nucleus has no spin if it has an even number of protons (atomic number) and an even atomic weight (sum of the number of protons and neutrons). This kind of nucleus cannot be studied using magnetic resonance (MR) since it does not interact with an external magnetic field. Only nuclei with either an odd atomic number or an odd atomic weight have a net spin and are thus suitable for MR study. The protium ($^{1}H$) nucleus consists of a single proton, hence $^{1}H$ is often referred to as proton. The protium is an ideal choice for the study of MR because: 1) it is the most abundant isotope for hydrogen; 2) it has one of the largest responses to an applied external field; and 3) the human body is primarily composed of water and fat, both of which contain hydrogen [23].

A spin cannot be decreased or increased but the axis of the spin can be changed. A positively charged nucleus has a local magnetic field. When it is placed inside an external magnetic field, $B_0$, the spin axis of the proton will change, causing it to precess around the external field axis, where the proton is tilted slightly away from the axis of the applied magnetic field, but its axis of rotation is parallel to $B_0$. The angular frequency or more commonly known as the Larmor frequency, $\omega_0$, can be calculated using the equation: $\omega_0 = 2\pi f = \gamma B_0$, where $f$ is the frequency of precession and $\gamma$ is the gyromagnetic ratio, equal to 42.58 MHz/T for hydrogen [24].

### 2.1.2 Equilibrium Magnetization

In general, MR measurements are made on a collection of protons. In the absence of an external field, each proton has a spin vector of equal magnitude but random phase, leading to zero net magnetization. When an external magnetic field is introduced, the protons will align with the applied field, generating a net magnetization, $M_0$, that is proportional to the proton density. At equilibrium, the difference between the number of spins aligned with and against the magnetic field is only about 1 in $10^5$ protons for a 1.5 T external field [24]. As a result, higher magnetic field strength scanners are generally desirable because the difference between the number of spins aligned with and against the applied magnetic field will be bigger, generating a larger $M_0$, but there are some limitations for the higher field strength scanner which will be discussed in the later section.

### 2.1.3 Radio Frequency (RF) Pulses

The local value of $M_0$ is not measurable because $B_0$ is many orders of magnitude stronger than $M_0$. Thus, RF pulses ($B_1$) with the same Larmor frequency as protons are usually

applied to tip the net magnetic field away from $B_0$ so that a transient but measurable signal can be produced. Such RF pulses are usually described by the flip angle they produce.

### 2.1.4 Relaxation

Once the $B_1$ field is removed, the protons tend to re-align with the $B_0$ field. This process is called relaxation, where protons release the energy absorbed from the RF pulses. There are two types of relaxation: longitudinal and transverse.

Assuming $B_0$ is applied along the positive z-direction, the longitudinal relaxation time, $T_1$, refers to the time for the longitudinal magnetization ($M_z$) to return back to 63% of its initial magnetization ($M_0$) after being tipped away by the $B_1$ pulses. The equation governing the $T_1$ relaxation can be described as: $M_z = M_0\left(1 - e^{-\frac{t}{T_1}}\right)$.

The transverse relaxation time, $T_2$, is the time required for the transverse component ($M_{xy}$) to decay to 37% of its initial value ($M_{xy0}$) after the RF irradiation. The equation governing this process is $M_{xy} = M_{xy0} * e^{-t/T_2}$.

Both of these relaxations happen simultaneously. In general, $T_2$ is always smaller than or equal to $T_1$. The individual and combined longitudinal and transverse relaxations are shown in Figure 2.1.

Conventional MRI has focused on generating contrast based on $T_1$ and $T_2$ values because different tissues have different relaxation properties, as do healthy and pathological tissue. Normally, images generated using these properties are called weighted images. An example of $T_1$- and $T_2$-weighted images of a patient with glioblastoma are shown in Figure 2.2.

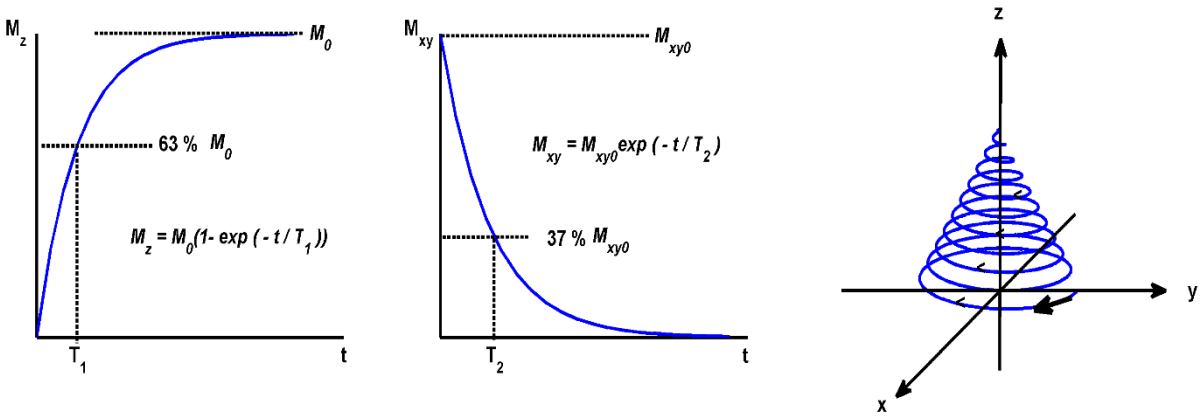


**Figure 2.1: Longitudinal (left) and transverse (centre) relaxation of protons after RF irradiation, and the combined relaxation (right). $T_1$ refers to the time constant for the longitudinal magnetization to reach 63 % of its equilibrium magnetization and $T_2$ is the time constant for the transverse magnetization to decay to 37 % of its initial transverse magnitude.**

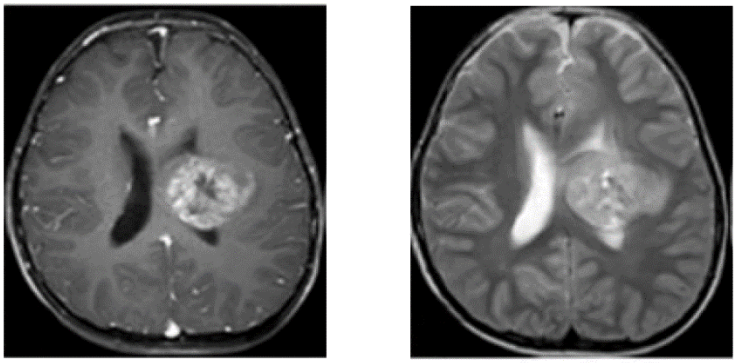

**Figure 2.2: (left) Gadolinium enhanced $T_1$-weighted image and (right) $T_2$-weighted image of a patient with glioblastoma [25] (reproduced in part with permission from Springer). The relaxation properties are not only different between the healthy and pathological tissue, but also within the healthy tissues in the different compartment of the brain.**

# 2.2 CEST Imaging

## 2.2.1 CEST Mechanism

CEST uses the chemical exchange of a nucleus from one site to a chemically different site to transfer saturation. Saturation refers to the Boltzmann distribution of nuclear spins aligned either with (low energy state) or against (high energy state) the main magnetic field, $B_0$, being temporarily altered when a RF pulse(s), $B_1$, is applied at the resonance frequency of a nucleus of interest. At equilibrium, the number of spins in the low energy state slightly

exceeds the number of spins in the high energy state; the distribution of spins between these two energy states is determined by the Boltzmann equation. When $B_1$ is applied, the spins will be promoted from the low energy state to the high energy state, leading to fewer spins align with the magnetic field and thus smaller net magnetization. When a pool is fully saturated by the applied $B_1$ pulses, it means that the numbers of spins in the low and high energy states become equal which result in zero net magnetization. CEST has been studied and used extensively in nuclear magnetic resonance (NMR) and recently, it has been regarded as a new way of generating contrast in MR images.

CEST causes a reduction in the signal intensity of a resonance such as water that is in chemical exchange with another resonance when a $B_1$ is applied at the resonance frequency of the latter protons. Figure 2.3 illustrates the CEST mechanism using a simple 2-pool exchange system labelled as *A* and *B*. The pools of exchanging protons have different resonance frequencies. The numbers in the figure correspond to the following events:

1. When the main magnetic field, $B_0$, is applied to the pools, the distribution of spins aligned with and against the magnetic field becomes unequal.
2. The irradiation of RF pulses at the resonance frequency of pool *B* saturates the NMR spectrum of the pool.
3. Chemical exchange leads to the transfer of protons from pool *B* to pool *A* and vice-versa.
4. This results in a transfer of saturation from pool *B* to pool *A* which contributes to the decrease of signal intensity in pool *A*.

Once the saturation pulse is removed, the distribution of spins will eventually revert back to the conditions as shown in Figure 2.3a). The magnitude of the CEST effect depends on solute concentration, temperature, pressure, magnetic field strength, RF saturation

power, pH value, exchange rate of the protons, and longitudinal and transverse relaxation time of the pools [26-29].

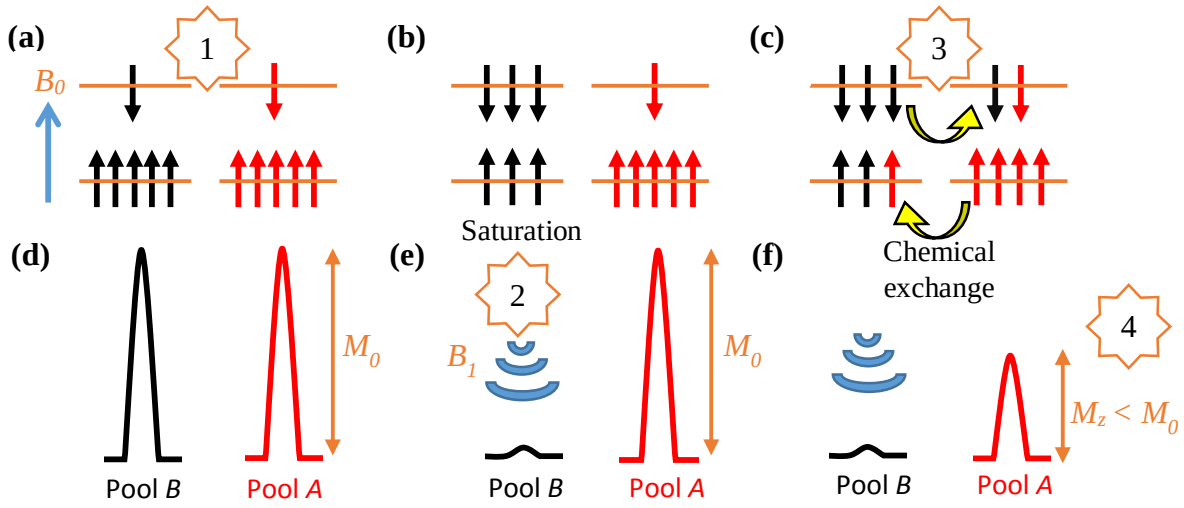


**Figure 2.3: Schematic representation of the CEST process. The top row (a – c) shows the distribution of spins/protons, aligned with and against the main magnetic field, $B_0$, and their respective simulated NMR spectra of two chemically distinct pools of nuclei during the CEST process are shown in the bottom row (d –f). The numbers in the figure represent the sequence of CEST. Pool *A* is the bulk water pool and pool *B* represents a labile pool that contains CEST agents involved in chemical exchange with the water pool when a $B_1$ is applied at the resonance frequency of pool *B*.**

## 2.2.2 Types of CEST Imaging

There are two types of CEST imaging – continuous and pulsed which are differentiated by the form of the RF irradiation pulses used. When a continuous (rectangular) pulse is applied to saturate the pools, it is referred as continuous-wave CEST (CW-CEST). Pulsed CEST uses multiple short but high intensity pulses to perform the saturation.

After a long rectangular pulse is applied to saturate the pools in the continuous case, a crusher gradient is applied to suppress the transverse magnetization before image acquisition (readout) to minimize image artefacts. When the crusher gradient is applied, the transverse magnetization dephases along the direction of the gradient, resulting in signal cancellation whereas the longitudinal magnetization is not affected by the gradient and thus

is preserved to give rise to a signal in subsequent image acquisition. Normally, a fast image acquisition method such as echo planar imaging (EPI) is used to minimize the relaxation. EPI is capable of producing a 2D image in a few tens of milliseconds. It employs a series of bipolar frequency-encoding gradients to form a train of gradient echoes. Each echo is spatially encoded so that multiple k-space lines, a matrix of digitized MRI data that represents an image after Fourier transform analysis, can be sampled within one or a few RF excitations.

For pulsed CEST, alternate sign crusher gradients are applied during the inter-pulse delays to nullify the transverse magnetization and to minimize unwanted echo formation. EPI is usually the preferred image acquisition technique but others such as fast imaging with steady state free precession acquisition [30] has been suggested recently. This is because the free precession acquisition can be implemented with centric phase encoding to maximize CEST sensitivity and has fewer image artefacts than EPI, however, the signal to noise ratio (SNR) is smaller than EPI. The CEST imaging sequence of the different types of saturations at a particular frequency offset is shown in Figure 2.4.

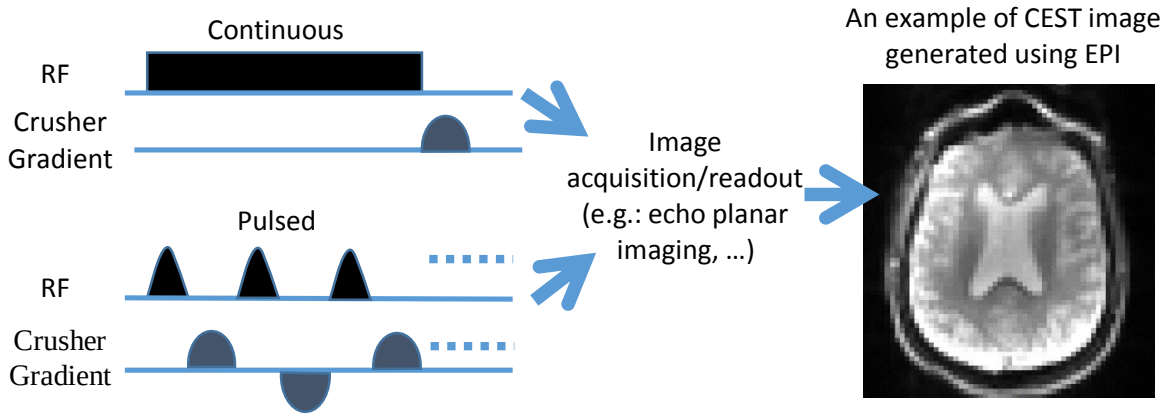


**Figure 2.4: Schematic sequence of different type of CEST RF irradiation schemes at a particular frequency offset. Crusher gradients are used to suppress residual transverse magnetization and to avoid unwanted echo formation.**

For a complete CEST acquisition, the sequence in Figure 2.4 is usually applied across a range of frequency offsets and the resultant plot is called the z-spectrum as shown in Figure 2.5. Basically, the z-spectrum is the measured signal of the bulk water pool in the z-direction at different frequency offsets.

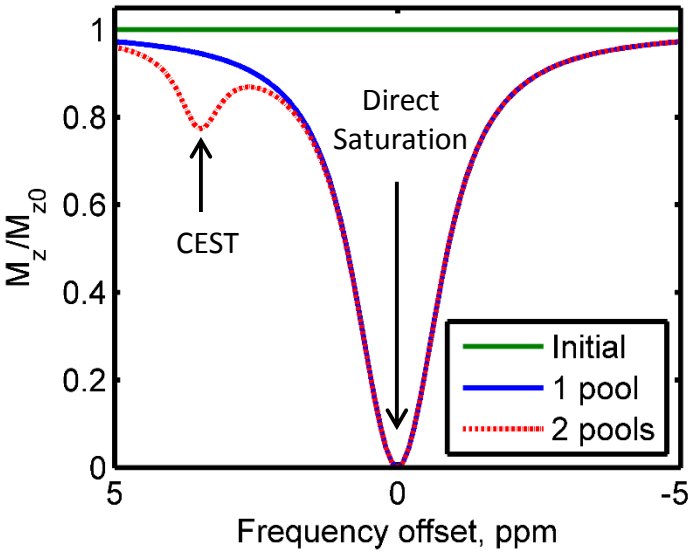


**Figure 2.5: Simulated z-spectra of CEST imaging, where the blue and red-dotted lines are the saturated magnetization of 1- and 2-pool exchange system, respectively, and the green line is the initial magnetization. The z-spectrum can also be viewed as the inverted NMR spectra at different frequency offsets, where the water resonance is at 4.7 ppm in the spectroscopy scale. For the CEST spectrum, the water resonance is commonly rescaled with reference to 0 ppm.**

Initially, the longitudinal magnetization is maximum (green line in Figure 2.5) because under the influence of $B_0$, the majority of the spins (protons) are pointing in the direction of the applied $B_0$. The z-spectrum is symmetric with respect to the water resonance after the saturation, if there is only one pool of protons in the system (blue spectrum in Figure 2.5). When the saturation is performed directly at the water resonance, it is referred to as direct saturation. If the saturation is performed not at the water resonance but the water signal is directly saturated, this phenomenon is known as the spillover effect.

When there is more than one pool of protons in the system and CEST occurs, the z-spectrum is no longer symmetric. The simulated red-dotted spectrum shown in Figure 2.5

represents the saturated magnetization of a 2-pool exchange system from -5 to 5 ppm; there are two dips – one at 0 (water pool) and the other at 3.5 ppm (assumed resonance of the labile pool); the dip at 0 ppm is due to direct saturation of water whereas the positive offset dip originates from the chemical exchange of the saturated and unsaturated nuclei as illustrated in step 4 of Figure 2.3.

The CW saturation scheme has several advantages over its pulsed counterpart. First of all, it is easier to optimize the CEST experiment because the saturation depends only on the amplitude and saturation time of $B_1$. Secondly, steady state saturation and maximal proton transfer enhancement can easily be achieved. In addition, a longer pulse leads to a smaller saturation bandwidth, leading to lesser cross-over saturation when the RF pulses are irradiated at the frequency offsets near to the water and labile proton resonance, thus resulting in narrower CEST dips on the z-spectrum acquired using the CW saturation.

However, a long continuous pulse is not permitted in MRI clinical applications due to the specific absorption rate (SAR) limit which is defined as the amount of RF power absorbed per unit of mass of an object (W/kg) by the International Electrotechnical Commission (IEC). SAR is associated with the heating of tissue: when a long saturation is applied *in vivo,* the accumulated power (heat) can kill the tissue. Besides that, most clinical scanners cannot generate a long enough CW pulse (several seconds) for the saturation due to hardware limitations. Therefore, only pulsed CEST, which uses high intensity but short duration pulses, can be applied in clinical settings currently.

Gaussian pulses are the most commonly used pulse shape for pulsed CEST because a study has shown that the optimized Gaussian RF irradiation can provide contrast similar to CW-CEST [31]. Since multiple pulses are used in pulsed CEST, $B_1$ is time dependent and the

CEST contrast is a function of irradiation pulse shape, flip angle of the irradiation pulses, irradiation pulse duration and duty cycle.

Several studies have optimized the pulses for pulsed CEST; it is generally found that an irradiation flip angle of 180° produces an optimal or near to optimal CEST effect, irrespective of the other acquisition parameters and sample properties, and that higher duty cycles lead to better contrast [32]. For clinical MRI scanners, 50 % duty cycles with 100 msec of irradiation pulses and inter-pulse delays are found to produce the best CEST effect with minimum interference from other confounding factors [33].

In order to generate an observable CEST effect or contrast, the exchangeable protons must be rapidly and selectively saturated, exchange quickly with water and remain on the water sufficiently long to build-up the saturation. Therefore, the exchange rate of the CEST agents should be as fast as possible while remaining slow on the NMR time scale because CEST studies are for slow to intermediate exchange conditions which means that the exchange rate has to be smaller than or equal to the chemical shift of the agents to the bulk water, $\Delta\omega$ ($\Delta\omega$ >> CEST agent exchange rate – slow regime; $\Delta\omega$ ~= CEST agent exchange – intermediate regime) [27, 28].

Recently, more sophisticated alternative sequences for CEST imaging have been proposed: these being saturation with frequency alternating RF irradiation [34], spin-locking [35], CEST phase mapping using a length and offset varied saturation scheme [36], two-frequency RF irradiation [37], chemical exchange rotation transfer [38], frequency labelled exchange transfer [39, 40] and variable delay multi-pulse CEST [41]. Since only the basic CEST sequence as shown in Figure 2.4 is relevant to the work presented in this thesis because the

equations or models governing the exchange process are quite different for some of them, please refer to the references provided for details about the mentioned sequences.

### 2.2.3 The General Modified Bloch Equations

As discussed in the previous section, CEST depends on the chemical exchange of nuclei between two or more different environments, often known as pools, one of which is the bulk water pool where the measurements are made. The *x*, *y* and *z* magnetizations are influenced by the chemical exchange of nuclei. Their MR behaviour can be described using the modified Bloch equations [42, 43]. For pool *i*, the magnetizations of the pool can be calculated using the following general equations [44]:

$$\frac{dM_x^i}{dt} = -(\omega_i - \omega)M_y^i - K_{2i}M_x^i + \sum_{j\in\boldsymbol{Q},j\neq i} k_{ji}M_x^j \,, \tag{1}$$

$$\frac{dM_y^i}{dt} = (\omega_i - \omega)M_x^i - K_{2i}M_y^i + \sum_{j\in\boldsymbol{Q},j\neq i} k_{ji}M_y^j - \omega_1 M_z^i \,, \tag{2}$$

$$\frac{dM_z^i}{dt} = \frac{M_0^i}{T_{1i}} - K_{1i}M_z^i + \sum_{j\in\boldsymbol{Q},j\neq i} k_{ji}M_z^j + \omega_1 M_y^i \,, \tag{3}$$

where:

$$K_{1i} = \frac{1}{T_{1i}} + \sum_{j\in\boldsymbol{Q},j\neq i} k_{ij} \,, \tag{4}$$

$$K_{2i} = \frac{1}{T_{2i}} + \sum_{j\in\boldsymbol{Q},j\neq i} k_{ij} \,, \tag{5}$$

$$k_{ij}M_0^i = k_{ji}M_0^j \,. \tag{6}$$

$\boldsymbol{Q}$ = {$a, b, c, \ldots$}, where $a, b, c, \ldots$ represent the pools in the system and $\boldsymbol{Q}$ has *NOP* elements, where *NOP* refers to number of pools in the system; *i* and *j* are elements of $\boldsymbol{Q}$; $k_{ij}$ is the proton exchange rate from pool *i* to pool *j*; $\omega$ is equal to $2\pi\boldsymbol{f}$, where $\boldsymbol{f}$ is a vector of saturation frequencies; $\omega_1$ is equal to $2\,\pi\,B_1$; and $T_{1i}$ and $T_{2i}$ are the longitudinal and transverse relaxation times, respectively, for pool *i*.

These coupled equations are linear and can be re-written into a more general matrix form and solved analytically [42, 43]:

$$\frac{d\boldsymbol{M}(t)}{dt} = \boldsymbol{A}\boldsymbol{M}(t) + \boldsymbol{B}\,, \tag{7}$$

where $\boldsymbol{A}$ is a square matrix that is defined as below:

$$\boldsymbol{A} = \begin{pmatrix} \boldsymbol{D}_a & \boldsymbol{O}_{ab} & \boldsymbol{O}_{ac} & \vdots \\ \boldsymbol{O}_{ba} & \boldsymbol{D}_b & \boldsymbol{O}_{bc} & \vdots \\ \boldsymbol{O}_{ca} & \boldsymbol{O}_{cb} & \boldsymbol{D}_c & \vdots \\ \cdots & \cdots & \cdots & \ddots \end{pmatrix}.$$

If there are 4 pools (*NOP* = 4), the size of $\boldsymbol{A}$ is 12 x 12 (3**NOP* x 3**NOP)*. $\boldsymbol{D}$ and $\boldsymbol{O}$ are the diagonal and non-diagonal elements of $\boldsymbol{A}$ respectively and are defined as below:

$$\boldsymbol{D}_i = -\begin{pmatrix} K_{2i} & (\omega - \omega_i) & 0 \\ -(\omega - \omega_i) & K_{2i} & \omega_1 \\ 0 & -\omega_1 & K_{1i} \end{pmatrix},$$

$$\boldsymbol{O}_{ij} = k_{ji}\begin{pmatrix} 1 & 0 & 0 \\ 0 & 1 & 0 \\ 0 & 0 & 1 \end{pmatrix} = k_{ji}\boldsymbol{I}_3\,.$$

$\boldsymbol{B}$ is a column matrix and its size is 1 x 3**NOP*. The matrix has the following form:

$$\boldsymbol{B} = (\boldsymbol{B}_a \quad \boldsymbol{B}_b \quad \cdots)^T\,,$$

where $T$ stands for transpose and $\boldsymbol{B}_i$ is equal to:

$$\boldsymbol{B}_i = \begin{pmatrix} 0 & 0 & \frac{M_0^i}{T_{1i}} \end{pmatrix}^T, \ i \in \boldsymbol{Q} \ .$$

The analytical solution of Eqn. (7) is [42, 43]:

$$\boldsymbol{M}(t) = e^{(\boldsymbol{A} * T_{sat})} * (\boldsymbol{M_0} + \boldsymbol{A^{-1}B}) - \boldsymbol{A^{-1}B} \ , \tag{8}$$

where $T_{sat}$ refers to saturation time and $\boldsymbol{M_0}$ is the initial magnetization of the pools which is defined as:

$$\boldsymbol{M}_0 = \ (\boldsymbol{M}_a \quad \boldsymbol{M}_b \quad \cdots)^T \ ,$$

where:

$$\boldsymbol{M}_i = \ (0 \quad 0 \quad M_0^i)^T, \ i \in \boldsymbol{Q} \ .$$

Recently, another approach to find the analytical solution of the modified Bloch equations has been proposed [45]. The $\boldsymbol{A}$ matrix is re-arranged into (2**NOP* + 1) x (2**NOP* + 1) elements, $\widetilde{\boldsymbol{A}}$, to remove the column matrix, $\boldsymbol{B}$. The analytical solution of Eqn. (7) can then be simplified to:

$$\widetilde{\boldsymbol{M}(t)} = e^{(\widetilde{\boldsymbol{A}} * T_{sat})} * \ \widetilde{\boldsymbol{M}_0} \ , \tag{9}$$

where $\widetilde{\boldsymbol{M}_0}$ = $[\boldsymbol{M}_0{}^T \ 1]^T$.

## 2.2.4 Potential Clinical Applications of CEST Imaging

The unique feature of CEST imaging is that it allows the detection of previously undetectable labile protons due to their low concentration through the chemical exchange reaction. This has led to the study of many potential clinical applications in recent years. The CEST agents can be broadly categorised into two groups: endogenous and exogenous.

Some examples of the endogenous agents, which have been used in the pre-clinical model, are the amide group in the endogenous mobile proteins and/or peptides for tumour [46-49] and stroke [22, 50-53] diagnosis, hydroxyl groups for type 2 diabetes [54] and myo-inositol for Alzheimer's disease [55, 56]. For the exogenous agents, applications such as mapping of kidney pH [57, 58], checking transplanted cell viability [59], monitoring brain neuronal activity [60], detecting enzyme activity [61], imaging brain deoxyglucose uptake and metabolism [62], monitoring glucose uptake in tumour metabolism [63] and acting as a potential reporter gene [64, 65] have been proposed.

However, due to various limitations such as SAR guidelines and scanner hardware constraints, most of the proposed applications have yet to be translated into routine clinical diagnostic tools. Table 2.1 summarizes the endogenous CEST agents that have been studied in humans and the origin of the molecules acting as the agents. The backbone amide group in the endogenous mobile proteins and/or peptides is best described in the literature [66]. This group has a chemical shift or resonance frequency at 3.5 ppm with respect to the water resonance [22] and the CEST experiment that uses this molecule to generate contrast is often referred to as amide proton transfer (APT) imaging. A number of other molecules have also been studied in humans; please refer to Table 2.1 for details.

As of today, there is still no published literature regarding the use of exogenous CEST agents in humans. Iopamidol, which has been used for kidney pH mapping in the animal models, has the most promising potential to be the first exogenous agent for human CEST applications because it is a FDA approved X-ray contrast agents routinely used for a variety of diagnostic applications with a very good clinical acceptance [57].

**Table 2.1: Overview of studies using endogenous CEST contrasts in humans. Most of the details are taken from [66]. Abbreviations: No. Pat. = number of patients; and No. Vol. = number of healthy volunteers.**

| Name | Molecule | Chemical shift | Origin | Area of applications | No. Pat. | No. Vol. | Reference |
|---|---|---|---|---|---|---|---|
| Amide proton transfer (APT) | Amides | + 3.5 ppm | Backbone structure of proteins | Brain | | 36 | [25, 34, 53, 67-70] |
| | | | | Brain tumour | 47 | | [25, 46, 49, 53, 67] |
| | | | | Prostate tumour | 13 | | [71] |
| | | | | Breast | | 10 | [72] |
| | | | | Breast tumour | 3 | | [72] |
| | | | | Radiation necrosis after arteriovenous malformation treatment | 1 | | [73] |
| | | | | Multiple sclerosis | 4 | | [68] |
| | | | | Stroke | 4 | | [53] |
| glycoCEST | Glycogen (glyco) | + 0.5 to 1.5 ppm | Primary form of glucose storage in muscle and liver | Calf muscle | | 4 | [74] |
| | | | | Lower back muscle | | 12 | [75] |
| gagCEST | Glycosamino glycans (gag) | + 0.9 to 1.9 ppm | Polysaccharide in cartilage | Knee cartilage | | 8 | [76, 77] |
| | | | | Knee cartilage after autologous osteochondral transplantation | 9 | | [78] |
| | | | | Knee cartilage after cartilage repair | 12 | | [79] |
| | | | | Intervertebral disc lumbar spine | 16 | | [80] |
| GluCEST | Glutamate (Glu) | + 3 ppm | Excitatory neurotransmitter | Brain | | 7 | [81, 82] |
| | | | | Spinal cord | | 7 | [83] |
| MICEST | Myo-inositol (MI) | + 0.2 to 1.56 ppm | Sugar-like brain metabolite in glial cells | Brain | | 5 | [55] |
| ureaCEST | Urea | + 1 ppm | Nitrogen-containing substance in urine | Kidney | | 5 | [84] |

## 2.2.5 CEST Imaging and pH

The first demonstration of CEST imaging to map the distribution of pH in a variety of phantoms was reported by Ward et al. [27] in 2000 and their follow-up study [26] showed that the chemical exchange rate of labile protons increases with increasing pH; thus the CEST effect is pH dependent, highlighting the potential of CEST imaging as a new approach for MRI based pH measurements. In theory, the proton exchange rate in an aqueous solution can be calculated as below [28]:

$$k_{sw} = k_a[H^+] + k_b[OH^-] + k_0 = k_a 10^{-pH} + k_b 10^{pH-pk_w} + k_0, \quad (10)$$

where $k_a$ is the acid catalysed exchange rate, $k_b$ is the base catalysed exchange rate, $pk_w$ is the negative logarithm of the dissociation constant of water and $k_0$ refers to other possible contributions.

Although other MR techniques such as phosphorous MR spectroscopy ($^{31}$P-MRS) exist for pH measurements, CEST imaging has higher spatial and temporal resolution. Additionally, CEST imaging does not require specialized hardware such as phosphorous coils to perform the measurements, making it a very promising technique to monitor the metabolic activities of tissue by tracking the pH change in pathological conditions such as ischemic stroke.

## 2.2.6 APT Imaging as a Marker of Tissue pH

In healthy tissue, intra- and extracellular pH are very well regulated by the body buffering system and cellular ion transporters. Small dynamic changes in tissue pH happen during normal physiological activities, for example neuronal activity, but the body's auto-regulation system is able to reverse the change very quickly and maintain pH at its equilibrium

level [85]. However, the acid-base homeostasis can be significantly altered in pathological conditions such as stroke, as described earlier, leading to a severe decrease in pH [52].

In 2003, Zhou and co-workers [22] were the first to demonstrate that the CEST signal from amide protons in the backbone of endogenous proteins and/or peptides could be used as a marker of tissue pH. Nowadays, the CEST signal at 3.5 ppm is more commonly known as the APT signal because it originates from the amide protons. The concentration of amide protons in endogenous mobile proteins and/or peptides is only in the milli-molar range; hence, it is impossible to image the protons directly. Although the concentration is extremely small *in vivo*, it is possible to achieve a detection sensitivity of several percent on the water signal (*in vivo* water concentration = ~ 112 M) using the CEST mechanism [22, 46].

Zhou and co-workers [22] discovered that the APT ratio (APTR, used commonly to quantify the APT effect) was 2.94 % in the normal rat brain and that the effect dropped to 1.04 % post-mortem, showing a 1.9 % decrease from before to after cardiac arrest. The corresponding pH values were 7.11 ± 0.13 and 6.66 ± 0.10, determined using $^{31}$P-MRS and the amide proton exchange rates, $k_{sw}$, measured using water exchange (WEX) spectroscopy were 28.6 ± 7.4 Hz at normocapnia and 10.1 ± 2.6 Hz post-mortem. According to a previous study on amide protons in aqueous solution [86], the amide proton exchange was found to be predominantly base-catalysed in the physiological pH range (6.5 to 7.5), thus Eqn (10) can be simplified to:

$$k_{sw} = k_b 10^{pH-pk_w} = 5.57 * 10^{pH-6.4}, \quad (11)$$

where $pk_w$ = 15.4 at 37 °C [87] and $k_b$ = 5.57 x $10^9$ Hz, obtained by fitting the *in vivo* and post-mortem exchange rates versus measured pH values [22].

Assuming that there is negligible back-exchange from saturated water, that the amide protons are fully saturated by a long saturation pulse and that the water longitudinal relaxation rate is much bigger than the exchange rate, APTR can be calculated as below [22]:

$$APTR = \frac{k_{sw}[amide]}{2[H_2O]R_{1w}}(1 - e^{-R_{1w}T_{sat}}) , \quad (12)$$

where $R_{1w}$ is the water relaxation rate ($1/T_{1w}$ = 0.714 Hz at 4.7 T), $T_{sat}$ is the saturation time (4 s, dependent on the experiment) and $[amide/H_2O]$ refers to the concentration of amide or water protons. Based on the measurements of APTR and $k_{sw}$ listed above, the *in vivo* amide proton concentration was estimated to be 71.9 mM [22]. If several other assumptions, such as negligible changes in the water longitudinal relaxation rate and the water and amide proton content of tissue following ischemic stroke, are made, APTR is then a simple function of pH [22]:

$$APTR = 5.73 * 10^{pH-6.4} . \quad (13)$$

This concept was first demonstrated by Zhou and co-workers [22] in a permanent ischemic rat model following middle cerebral artery occlusion (MCAO). They showed that the infarct could be detected by APT imaging and it was in good agreement with the diffusion-weighted images (DWI), and histology that was acquired after 8 hours of the induced stroke (Figure 2.6). Additionally, these pH-weighted changes were observed before the $T_2$-weighted image showed any detectable differences, suggesting that APT imaging had the potential to monitor acute pH change with possible applications to clinical stroke imaging.

Follow-up APT studies in MCAO animal models have also presented the same observations, where the APT effect decreases in the ischemic lesion [50, 52, 88-93]. The drop in the APT effect has been found to correlate with the lactate content [52] and pH [91, 93].

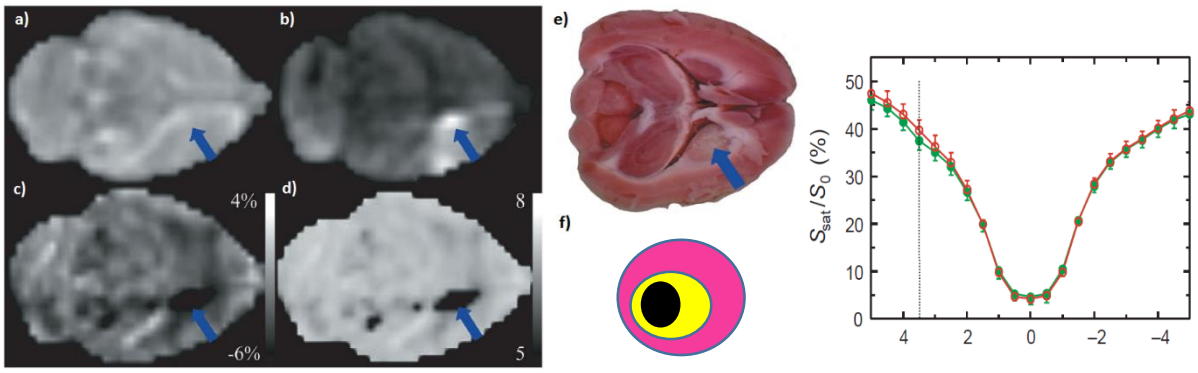


**Figure 2.6: Different MRI modalities applied on an ischemic rat brain: a) $T_2$-weighted image; b) isotropic diffusion-weighted image; c) magnetization transfer ratio asymmetric analysis at 3.5 ppm; d) absolute pH-weighted image; e) histology of the rat brain after 8 hours of induced stroke, where the ischemic region is pointed by the blue arrows; f) schematic plot shows the classic definition of cerebral blood flow (pink), pH-weighted (yellow) and apparent diffusion coefficient (black) deficit mismatch. The right-most plot is the average z-spectra acquired during normocapnia (green) and cardiac arrest (red). Pictures (a-e) and the z-spectrum plot are taken from [22] (reproduced in part with permission from Nature Publishing Group).**

Later studies showed that the pH-weighted deficit region was different from the mismatch lesion detected by perfusion weighted imaging (PWI) and DWI, where the pH deficit area was always bigger or equal to the diffusion deficit area but smaller than the perfusion abnormality [50, 88, 89], as shown in the schematic plot in Figure 2.6f). When this lower pH region, determined during the acute phase, was compared with the final infarct area defined based on $T_2$-weighted imaging at 24 hours post MCAO, a very high correlation between them was found [50]. Thus, this led to the suggestion that APT imaging could be used to separate regions within the PWI-DWI mismatch into ischemic penumbra, an area with hypo-perfusion and lower pH (salvageable tissue if re-perfused), and benign oligemia, hypo-perfusion but normal pH (tissue may not progress to infarction even if no re-perfusion) [50, 88]. This was supported by another study with shorter MCAO and re-perfusion after 65 minutes of occlusion, where the APT effect remained at decreased levels in tissue that ultimately progressed to infarction while the perfusion and diffusion signals recovered [92].

Due to these encouraging results obtained in the pre-clinical model, APT imaging has been suggested to provide complementary information to conventional MRI modalities, and

has been hypothesized to correspond better to the ischemic penumbra than the mismatch of PWI and DWI. Although APT imaging may not be the only definite diagnostic tool for clinical stroke imaging, it is potentially one of the important quantitative multi-parametric MRI modalities that can facilitate stroke management in the future [51, 52, 92].

### 2.2.7 APT Imaging for Clinical Stroke

In 2011, the first application of APT imaging in stroke patients was reported [53]. This study proposed the power and duration of $B_1$ required to produce the hypo-intensity APT effect for stroke, iso-intensity for the normal appearing tissue and hyper-intensity for tumour. Even though the patients were scanned in the delay phase (mean onset time of 4.3 days), the APT effect still showed a lower signal in the infarct area when compared to the contralateral normal appearing tissue. This remains the first and only published journal paper in this topic to date.

Table 2.2 summarizes the latest published literature (journal and conference) related to the use of APT imaging in the ischemic stroke patients. So far, APT imaging has been performed in at least 27 stroke patients but only about 11 of them were imaged within the hyper-acute period which is the therapeutic window of thrombolytic intervention (< 6 hours of onset) [14-16].

Figure 2.7 shows some of the published results from the references in Table 2.2. In general, the consensus appears to be that the APT effect becomes smaller in the infarcted tissue and penumbra during the hyper-acute period, owing to the pH reduction caused by the accumulation of lactate [52]. As mentioned previously, this observation is valid during the hyper-acute period because water relaxation time and amide proton concentration show negligible change in this time frame [22]. However, most of the reported cases so far do not

fall within this time window which can potentially explain the variability in the APT effect regionally because APTR depends on multiple parameters, not just on pH via the exchange rate as shown in Eqn. (12). Oedema formation will lead to a change in the water relaxation time and concentration, undermining the quantified effect. There may also be a change in the amide proton concentration due to cell depolarisation and loss of cytoplasm. Furthermore, some of the patients underwent either intra-venous thrombolysis or mechanical thrombectomy before or after APT imaging, which will alter the physiological condition of the brain, as well as the APT effect.

**Table 2.2: Application of APT imaging in ischemic stroke patients.**

| No. of Patients | Image Time After Ischemic Onset | Mean Onset Time | Hyperacute (< 4 or 6 hours) | Treatment ^ | Reference |
|---|---|---|---|---|---|
| 4 | 1–7 days | 4.3 ± 2.5 days | No | NI | [53] |
| 1 | 62 hours | 62 hours | No | NI | [94] |
| 2 | 11-14 hours | 18.5 – 20 hours | No | No | [95] |
| | 26-36 hours | | No | No | |
| 3 | 3 hours | 25 – 46 hours | Yes | NI | [96] |
| | 10 hours | | No | NI | |
| | 19 hours | | No | NI | |
| 3 | 24 - 48 hours | | No | NI | |
| 2 | 48 – 96 hours | | No | NI | |
| 7 | < 4 hours | < 4 hours | Yes | Yes(4), No (3) | [97] |
| 1 | 1 - 7 hours | | Yes* | No | |
| 2 | Unclear | | - | No | |
| 2 | < 6 hours | < 6 hours | Yes | Yes(1), No(1) | [98] |
| **11** out of the 27 patients were in the hyperacute period. | | | | | |

* Included in the hyper-acute stage even though it may be slightly out of the time frame.
^ The number in parenthesis followed immediately after 'Yes' or 'No' refers to the number of patients in that category and NI stands for 'No Information'.

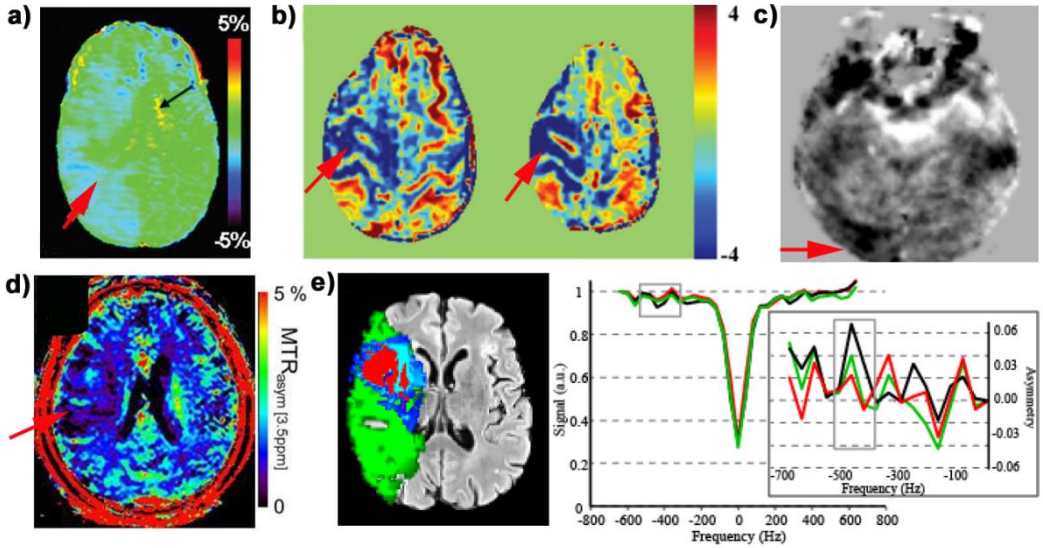


**Figure 2.7: Various published APT results taken from some of the references in Table 2.2, where the red arrows indicate the ischemic area: a) APT image of a patient on day 5 post-onset, the black arrow points to an artefact [53]; b) APT images of a patient scanned 62 hours after the onset, two different slices of the brain are shown [94]; c) APT result of a patient on day 2 post-onset [95]; d) APT image of a patient with right middle cerebral artery infarction 48 hours after onset [96]; e) patient data from [97], where red area shows the FLAIR result at one month follow-up and green area is the acute time-to-peak lengthening; their corresponding z- and asymmetry spectra are shown using the respective colours in the plots next to it. Light blue area refers to the acute DWI hyper-intensity and the black plots refer to the signal from the healthy white matter which have higher APT signal than the red (ischemic tissue which progress to infarction at follow-up). Reproduced a) with permission from John Wiley and Sons, and b), c), d) and e) with permission from The International Society for Magnetic Resonance in Medicine (ISMRM).**

Judging from the reported cases so far, the full potential of APT imaging for clinical stroke has not yet been fully explored. Although the preliminary results seem promising, better quantification methods are required to account for the variations in the different mentioned factors that can influence the APT effect. Until then, it is not easy to clinically endorse the potential of APT imaging as an important marker to predict ischemic injury.

## 2.2.8 APT Quantification Methods

### *2.2.8.1 Asymmetry Analysis*

The most commonly used method to quantify the APT effect is magnetization transfer ratio asymmetry analysis, $MTR_{asym}$, defined as:

$$MTR_{asym} = \frac{M(-\Delta\omega) - M(\Delta\omega)}{M_0}, \tag{14}$$

where $M(\Delta\omega)$ refers to the measured signal at 3.5 ppm (labelled scan), $M(-\Delta\omega)$ refers to the measured signal at -3.5 ppm (reference scan) and $M_0$ is the unsaturated signal, all in the z-direction (the subscript z is usually dropped because it is the convection that $M$ refers to the direction in which the measurements are made). This analysis depends on experimental parameters such as RF power [99] and saturation time [100]. It inherently assumes that all the non-CEST contributions are symmetric around the water resonance; thus, a pure APT effect can be obtained by taking the difference between the signals measured at positive and negative offset.

Various other forms of asymmetry measures, based on the concept of Eqn.(14), have been studied using phantoms, paramagnetic CEST agents and animal models, and it is found that a complementary type denoted as $ST^{com}$, where ST stands for saturation transfer, is more suitable for *in vivo* application [101]. For consistency in this work, $ST^{com}$ is renamed as $MTR_{asym_comp}$, and it can be calculated as below:

$$MTR_{asym_comp} = \frac{M(-\Delta\omega) - M(\Delta\omega)}{M_0 - M(-\Delta\omega)}. \tag{15}$$

*2.2.8.2 Three Offset Measurement*

The asymmetry analyses use the signal measured at positive and negative offset(s) to quantify the APT effect. For a well-delineated APT dip, the APT effect can be quantified using a simple three offset measurement based on the signal acquired at only one side of the z-spectrum [102]:

$$APT^{*} = \frac{\frac{M(\delta - \Delta) + M(\delta + \Delta)}{2} - M(\delta)}{M_0}, \quad (16)$$

where $\delta$ is the labelled image at a frequency offset which corresponds to the maximum APT effect and $\delta \pm \Delta$ refer to the two boundary images with minimum APT effect at an offset separation of $\pm\Delta$ from $\delta$. It is relatively easy to estimate the frequency offset of the maximum APT effect when there is a clear dip; the challenging part is to find the two boundary frequency offsets which can be approximated by a linear function.

APT* can be a good approximation of the pure APT effect when the dip is narrow and far away from the water resonance. When these assumptions are met, APT* can be obtained from a label image acquired at 3.6 ppm and the two boundary images at 3 and 4.2 ppm [102]:

$$APT^{*} = \frac{\frac{M(3\ ppm) + M(4.2\ ppm)}{2} - M(3.6\ ppm)}{M_0}, \quad (17)$$

*2.2.8.3 Lorentzian Difference Analysis (LDA)*

Under low power saturation and steady state conditions, the direct water saturation contribution (water pool) can be approximated using a Lorentzian line shape [103]:

$$L = 100 - A\left(\frac{\left(LW_{\frac{1}{2}}\right)^2}{\left(LW_{\frac{1}{2}}\right)^2 + 4\left(f_0 - f_{shift}\right)^2}\right) + b, \quad (18)$$

where $A$ is the amplitude, $LW_{\frac{1}{2}}$ is the water linewidth, $f_0$ is the water centre frequency shift of z-spectrum, and $b$ is the baseline offset. The Lorentzian fit is usually performed on the measured signal at frequency offsets around water resonance ($\left|f_{shift}\right| < 1ppm$) and at

frequency offsets above 6 ppm away from water resonance ($f_{shift} \geq 6\ ppm$), where limited non-CEST contributions are expected.

This is another type of quantification method that uses only one side of the z-spectrum to measure the APT effect, denoted as Lorentzian difference analysis (LDA). This method first subtracts the Lorentzian fitted curve using Eqn. (18) from the measured z-spectrum and then finds the mean of the resultant signal from 3.3 to 3.7 ppm to quantify the APT effect [104].

#### *2.2.8.4 Model-Based Analysis*

The MR behaviour of the protons in an APT experiment can be fully described by using the model introduced in section 2.2.3. A model-based analysis refers to fitting the modified Bloch equations using an optimization algorithm such as nonlinear least-squares or variational Bayesian method, to the measured z-spectrum. From a previous study [44], at least three pools of protons are required to perform the model fitting for the *in vivo* APT imaging: 1) water; 2) amide; and 3) asymmetry magnetization transfer (MT) pool.

Through the fitted parameters from the model-based analysis, a further quantitative metric can be calculated, denoted as APTR*. This measure uses the parameters obtained from model-fitting to generate an ideal 2-pool (water + amide) model and to compare it to an ideal 1-pool model of water, where both the ideal 1- and 2-pool model are simulated using the fitted parameters within the multi-pool fit, to obtain the pure APT effect [44]:

$$APTR^{*} = \frac{M_{1-pool}(\Delta\omega) - M_{2-pool}(\Delta\omega)}{M_0}\ , \tag{19}$$

where $M(\Delta\omega)$ is the simulated magnetization at 3.5 ppm using the fitted parameters and the subscript $1, 2-pool$ refers to the fitted parameters from the water or water+amide pool. Although a greater number of pools can be used to perform the model fitting as required,

only the fitted model parameters of water and APT pool obtained from the model-based analysis are used to calculate the APTR*, in order to prevent the other CEST or non-CEST contributions from contaminating the APT signal.

# 2.3 Limitations of APT Quantification Methods

There are various causes that contribute to the limitations of the different APT quantification methods introduced in the previous section. These causes can be broadly classified into two types. The first one is generic for any CEST experiment, including APT imaging, such as magnetic field strength and inhomogeneity, and inherent asymmetry in the *in vivo* z-spectrum. The second type primarily arises due to pathological conditions in stroke which lead to a change in the physiology and the parameters that affect the APT effect.

## 2.3.1 Magnetic Field Strength

When $B_0$ increases, the chemical shift increases ($\Delta\omega$ is proportional to $B_0$), leading to a bigger separation between the amide and water protons in term of Hertz (Hz) and thus a smaller spillover effect. The relaxation time of water is also proportional to the magnetic field strength: the stronger the magnetic field strength, the larger the relaxation time of water, prolonging the saturation and hence enhancing the APT effect.

Quantifying the APT effect using the three offset measurement is essentially an extreme simplification of the model-based approach by approximating the APT effect using a linear function. This method is generally more suitable for APT experiments performed using a high magnetic field strength scanner (≥ 7T) because it requires the APT dip to be narrow and well-delineated.

However, most of the clinical scanners nowadays are 3T and below; although 7T scanners are increasingly popular and used for research, it has yet to be approved as a routine clinical diagnostic tool. Performing the APT experiment at a lower field strength scanner results in a smaller and less well-defined APT dip due to higher spillover effect (smaller $\Delta\omega$) and shorter relaxation times.

Consequently, using the three offset measurement approach to quantify the APT effect will lower the sensitivity to the small signal change caused by a pH drop during the ischemic condition and is thus not suitable for clinical stroke imaging. The other quantification methods are less sensitive than the three offset measurement to the magnetic field strength and have been used in various *in vivo* APT imaging at 3T, although a higher field strength is generally desirable for APT imaging because it can generate a larger APT signal.

### 2.3.2 $B_0$ and $B_1$ Field Inhomogeneity

When the RF irradiation power strength is not negligible compared to the chemical shift between water and amide protons, there will be a direct RF saturation of the water signal (spillover effect). Due to this, the widely used asymmetry analysis is often performed to compensate for the spillover effect by applying the RF irradiation pulses at a labelled and a reference scan, which are at the opposite frequency offset to each other relative to the water resonance (Eqn. (14)). Hence, under ideal conditions, the RF spillover effect, which is approximately symmetric, can be suppressed by subtracting the labelled image from the reference counterpart.

The *in vivo* APT effect is highly affected by experimental conditions, especially field inhomogeneity, and this issue persists despite recent advancements in MRI technology. In the

presence of a $B_0$ field inhomogeneity, the water centre frequency will shift away from the expected value (0 ppm). This shift means that any applied RF saturation is not necessarily happening at the specific offset relative to water resonance: the labelled and reference scan are no longer symmetric around 0 ppm. Consequently, asymmetry analysis cannot fully remove the spillover effect and it will introduce a $B_0$ inhomogeneity-dependent MT ratio offset [105]. The same issue also affects the three offset measurement, resulting in the quantification of the APT effect being performed at frequency offsets that are different from the intended ones as presented in Eqn.(17).

If such a shift due to the field inhomogeneity is not corrected, it can cause significant quantification errors. Figure 2.8 shows an example of this issue using creatine phantoms which have a resonance frequency at 1.9 ppm [106]. When the shift due to field inhomogeneity is not corrected, the asymmetry analysis cannot correctly quantify the CEST effect of the tissue-like phantoms in a region of interest indicated by the red dashed line. Thus, it is extremely important to correct for the artefacts induced by the $B_0$ inhomogeneity prior to the quantification.

Shimming is usually the first step that can improve the homogeneity of the magnetic field. However, since it is often performed based on the NMR signal from a whole volume, some local regions of interest probably still have some different frequency offsets which can affect the applied selective RF irradiation. Therefore, a z-spectrum with an evenly distributed sampling across the investigated frequency range is usually acquired, so that a polynomial or cubic spline fitting can be used to correct for the inhomogeneity on a pixel-by-pixel basis [22, 46, 49, 107]. Although this is a viable correction method if the sampling interval is small, the

method is not so sensitive to the shift and may fail to interpolate correctly when the samples are sparse and noisy.

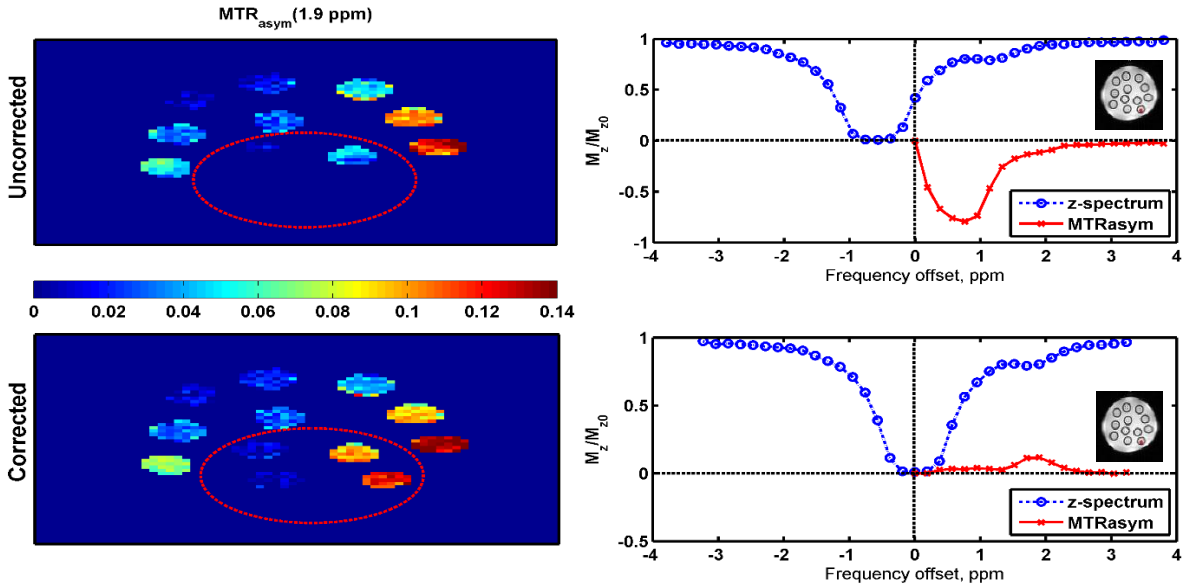


**Figure 2.8: The influence of $B_0$ inhomogeneity. Top row shows the uncorrected $MTR_{asym}$ and z-spectrum. When there is a shift regarding the water centre frequency, $MTR_{asym}$ spectrum (red) cannot detect the presence of CEST agents in the phantoms. For the corrected z-spectrum at the same voxel, the $MTR_{asym}$ spectrum clearly shows the presence of amine protons at 1.9 ppm.**

A $B_0$ field map, produced using different phase images by varying the echo times, has also been used to correct for the field artefacts [105]. Although this method has been shown to be useful for small $B_0$ shifts, it may not be applicable for large frequency shifts such as those found in *in vivo* human data [74]. Additionally, the field map is generated using an acquisition scheme that is different from the APT imaging, so there may be a mismatch in field-based image distortion between the datasets.

Pure direct water saturation imaging can be obtained by using a sufficiently short RF irradiation duration and a small power to minimize the MT effects. This has been shown to be able to measure the absolute water resonance in each voxel; thus, allowing proper centring of the water centre frequency on a voxel-by-voxel basis, independent of spatial $B_0$ field variations [74]. The advantage of this approach is that the water saturation shift referencing

(WASSR) map is generated using the same acquisition schemes as the APT imaging, avoiding any mismatch in field-based image distortions and it can be used to correct for large water frequency shifts. However, the map is acquired either before and/or after the APT experiment which requires around 1 - 2 minutes extra per scan (more sampling points take longer).

In order to quantify the APT effect accurately, the asymmetry analysis and three offset measurement require either the $B_0$ or WASSR map to correct for the shift of water resonance due to the $B_0$ inhomogeneity. LDA and model-based analysis can correct for this artefact through the data fitting process because each of these methods has a parameter (Eqn. (18) and (8)) to account for the shift.

In addition to the $B_0$ field correction, compensating for the $B_1$ field inhomogeneity is also crucial. For a 1.5 T MRI scanner, homogeneity can be achieved reasonably well with body coil excitation but it becomes more difficult at the higher field strength as a result of the limitation in wavelength with respect to the size of the brain [28]. From measurements obtained in 7 T scanners, the excitation efficiency is often found to be higher at the centre of the brain which may be problematic for APT imaging [28]. A double angle method [108] has been used to find the $B_1$ power distribution based on the ratio of image intensities obtained from the flip angle of the RF pulses equal to 60 and 120° [105, 109]. However, since this method uses an imaging acquisition scheme that is different from APT imaging, there may be some discrepancies between the RF power distributions of the two.

Model-based analysis can cater for the $B_1$ inhomogeneity when fitting the data because there is a RF irradiation parameter in the model ($\omega_1$) to account for this artefact, which is a common issue for any CEST experiment. None of the other different quantification

methods mentioned above can correct for this variation in the measurement without having a separate acquisition such as the double angle method.

### 2.3.3 Inherent Asymmetry in the *In Vivo* Z-spectrum

When CEST imaging is performed, MT also affects the net magnetization [110]. MT occurs mainly due to the dipole-dipole interaction between water and large macromolecule protons which have the same Larmor frequency as water [111, 112]. Thus, when a CEST experiment is performed, the bulk water pool experiences both CEST and MT effects. The CEST effect is pH dependent whereas MT is not [110]. The nuclei involved in the chemical exchange with the water protons are usually freely moving in the solution, unlike the nuclei that interact with water protons in MT which are normally immobile macromolecules such as lipids, membrane, myelin and bound proteins. The CEST bound protons have a longer transverse relaxation time, $T_2$ (milli-seconds) when compared to the bound protons involved in MT (micro-seconds) [34]. The line width of a signal, which is defined as the width of the frequency range where the signal becomes half of its maximum, is inversely proportional to the transverse relaxation time; therefore, the CEST effect is only seen around the resonance of the bound protons (Figure 2.5) whereas the MT effect has a broad resonance centred at the bulk water frequency, affecting the whole CEST spectrum as a result of the $T_2$ difference [34, 110-112].

Recent studies have shown that the assumptions made by the asymmetry analyses ($MTR_{asym}$ and $MTR_{asym_comp}$) will not hold, especially in the *in vivo* cases, due to inherent asymmetries in the MT or transfer of nuclear spin polarization from one nuclear spin population to another spatially-close spin population via dipole-dipole cross-relaxation which is termed as the nuclear Overhauser effects (NOE), resulting in a broad saturation effect

across the negative frequency offsets [21, 29, 88, 113] as shown in Figure 2.9: these effects are collectively grouped as MTR'$_{asym}$ here. Although the complementary approach is claimed to perform better than the widely used MTR$_{asym}$ in the biological environment, it still suffers from the same confounding factors at the negative offsets.

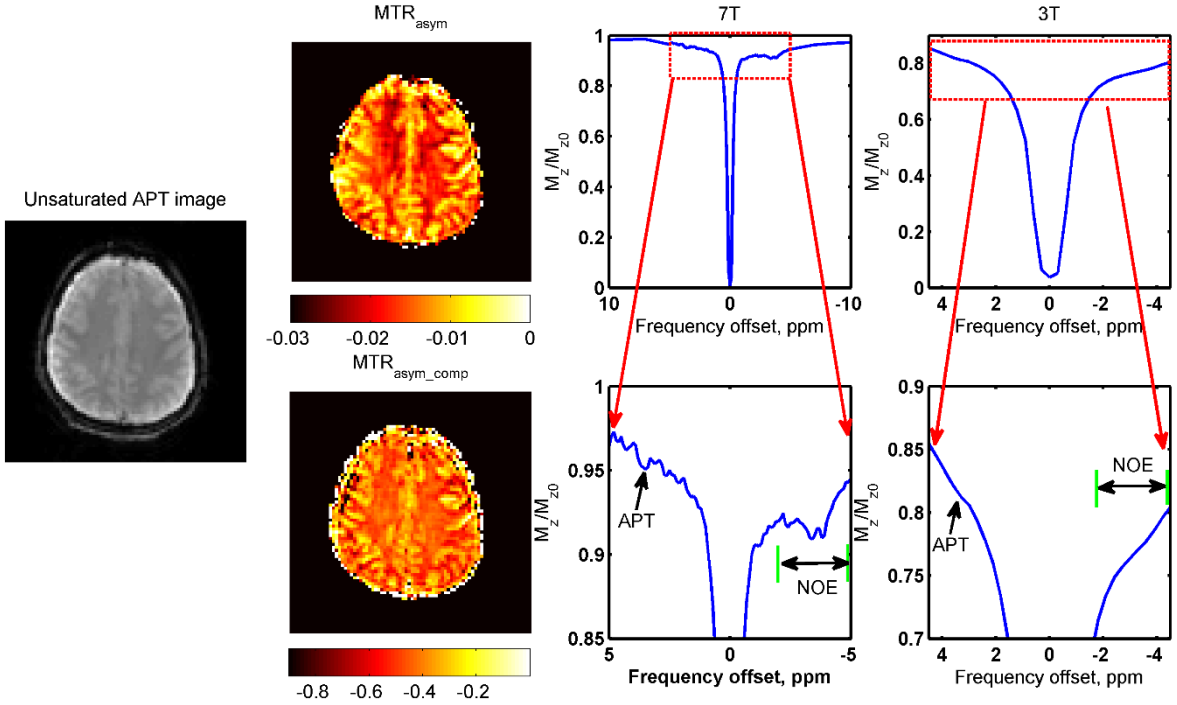


**Figure 2.9: Unsaturated APT, MTR$_{asym}$ and MTR$_{asym_comp}$ images of a healthy subject scanned at 7T, where the asymmetry analyses have negative amplitude due to a broad saturation effect at the negative offsets; z-spectra of a region of interest in white matter of a healthy subject scanned at 3 and 7T, and their respective zoomed in z-spectra indicated by the red dashed rectangular boxes are plotted directly below them. The sampling interval of 3T z-spectrum is bigger (0.3 ppm) than the 7T counterpart (0.1 ppm).**

Hence, quantifying the APT effect by applying the widely used asymmetry analyses contains not only the APT effect (APTR), but also contributions from other transfer of magnetization effects:

$$MTR_{asym} = MTR'_{asym} + APTR\,. \qquad (20)$$

As a result of the contributions from MTR'$_{asym}$, quantification of the APT effect using the above metric often results in negative amplitude when a low power is used, which contradicts with

the saturation effect (positive difference) [44, 104], thus any pH estimation based on this may be more strongly influenced by $MTR'_{asym}$.

Furthermore, asymmetries in the MT have recently been shown to be pH sensitive under low power saturation [113], making the use of signals measured at the negative offset less suitable as reference for APT quantification. Examples of the unsaturated APT, $MTR_{asym}$ and $MTR_{asym_comp}$ images of a healthy subject scanned at 7 T and also the z-spectra acquired using different field strengths are shown in Figure 2.9.

### 2.3.4 Physiological Changes after Stroke

In the previous sections, some of the limitations of quantification methods due to the common factors that affect any CEST experiments were discussed. In this section, issues that are more related to stroke are presented.

Most of the novel potential APT imaging applications have previously been tested in a pre-clinical model under a well-controlled environment, but this is generally not the case in the clinical scenario. Assumptions such as negligible change in the relaxation time of the water pool and concentration may hold during the hyper-acute stroke period, however, these remain to be verified in the clinical setting. For APT imaging performed outside this time window, there is a very high possibility that these assumptions may not remain valid because of secondary phenomena such as oedema formation and inflammation. In addition, there may be a change in the amide proton concentration due to cell depolarisation and loss of cytoplasm in the hours, days and weeks after ischemic onset, as previously discussed.

Previous studies have used different inversion and echo times to produce $T_1$ and $T_2$ maps, respectively, to estimate the relaxation time variations following stroke [50, 88, 91].

Several others have proposed using multiple RF saturation powers [114] and times when performing the CEST experiment to calculate the labile proton exchange rate [100] or both the labile proton exchange rate and concentration [115, 116]. However, these multiple saturation power and time methods have mainly been tested on tissue-like phantoms or *ex vivo*; their practicality remains to be verified for *in vivo* applications.

In order to account for all these variations, various other acquisitions such as $B_0$ or WASSR map, relaxation time maps and multiple RF saturation power and time APT experiments are required, resulting in the patient scan time increasing beyond what is suitable for clinical stroke diagnosis. Since clinicians only have a limited time to determine the treatment plan for the patients, it is almost impossible to run all the tests and to find out the required parameters. Thus, most of the quantification methods introduced above do not meet the requirements for clinical stroke imaging, suggesting that a model-based analysis, which can account for all these variations without requiring extra scans other than the APT imaging, should be used.

However, model-based analysis also has its limitations. It can incorporate all the above-mentioned variations in the parameters at the expense of a longer post-processing time because multiple parameters need to be estimated from the data. This increases the risk of over fitting the data, leading to estimation of the parameters that reflect random noise more than the underlying signal of interest.

Furthermore, since only pulsed APT imaging can be performed clinically due to SAR and hardware limitations, there is no simple analytical solution such as Eqn.(8) for model-based analysis. Finding the proton MR behaviour in response to time varying RF power as present in the pulsed APT imaging is time consuming because the solution to the general

modified Bloch equations (Eqn.(7)) must be arrived at either by using a numerical differential equation solver or by discretizing the pulses into a series of short continuous RF segments. In the latter method, the individual segments are then solved using the simple continuous analytical solution by propagating the magnetization through each of the segments, with the final values from one segment serving as the initial conditions for the next one [31, 110]. Due to the combination of the repeated calculations required and the multiple iterations within the data fitting process, this model-based analysis of pulsed APT imaging is often deemed too slow for practical use.

## 2.4 Summary

10 years after the first published APT paper demonstrated the potential use of APT imaging to identify tissue at risk of infarction in an animal model [22], none of the literature to date has been able to reproduce the pre-clinical results clinically. Clearly, the development of APT imaging for clinical translation is still in its infancy. APT imaging in its current form suffers from too many sources of error for clinical stroke imaging, thus the most commonly used asymmetry analysis may not be suitable to quantify the APT effect, highlighting the need of a more sophisticated approach such as model-based analysis to correct for the various confounding factors.

In this thesis, the study focus is on moving from qualitative (asymmetry analysis) to quantitative and reproducible measures (model-based analysis), improving the APT experimental protocol, speeding up the model-based analysis and assessing the efficacy of the different quantification methods on the data acquired from hyper-acute stroke patients. This is done to facilitate clinical translation of APT imaging and to improve stroke diagnosis.

# Chapter 3

# Optimal Sampling Schedule for CEST*

* Reproduced with permission from John Wiley and Sons. This chapter has been published in the Magnetic Resonance in Medicine (MRM).
Y.K. Tee, A.A Khrapichev, N.R. Sibson, S.J. Payne, and M.A. Chappell, "Optimal Sampling Schedule for Chemical Exchange Saturation Transfer", Magnetic Resonance in Medicine, 70:1251-1262, 2013.

# 3.1 Introduction

The $MTR_{asym}$ is the most commonly used metric to quantify the CEST effect. The simplest CEST acquisition technique is to saturate at the labelled ($\Delta\omega$) and reference scans ($-\Delta\omega$), and to acquire an unsaturated image to quantify the CEST effect using $MTR_{asym}$ [50, 88]. However, a shift of water centre frequency away from the expected value is a common issue in a CEST experiment due to the main magnetic field inhomogeneity [28]. This shift means that any applied RF saturation is not necessarily happening at the offset relative to water resonance that was specified. As a result, the calculated $MTR_{asym}$ may not necessarily reflect the actual CEST effect at the resonance frequency of the labile pool. Correction for artefacts induced by this inhomogeneity is important; various techniques have been used such as $B_0$ field map [105], WASSR [74] and polynomial or cubic spline method [22, 46, 49].

Conventionally, the sampling schedule for CEST imaging is evenly distributed across the saturation frequency offsets [32, 67, 71, 105, 117]. However, this evenly distributed sampling schedule (EDS) is not ideal, especially for *in vivo* applications, because the CEST effect is relatively small, about 2 – 6 % of the water signal [29], and measurement noise or error can easily destroy the signal. To obtain higher SNR measurements, more data acquisitions have been placed at and around the resonance frequency of the labile pool and also its mirror frequency about the water resonance [49, 53].

Although the latter sampling schedule is more tailored, it is simply empirical and not necessarily optimal. Some of the collected samples are still minimally informative to the parameter of interest such as labile proton exchange rate, which has been found to be correlated to intracellular pH [22]. This can be shown from the simulated z-spectra in Figure

3.1, generated using the modified Bloch equations [42, 43]. In this figure, negligible change to the z-spectra is evident at the majority of frequency offsets, except near the resonance frequency of the labile pool when amine proton concentration or exchange rate varies. Since most of the model parameters can be determined relatively accurately prior to the CEST experiment, it is not necessary to sample at the frequency offsets that are not informative to the parameters of interest.

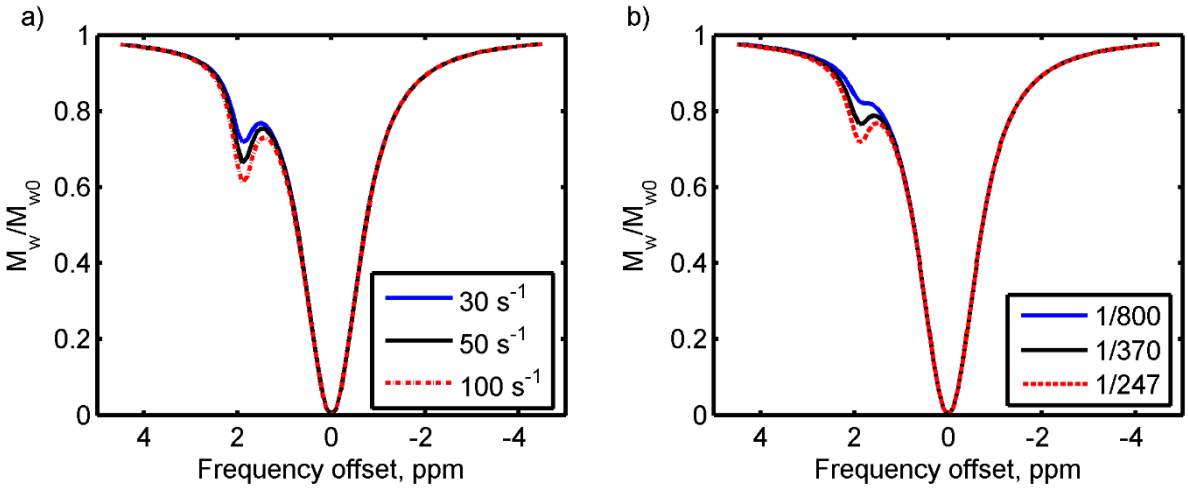


**Figure 3.1: Simulated z-spectra using a 2-pool exchange model (water and amine protons). The parameter values used were set according to Sun et al. [99], unless otherwise stated: (a) varying the amine proton exchange rate while setting the amine to water proton concentration ratio to 1/247; and (b) changing the amine to water proton concentration ratio with amine proton exchange rate set to 30 $s^{-1}$. When either of the parameters varied, there was negligible change on the z-spectra at all the frequency offsets, except near the resonance frequency of amine pool (1.9 ppm).**

In this chapter, an optimal sampling schedule (OSS) is proposed, based on the sensitivity functions that describe how sensitive the data are to changes in the parameter values at a particular saturation frequency offset, to maximize the useful information present in the measured data. Quantitative model-based analysis is then performed pixel-wise by fitting the modified Bloch equations to the z-spectra collected using an EDS and OSS. The important quantified model parameters are examined using simulations and tissue-like phantoms to evaluate the potential benefits of this new type of CEST sampling schedule.

# 3.2 Theory

When a RF irradiation pulse is applied to the exchanging pools, the MR behaviour of protons in each pool can be modelled by the modified Bloch equations in section 2.3.3. These coupled equations are linear and can be arranged in the following form (Eqn. (7)) [42, 43]:

$$\frac{d\boldsymbol{M}}{dt} = \boldsymbol{AM} + \boldsymbol{B}\,,$$

where $\boldsymbol{M}$ is a vector that consists of magnetization of each pool in the *x*, *y* and *z* direction; $\boldsymbol{A}$ is the coefficients of the magnetizations ($\boldsymbol{M}$) which consist of the exchange rate, relaxation rate and resonance frequency of each pool, and also the frequency and power of the RF irradiation; and $\boldsymbol{B}$ is the ratio of initial magnetization in the *z* direction over longitudinal relaxation time of each pool. The details of the multi-pool exchange model used in this study are given in Appendix A1.

Under the conditions of steady state and continuous RF irradiation, Eqn. (7) can be solved analytically [42, 43] and the result is as below (Eqn. (8)):

$$\boldsymbol{M} = e^{(\boldsymbol{A}*T_{sat})} * (\boldsymbol{M_0} + \boldsymbol{BA^{-1}}) - \boldsymbol{BA^{-1}}\,,$$

where $\boldsymbol{M_0}$ is the initial magnetization of each pool in the *x*, *y* and *z* direction.

## 3.2.1 Application of Optimal Design to CEST Imaging

The principle behind optimal design is to minimize the variance associated with the parameters of interest estimates. In this work, an optimal sampling strategy was designed using an approach previously applied to MT imaging [118] and arterial spin labelling [119]. Quantitative model-based analysis of a z-spectrum acquired from CEST imaging involves the

minimization of the sum of squared errors between the model prediction and data. Under this cost function, the variance of the parameters can be determined by the matrix below, $\boldsymbol{H}$, containing terms [119]:

$$\boldsymbol{H} = \begin{bmatrix} H_{jj} & \cdots & H_{jk} \\ \vdots & \ddots & \vdots \\ H_{kj} & \cdots & H_{kk} \end{bmatrix}, \text{where } H_{jk} = \sum_{i=1}^{N} \left[\frac{\partial \boldsymbol{M}(f_i;\boldsymbol{p})}{\partial p_j} \frac{\partial \boldsymbol{M}(f_i;\boldsymbol{p})}{\partial p_k}\right], \tag{21}$$

$\boldsymbol{M}(\boldsymbol{f};\boldsymbol{p})$ is the model (modified Bloch Equations) as a function of model parameters, $\boldsymbol{p}$; and $\boldsymbol{f}$, the sampling points (saturation frequency offsets in this case). The differential terms (with respect to each parameter) represent the sensitivity functions which describe how sensitive a parameter is at a particular frequency offset.

The aim of optimal sampling strategy is to choose $\boldsymbol{f}$ such that the variances associated with the parameters of interest are minimized. This can be achieved by maximizing the property of $\boldsymbol{H}$. The D-optimality criterion is used in this study whereby the strategy is to maximise the determinant of $\boldsymbol{H}$ by varying the sampling schedule, $\boldsymbol{f}$.

## 3.2.2 Quantification of CEST Effect for Model-based Analysis

$MTR_{asym}$ is most generally used to quantify the CEST contrast by combining the effects of labile proton exchange rate and concentration. An equivalent single metric can be derived in the case of model-based analysis to quantify the CEST effect. In that case, the model parameters obtained from fitting the modified Bloch equations to the measured data are used to generate an ideal 2-pool z-spectrum that involves only water and labile protons and the derived measure, CESTR*, is calculated by comparing it to an ideal 1-pool model of water also using the parameters from the multi-pool fit [44]:

$$\mathrm{CESTR}^{*} = \frac{[M_w(\Delta\omega) - M_{w+cest}(\Delta\omega)]}{M_{w0}}, \tag{22}$$

where $M(\Delta\omega)$ refers to the simulated magnetization at the resonance frequency of the labile pool ($\Delta\omega$ = 1.9 ppm in this study) using the fitted parameters, the subscripts *w + cest* and w denote either the ideal 2- and 1-pool model, respectively, and $M_{w0}$ is the unsaturated water signal. (Note: Whilst a greater number of pools can be used to fit the measured data as required, only the fitted model parameters of the water and labile pool are used to calculate the CESTR* to isolate the CEST effect.)

# 3.3 Materials and Methods

## 3.3.1 Numerical Simulation

### *3.3.1.1 Sensitivity Functions*

A 2-pool exchange model (water and amine pools labelled as w and cest, respectively) was modelled using the modified Bloch equations as shown in Appendix A1. Three parameters were chosen for which the variances were to be minimized: amine proton exchange rate, $k_{cest}$, amine proton concentration, $M_{cest0}$ and water centre frequency offset, $\omega_w$; $\boldsymbol{p}$ = [$k_{cest}$, $M_{cest0}$ and $\omega_w$]. $k_{cest}$ and $M_{cest0}$ were chosen because the first is pH dependent [22, 50, 100] and they both affect the magnitude of CEST effect [43, 100, 115]. Consequently, it is important to maximize the information of the collected data for these two model parameters. Optimization was also performed for $\omega_w$ since it is necessary to account for shift, which is unavoidable, due to the main magnetic field inhomogeneity [47, 74, 105].

Forward finite differences were used to approximate the sensitivity function for the parameters of interest because it is non-trivial to differentiate Eqn. (8), which consists of an

exponential matrix with 6 x 6 elements for a 2-pool exchange model. The interval parameter, *h*, for the finite differences was set as 1e-6 for all the parameters of interest investigated.

#### *3.3.1.2 Algorithm for Finding the OSS*

An OSS was generated starting from an EDS using an iterative search algorithm proposed by Xie et al. [119]. Briefly, the optimization proceeded by changing the frequency offsets in the sampling schedule, $\boldsymbol{f}$, sequentially according to a searching resolution ($r$ = 0.1 ppm). For each iteration, all the saturation frequency offsets were varied one by one until the search reached the last element of $\boldsymbol{f}$ and the best cost function found (det($\boldsymbol{H}$)) was recorded. The process was repeated until the difference in the cost function between the current and previous iterations was smaller than a predefined tolerance (1e-16). The algorithm can be summarized as below:

1. One saturation frequency offset was selected every time and the searching bounds were set to be its immediate neighbouring offsets.
2. By varying the selected offset according to *r*, if the modified saturation frequency offset contributed to a higher cost function than the previous sampling schedule, the changed offset was updated as the latest sampling schedule, else it would revert back to its original value.
3. Step 1 and 2 were repeated until the last element of $\boldsymbol{f}$ had been examined. The sampling schedule which generated the biggest cost function once the algorithm reached the last element was retained and compared with the best cost function found from the previous iteration. If the difference was larger than the tolerance, the search started from the first element again and step 1, 2 and 3 were repeated, else the algorithm stopped.

In practice, the OSS may propose sampling multiple times at one saturation frequency offset to maximise the information present within the measured data.

In order to obtain an OSS for a more realistic case in which the values of the parameters of interest were unknown, the search algorithm was performed for multiple combinations of 'true' values for the parameters sampled from plausible distributions of their values. These distributions were taken to be Gaussian with the following means and standard deviations (optimized ranges): $k_{cest}$ = 50 ± 35 $s^{-1}$, $\omega_w$ = 0 ± 0.2 ppm and $M_{cest0}$ = 0.27 ± 0.07 M. Assuming a water proton concentration of $M_{w0}$ = 100 M, the resulting optimized range of amine to water proton concentration ratio became $M_{cest0}/M_{w0}$ = 0.0027 ± 0.0007.

1000 randomly sampled $k_{cest}$, $M_{cest0}$ and $\omega_w$ sets of values were selected from their Gaussian distributions and fed to the search algorithm to find the OSS for each pair of them. The final OSS was acquired by summing all the optimal saturation frequency offsets found and then normalizing it. The resultant was rounded to the nearest integer so that the final OSS had the same number of saturation frequency offsets as the EDS.

#### *3.3.1.3 Validation of OSS with Simulated Data*

The performance of the OSS obtained was examined using simulated data within and outside the optimized ranges of the parameters of interest: $k_{cest}$ was varied from 10 to 90 $s^{-1}$ with intervals of 10 $s^{-1}$, $M_{cest0}$ was changed from 0.15 to 0.39 M with increments of 0.03 M (equivalent to 0.0015 to 0.0039 for $M_{cest0}/M_{w0}$) and $\omega_w$ was set to change from -0.4 to 0.4 ppm with intervals of 0.2 ppm.

An evenly distributed z-spectrum was simulated for each set of $k_{cest}$, $M_{cest0}$ and $\omega_w$ values. From this, 1000 datasets were created by adding white Gaussian noise with standard

deviation equal to 1, 2 and 5 % of the unsaturated signal (SNR = 100:1, 50:1 and 20:1) to the simulated z-spectrum. For the OSS case, the same procedure as the EDS was applied, except the replicated data were generated according to the optimized sampling frequencies found. The total number of noisy simulated z-spectra for each SNR and sampling schedule was 405,000 (9 different $k_{cest}$ and $M_{cest0}$ values each, 5 different $\omega_w$ offsets and each combination of the three parameters was replicated 1000 times). The noisy z-spectra were fitted to a 2-pool model sampled by OSS and EDS using the nonlinear least-square curve fitting function, *lsqcurvefit* in MATLAB (Mathworks, Natick, MA, USA).

Normalized RMS errors for the important fitted model parameters ($k_{cest}$, $M_{cest0}$ and $\omega_w$) against the 'true' values were calculated for each sampling scheme to assess its performance within and outside the optimized range. When all of the parameters of interest were within the optimized range, the RMS errors were recorded in the 'optimized' category of each parameter whereas when one or more of the parameters were not in the range for which the OSS was optimized, the average calculated errors were assigned to an 'unoptimized' category of each of them.

The majority of simulations used an EDS from -3.8 to 3.8 ppm with intervals of 0.1 ppm, resulting in a total number of acquisitions (NA) of 77. In order to investigate the performance of the different sampling schedules further, an additional set of simulated data was generated with SNR = 50:1 and NA = 20; the EDS was set to have the same start and end saturation frequency offsets but with intervals of 0.4 ppm and the OSS was reduced proportionally from the higher NA study to match it. The other variables in the modified Bloch equations were treated as constant: relaxation parameters of water and amine protons were

$T_{1w}$ = 3 s, $T_{1cest}$ = 1 s, $T_{2w}$ = 60 ms, $T_{2cest}$ = 8.5 ms [89]; saturation time, $T_{sat}$ = 15 s; continuous RF power, $B_1$ = 0.4 μT and resonance frequency of the CEST pool, $\omega_{cest}$ = 1.9 ppm [89].

## 3.3.2 *In Vitro*

#### *3.3.2.1 Phantom Preparation*

Tissue-like phantoms were prepared according to [105] using creatine and agarose (Sigma Aldrich, St. Louis, MO, USA). Creatine was added to deionized water first to reach a concentration of 100 and 125 mM in two different containers. Once the creatine had fully dissolved, agarose was added to form 3 % of the mixed solution and then heated to boiling. After that, the mixed solution was maintained at 50 °C and titrated to pH values of 5.3, 5.6, 6 and 6.4 before being transferred to different 2 ml vials. In order to minimize the magnetic field inhomogeneity, a plastic container was used to house all the tubes and filled up with agar. The phantoms were left to solidify at room temperature prior to the MRI experiments.

#### *3.3.2.2 MRI Experiments*

All images were acquired on a 4.7 T Varian DirectDrive™ spectrometer (Agilent Technologies, Santa Clara, CA, USA) at room temperature. The $B_0$ was shimmed to minimize the field inhomogeneity artefacts and the RF field was calibrated before experiments. 250 Gaussian pulses with flip angle of 123° were used to saturate the pH phantoms and crusher gradients with alternating signs were applied after each irradiation pulse to spoil the residual transverse magnetization. Each such cycle was 40 ms long – 20 ms for an irradiation pulse followed by a crusher gradient. The total irradiation time was 10 s (250 cycles * 40 ms/cycle) to ensure that steady state was achieved. The bandwidth (full width at half maximum) used was 110 Hz. A single-slice EPI readout was used after the RF saturation. The acquired images

had a field of view (FOV) of 80 mm x 80 mm, matrix size of 64 x 64, slice thickness of 1 mm, bandwidth of 250 kHz, echo time (TE) of 20 ms and repetition time (TR) of 15 s.

The CEST imaging using EDS was identical to the simulation; saturation being performed from -3.8 to 3.8 ppm (-760 to 760 Hz for 4.7 T) with increments of 0.1 ppm (20 Hz), corresponding to NA = 77. For the OSS CEST experiment, 77 saturation frequency offsets were sampled according to the optimal schedule found from the simulations. The signal measured at 20 ppm was used as the unsaturated signal ($M_{w0}$) [55]. The CEST data were acquired in about 40 minutes per sampling schedule.

In addition to CEST imaging, $B_1$ field, $T_{1w}$ and $T_{2w}$ maps were also measured. The double angle method [109] was used to find the $B_1$ field map using excitation angles of 60° and 120°. The $T_{1w}$ images were obtained using an inversion recovery sequence with eight recovery intervals from 100 to 6000 ms, the measurement being repeated three times. The $T_{2w}$ map was derived from six separate spin echo images with TEs of 23, 30, 41, 56, 75 and 100 ms, and this was repeated four times.

WASSR was acquired before and after each sampling schedule to determine the water centre frequency shift. The WASSR map for each sampling strategy was produced by averaging the estimated shifts before and after the CEST experiment. The WASSR spectra were acquired using an identical sequence to the CEST acquisition except for the use of only 50 Gaussian pulses with flip angle of 31° and saturation frequency offsets from -0.75 to 0.75 ppm (-150 to 150 Hz for 4.7 T) with intervals of 0.025 ppm (5 Hz). The measured data points were interpolated to intervals of 0.0005 ppm (0.1 Hz) prior to finding the water centre frequency shift using the Maximum Symmetry algorithm [74]. The saturation frequency at which the magnetization was minimum was set as the initial search point.

#### *3.3.2.3 MRI Data Processing*

The $T_{1w}$ and $T_{2w}$ maps, and the model fitting on phantom data were processed using the nonlinear least-square curve fitting function, *lsqcurvefit* in MATLAB (Mathworks, Natick, MA, USA). The relaxation maps of the water pool were obtained by least-square fitting of the measured intensities against the inversion intervals ($T_1$ map) and TEs ($T_2$ map). A 3-pool model, which consisted of water (w), amine (cest) and magnetization transfer (MT) effect, was used to fit the experimental data. A Gaussian lineshape function, which has been found to be more appropriate for tissue-like phantoms prepared using agarose, was used to model the MT effect [112]. The coupled equations for the 3-pool exchange model used in this study are given in Appendix A2.

Since there is no simple analytical solution for CEST acquisition using time dependent Gaussian pulses, each pulse was discretized into 32 short continuous RF segments which should be sufficient to assure accuracy according to [106]. The individual segments were then solved using the simple analytical solution for the continuous case (Eqn. (8)) with the magnetization being propagated through each of the segments, the final values from one segment serving as the initial conditions for the following one [31, 110].

The rest of the parameters in the modified Bloch equations were determined as below: $T_{1w}$ and $T_{2w}$ were determined from the relaxation maps, $M_{w0}$ was set as the signal measured at 20 ppm and $\omega_1$ was derived from the $B_1$ map; the remaining variables in the model were treated as constant where $T_{1cest}$ = 1 s, $T_{2cest}$ = 8.3 ms, $\omega_{cest}$ = 1.9 ppm [89], $T_{1MT}$ = 1 s, $T_{2MT}$ = 15 µs, $C_{MT}$ = 48 $s^{-1}$, $M_{MT0}/M_{w0}$ = 0.021 [32], $\omega_{MT}$ = fitted $\omega_w$ [99] and $T_{sat}$ = 10 s.

The coefficient of variation (CV) (standard deviation divided by mean) of the fitted model parameters ($k_{cest}$ and $M_{cest0}$) were calculated to assess the performance of the sampling

schedules. The estimated water centre frequency shift ($\omega_w$) was compared with the WASSR map using the RMS error. CESTR* was calculated for each sampling schedule and the obtained values were compared with the conventional $MTR_{asym}$ generated from the EDS measured data. For inter-sampling schedule comparison, the standard deviation of CESTR* across each concentration and pH phantom was examined.

# 3.4 Results

## 3.4.1 Numerical Simulation

Normalized sensitivity functions of $k_{cest}$, $M_{cest0}$ and $\omega_w$ for one fixed set of parameters are shown in Figure 3.2. The first two parameters ($k_{cest}$ and $M_{cest0}$) were found to be most sensitive around the chemical shift of creatine (1.9 ppm) and $\omega_w$ had high sensitivity at ± 0.3 and 0.4 ppm. For this set of parameters, the search algorithm proposed sampling repeatedly near 0.4, 1.9 and 2.2 ppm with a few samples at -0.4 ppm, which mainly reflected the high sensitive frequency offset of each parameter of interest and at 2.2 ppm where all the parameters of interest were moderately sensitive.

When the parameters of interest were selected randomly from their Gaussian distributions, the search algorithm proposed the OSS given in Figure 3.3. The placement of the sampling points from -0.6 to 0.7 and 1.3 to 2.4 ppm with intervals of 0.1 ppm broadly reflected the sensitivity functions shown in Figure 3.2 with samples placed near the creatine and water resonances. The smaller NA OSS had saturation frequency offsets from 0.2 to 0.5 ppm and 1.5 to 2.3 ppm with increments of 0.1 ppm; 2 samples were acquired at 0.3 and 0.4 ppm, and from 1.7 to 2.1 ppm with intervals of 0.1 ppm and the rest of the frequency offsets in this reduced NA OSS study were sampled once.

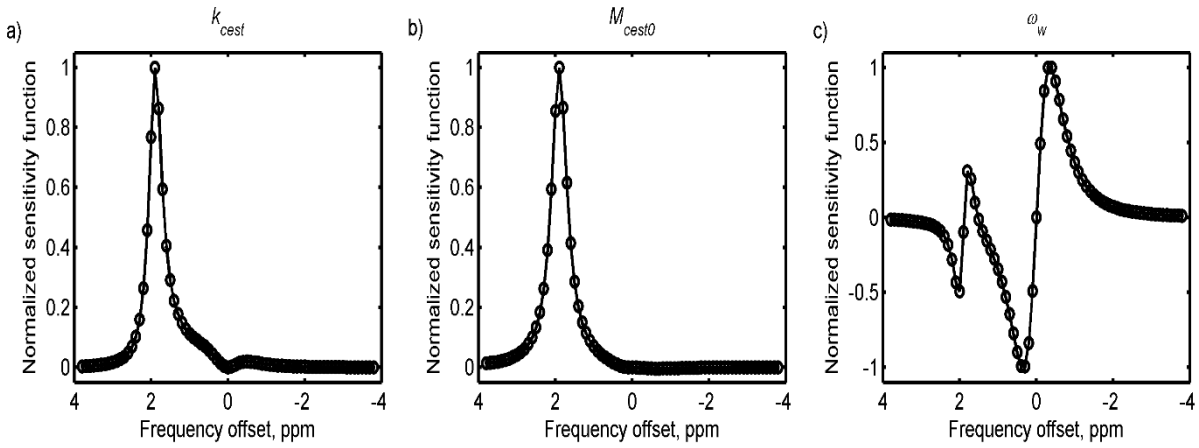


**Figure 3.2: Normalized sensitivity function for (a) amine proton exchange rate, $k_{cest}$; (b) amine proton concentration, $M_{cest0}$; and (c) water center frequency shift, $\omega_w$, for a 2-pool exchange model. The parameters of interest were set as $k_{cest}$ = 50 $s^{-1}$, $M_{cest0}$ = 0.27 and $\omega_w$ = 0, other model parameter values were as given in the Materials and Methods section (sensitivity function was normalized to the highest magnitude of the function).**

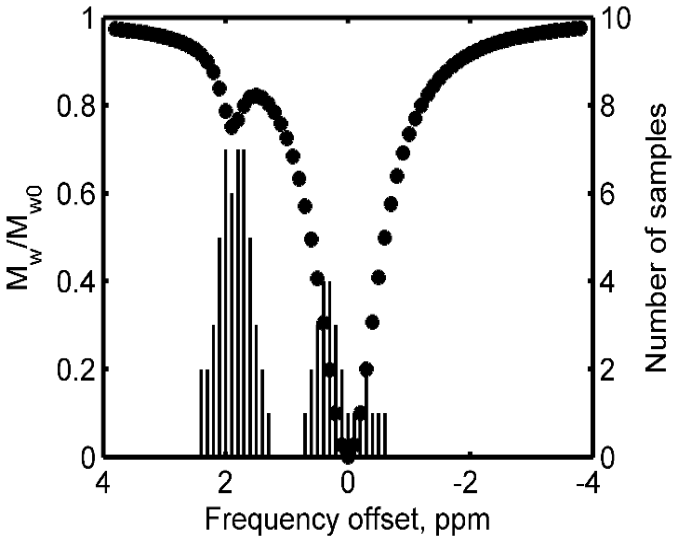


**Figure 3.3: OSS found from 1000 random samples (NA = 77). The z-spectrum (dots) was simulated using the parameter values applied to generate the results in Figure 3.2. The bar graph (vertical lines) represents the sampling points and the height of the bars refers to the number of samples for the OSS. The OSS sampling points from right to left are -0.6 to 0.7 and 1.3 to 2.4 ppm with intervals of 0.1 ppm.**

Quantitative model-based analyses were performed on the simulated noisy CEST data using both OSS and EDS, and the results are shown in Figure 3.4. The fitted parameters of interest using OSS were more accurate than the EDS approach for all the SNRs and NAs tested within and beyond the optimized range, except the quantified $\omega_w$ for the smaller NA study.

The RMS error increased when SNR or NA reduced. The biggest improvement was recorded from the highest SNR data, where quantification of parameters of interest using OSS achieved at least 30% smaller error within the optimized range and 15% beyond this range when compared with the fitted values using EDS. Under highly noisy environment (SNR of 20:1), placing the samples according to the OSS led to at least 10% more accurate quantification of parameters of interest than EDS within and beyond the optimized range.

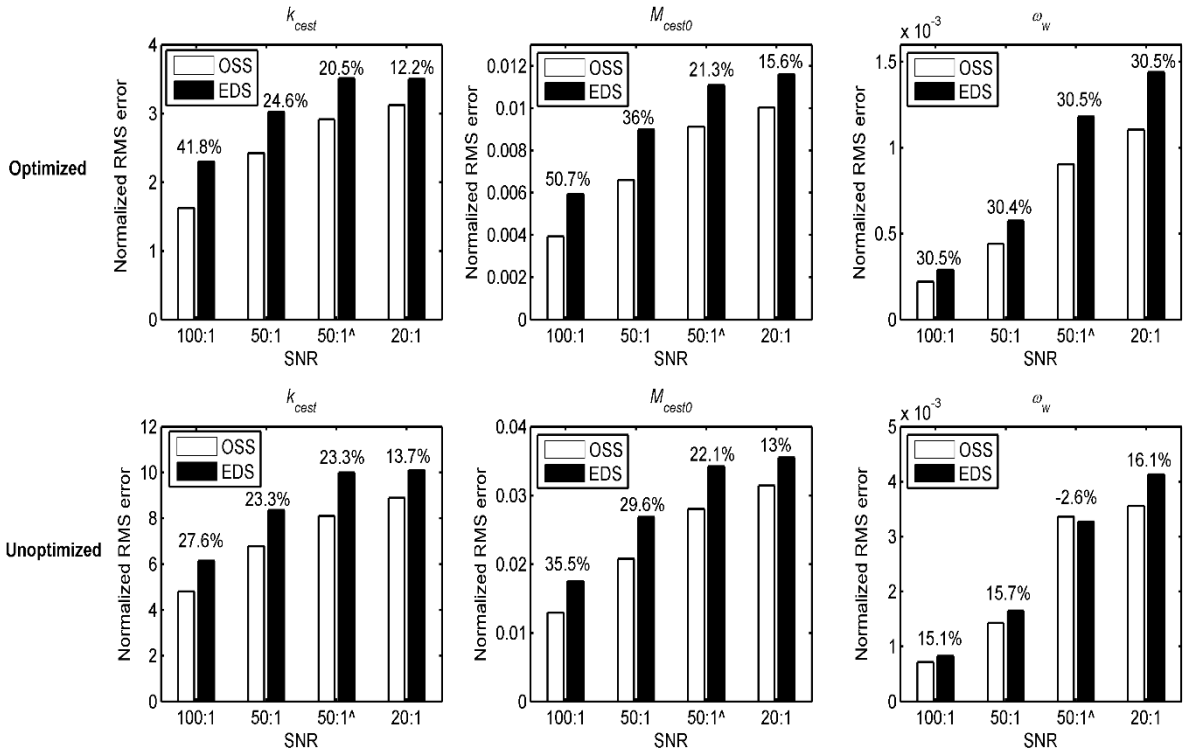


**Figure 3.4: Normalized RMS errors (RMS errors/number of spectra) of the fitted model parameters within (top row) and beyond (bottom row) the optimized ranges for amine proton exchange rate, $k_{cest}$; amine proton concentration, $M_{cest0}$; and water centre frequency shift, $\omega_w$; for different SNR and NA studies. The percentage values above each bar are the differences between the RMS errors of EDS and OSS, where a positive value means OSS was more accurate. ^ refers to the study with NA = 20 which was formed by proportionally reducing the OSS found from the search algorithm with NA = 77.**

## 3.4.2 *In Vitro*

The measured longitudinal and transverse relaxation times of the water pool at 4.7 T were: $T_{1w}$ = 2.25 ± 0.041 s and $T_{2w}$ = 44.7 ± 4.9 ms. Figure 3.5 shows the measured z-spectra

for different creatine concentrations and pH values corrected using the WASSR map. When either pH or creatine concentration increased, the dip of amine pool became larger. The measured results, like the simulated z-spectra in Figure 3.1, showed minimal variation in the majority of saturation frequency offsets except at the resonance frequency of the amine pool when amine proton concentration or exchange rate (pH) varied.

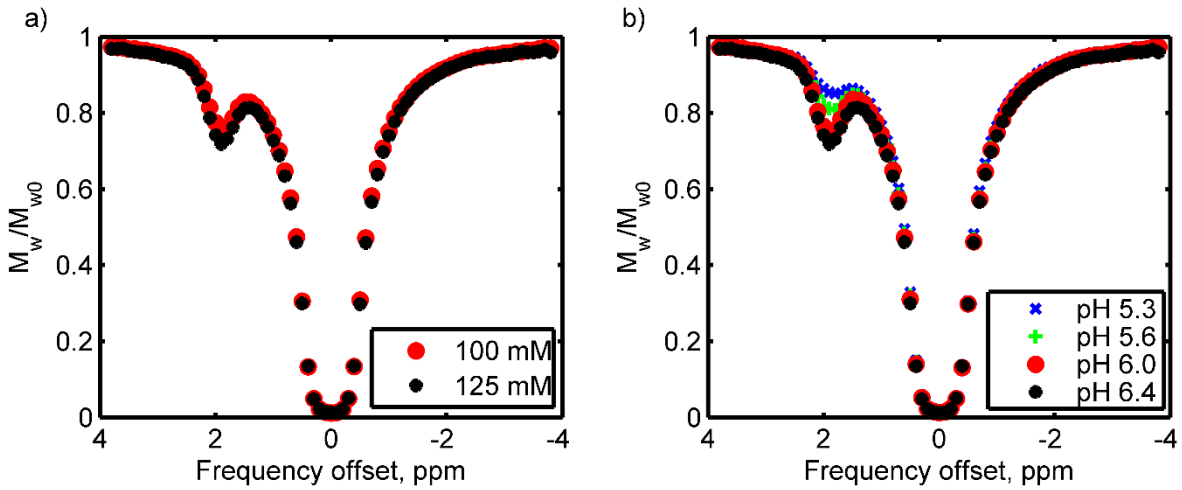


**Figure 3.5: Measured z-spectra of (a) different creatine concentration phantoms at pH 6.4 and (b) 125 mM creatine phantoms with different pH values. Water centre frequency shift was corrected using the WASSR map.**

The estimated water centre frequency shifts due to the field inhomogeneity using the WASSR method (b and d) and quantitative model-based approaches (c and e) are shown in Figure 3.6. The results show that the fitted $\omega_w$ using either sampling schedule matched well to the WASSR estimated shifts. The RMS error between the EDS fitted shifts and WASSR results was 1.66, whereas the calculated RMS error between the OSS and WASSR results was 1.29. Both sampling schedules estimated $\omega_w$ values with less than 0.03 ppm maximum difference from the WASSR estimated shifts.

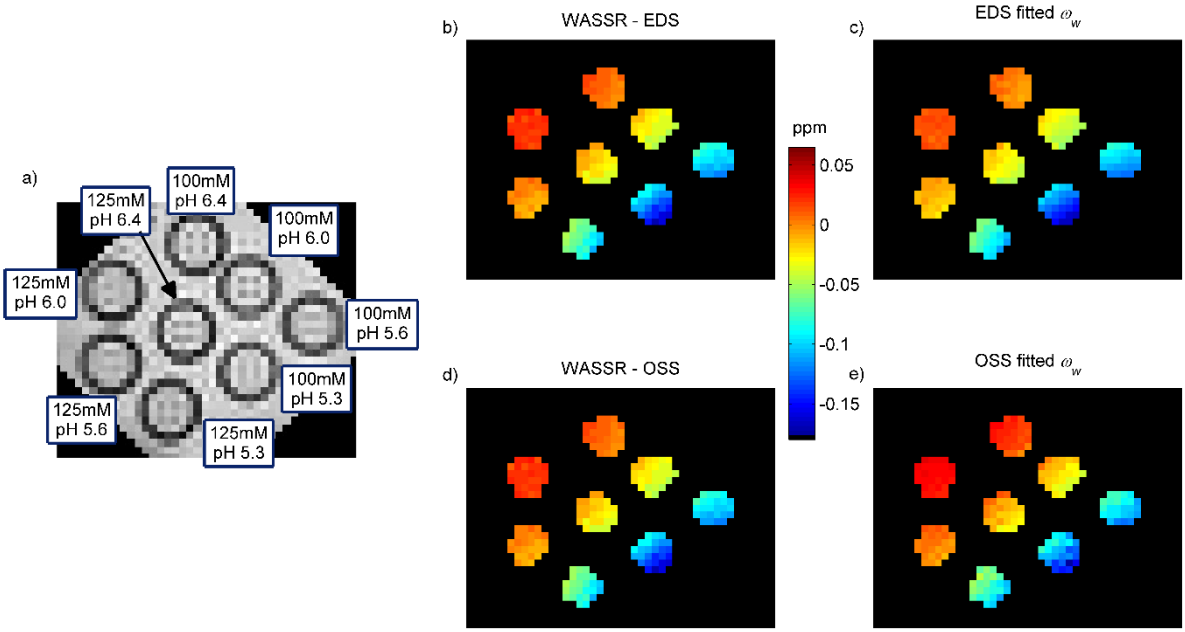


**Figure 3.6: WASSR maps (b and d) and model fitted water centre frequency shifts (c and e). Both the fitted results matched well to the WASSR maps. The arrangement of the phantoms is labelled in (a), where the top numbers represent the creatine concentration and the bottom ones refer to its pH value.**

The fitted values of the other two model parameters of interest are shown in Figure 3.7. The fitted $k_{cest}$ increased when pH increased, likewise an increase was observed for $M_{cest0}$, except for pH 5.3 samples. The difference in CV ($CV_{EDS} - CV_{OSS}$) is recorded in Table 3.1, where positive numbers indicate that the OSS estimates were more precise. The results indicate that the values for $k_{cest}$ and $M_{cest0}$ fitted using OSS were more precise than using EDS, except for the fitted $M_{cest0}$ at pH 6.4.

**Table 3.1: Difference in CV ($CV_{EDS} - CV_{OSS}$) of the fitted amine proton exchange rate, $k_{cest}$, and concentration, $M_{cest0}$. A positive difference indicates the model fitted results from OSS were more precise than EDS.**

| | $CV_{EDS} - CV_{OSS}$ | | | | | | | |
|---|---|---|---|---|---|---|---|---|
| | $k_{cest}$ | | | | $M_{cest0}$ | | | |
| **Phantom** | **pH 5.3** | **pH 5.6** | **pH 6.0** | **pH 6.4** | **pH 5.3** | **pH 5.6** | **pH 6.0** | **pH 6.4** |
| **100 mM** | 0.153 | 0.458 | 0.300 | 0.125 | 0.219 | 0.033 | 0.024 | *-0.009* |
| **125 mM** | 0.060 | 0.084 | 0.349 | 0.205 | 0.101 | 0.074 | 0.013 | *-0.004* |

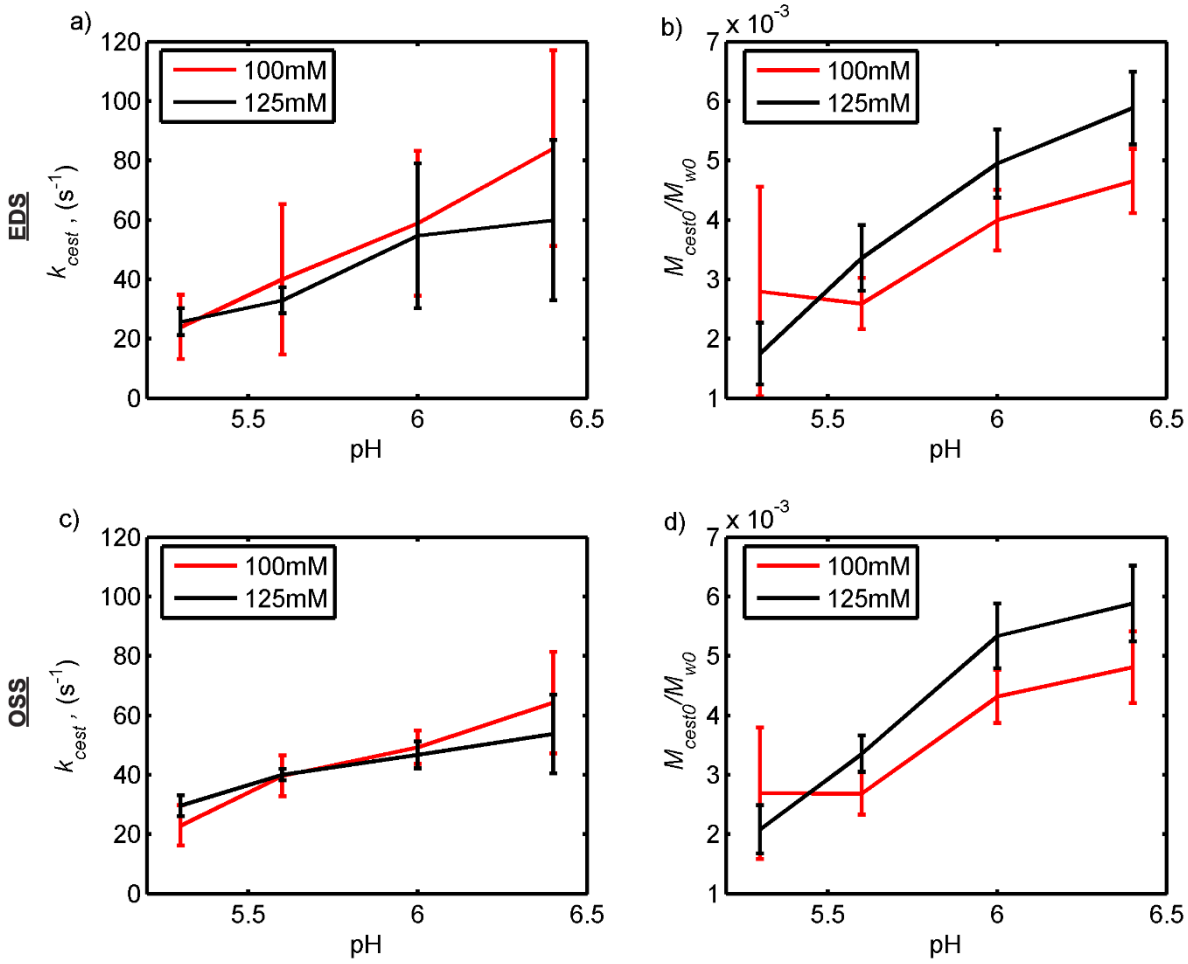


**Figure 3.7: Fitted amine proton exchange rate, $k_{cest}$ (a and c) and concentration, $M_{cest0}$ (b and d) using EDS and OSS for the tissue-like phantoms.**

The calculated CESTR* from both sampling schedules are shown in Figure 3.8. The results show that the CESTR* managed to separate the phantoms with the same concentration but different pH values equally well as the widely used $MTR_{asym}$. The CESTR* obtained from the fitted model parameters using OSS exhibited smaller variation than using EDS for all the different concentration and pH phantoms investigated (Figure 3.8e). The improvement increased dramatically when the CEST effect became smaller. Reducing the pH of the phantom from 6 to 5.6 and 5.3 showed approximately 20% to 30% and 40% smaller variation, respectively, when OSS was used. When the creatine concentration of the phantom changed from 125 to 100mM, smaller CESTR* variation was also observed in which the

phantom with the smallest CEST effect shows close to 60% smaller variation using the proposed method.

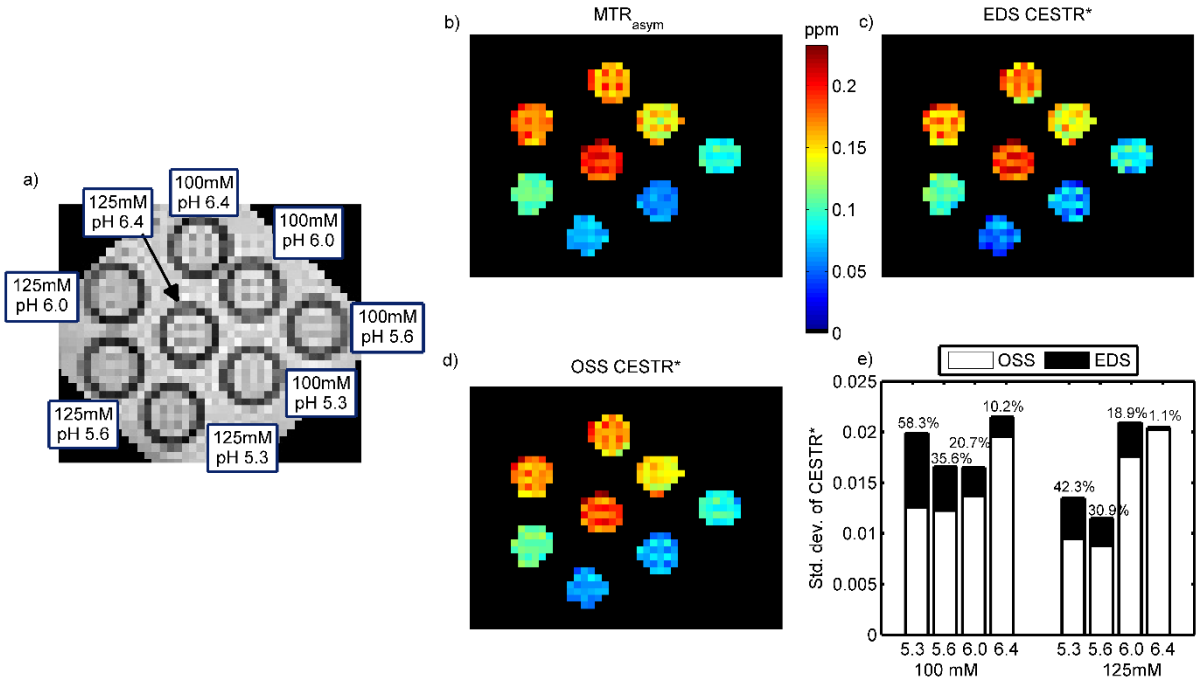


**Figure 3.8: Equilibrium magnetization image labelled with creatine concentration and pH of each sample. b) Conventional $MTR_{asym}$ obtained from the EDS data and CESTR* of (c) EDS and (d) OSS calculated from the fitted model parameters. The CESTR* variations for each phantom are shown in (e); the percentage value on top of each bar is the difference between the standard deviations in CESTR* of EDS and OSS.**

# 3.5 Discussion

This study proposes an optimal sampling strategy to perform data acquisition for CEST imaging. The OSS, which samples repeatedly at the frequency offsets where the sensitivity functions of the parameters of interest have high magnitude, was compared with the conventional EDS using quantitative model-based analysis. As illustrated in the simulations and experiments, variations of certain parameters of interest predominantly affected the signal across a small range of frequency offsets. Consequently, more sampling points should be placed around these frequency offsets to maximise the information present in the collected data so that their accuracy and precision can be improved in model fitting.

When quantitative model-based analysis was performed on the parameters of interest ($k_{cest}$, $M_{cest0}$ and $\omega_w$), OSS was shown to outperform EDS both theoretically (Figure 3.4) and experimentally (Figure 3.6, Table 3.1 and Figure 3.8). The simulated results showed that the quantified parameters using OSS were not only more accurate than EDS within the range of parameters for which the OSS was optimised, but also beyond this range for all the SNRs and NAs tested, except the fitted $\omega_w$ in the smaller NA study. This was caused by the limited number of samples acquired in this study, where the OSS did not acquire any data beyond the optimized range of $\omega_w$, leading to less accurate quantification of this parameter when the out of range values were tested. If the NA was small and the saturation frequency offset range was large such as in the paramagnetic CEST (PARACEST) study, the chance of EDS missing the important information will be high, making the use of OSS very appealing.

In the phantom study, the estimated water centre frequency shifts using OSS, which placed more samples around the water resonance, were more accurate than the fitted results using EDS when compared to their respective WASSR map. The proposed sampling schedule also showed smaller CESTR* variation within a region of homogenous pH and concentration, particularly the samples with small CEST effect where close to 60% improvement was observed (Figure 3.8e). This is especially important for *in vivo* CEST applications given that the CEST effect is very small due to the low concentration of the labile pool; lesser variation would allow better delineation of healthy tissue from pathological tissue, such as ischemic regions or tumours.

In Figure 3.7, the fitted $k_{cest}$ and $M_{cest0}$ both increased with pH for either sampling schedule. In practice, the change of pH should only affect the amine proton exchange rate when the concentration remains constant. Separating the effect of $k_{cest}$ and $M_{cest0}$ on the z-

spectrum is a non-trivial task because these two parameters are closely correlated to each other [44, 110, 114, 115]. Despite this, the CV values indicated that parameters fit from the OSS had higher precision when compared to EDS. Using data acquired with multiple different RF irradiation powers might increase the separability of these two model parameters as evidenced by the methods of an omega plot [114] and the radio frequency power dependence of CEST [115]. OSS, which is optimized to target data collection at the most informative frequency offsets, would still be applicable in this case to propose which offsets to sample and to improve the data fitting. However, the sensitivity functions are likely to vary with RF power. The variation is very small for $k_{cest}$ and $M_{cest0}$, and, thus, the results presented here would still remain applicable, but this is not the case for $\omega_w$; the most sensitive frequency offset for this parameter moves further away from the water resonance as the RF power increases. Since the normalized sensitivity function of $\omega_w$ is RF power dependent, including this model parameter in the OSS design might require the search algorithm to be performed for every RF power used.

For *in vivo* CEST applications, there are multiple labile proton pools that can interact with the water protons, for example glycogen (0.5 to 1.2 ppm) [54, 74, 75], myo-inositol (~0.6 ppm) [55, 56], glutamate (~3 ppm) [81], fat (~-3.5 ppm) [120, 121] and amide protons (~3.5 ppm) [22]. All of these labile pools and transfer of magnetization effects such as MT and NOE (which covers a few ppm upfield from water) [29], have some influence on the collected z-spectrum around their resonance frequencies. As a result, the model-based analysis of the *in vivo* EDS data may have to be performed with a multiple pool system accounting for each source of saturation exchange. A major drawback of having multiple pools in the model-based analysis is the long computational time required for the matrix exponential in the analytical

solution. Furthermore, when the number of pools increases, more parameters have to be fitted from the data leading to the risk of over-fitting the data and, thus, inaccurate results. OSS offers a preferable alternative because the sampling schedule only concentrates around the resonance frequency of the pool of interest, minimizing the contaminant effects from other metabolites and effects. As a result, the number of pools required for quantitative analysis using OSS can be kept to a minimum.

Due to the specific absorption rate (SAR) and hardware limitations of clinical scanners, continuous RF irradiation is not a feasible saturation scheme for CEST imaging, making multiple short and high intensity pulses the only currently suitable irradiation scheme for clinical translation. Performing quantitative model-based analysis using pulsed saturation is time consuming because there is no simple analytical solution like Eqn. (8) for the time-dependent RF power. The OSS derived here was for continuous RF irradiation; the simulated normalized sensitivity functions of the investigated model parameters under pulsed saturation, achieved by multiple short but high intensity Gaussian pulses, are shown in Figure 3.9. There are some differences between the pulsed and continuous normalized sensitivity functions, presented in Figure 3.9 and Figure 3.2, respectively. Nevertheless, the frequency offsets that contributed to the highest normalized sensitivity functions of $k_{cest}$ and $M_{cest0}$ were still the same. Thus, it is likely that the search algorithm would still similarly propose the placement of more samples around the resonance frequency of the labile pool even when a pulsed saturation is applied. There was a slight change to the sensitivity function of $\omega_w$, the peak magnitude of the sensitivity function shifting from ± 0.3 and 0.4 ppm in the continuous case to ± 0.5 ppm for pulsed irradiation. As a result, the true OSS for pulsed irradiation might differ slightly from the sampling frequency offsets presented in Figure 3.3.

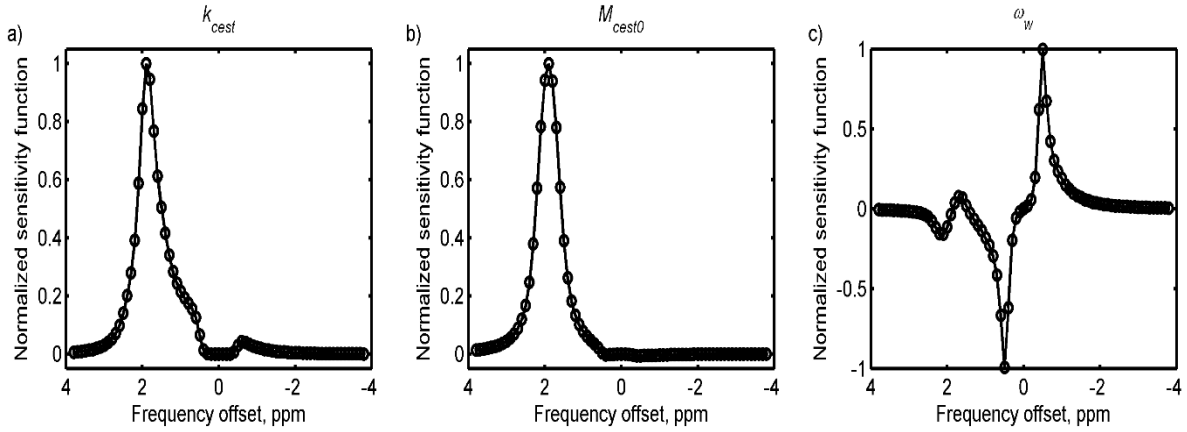


**Figure 3.9: Simulated pulsed CEST normalized sensitivity function plots: (a) amine proton exchange rate, $k_{cest}$; (b) amine proton concentration, $M_{cest0}$; and (c) water center frequency shift, $\omega_w$, for a 2-pool exchange model. $k_{cest}$ and $M_{cest0}$ were most sensitive around the chemical shift of creatine (1.9 ppm) and $\omega_w$ was found to be very sensitive around ± 0.5 ppm. The plots were generated using the same parameter values used to produce Figure 3.2 (sensitivity function was normalized to the highest magnitude of the function).**

Although the OSS was optimized for continuous RF irradiation, it did seem to offer improved estimates for the tissue-like phantom study where pulsed irradiation was employed. Whilst an OSS could be calculated for pulsed irradiation using the same methodology applied here, there would be a cost in terms of a substantial increase in computation time owing to the iterative calculation of magnetization required to discretize the pulses. Given the modest changes in the sensitivity functions, the OSS presented here appears to be sufficient. Likewise, whilst other pulse shapes aside from continuous and Gaussian pulses might be used, the effect on the sensitivity functions might be presumed to be small and thus the current OSS should still be appropriate.

# 3.6 Summary

Studies on simulations and tissue-like phantoms show that the proposed optimal sampling strategy, which samples repeatedly around the frequency offsets that are informative to the parameters of interest, has several advantages over the currently widely

used evenly distributed sampling schedule. The proposed approach could enable better quantification of both the CEST effect and parameter estimation by maximising the information present in the collected data for quantitative analysis.

# Chapter 4

# Evaluating the Use of a Continuous Approximation for Model-based Quantification of Pulsed CEST[†]

[†] Open access article, no permission is required to reproduce the content. This chapter has been published in the Journal of Magnetic Resonance (JMR).
Y.K. Tee, A.A Khrapichev, N.R. Sibson, S.J. Payne, and M.A. Chappell, "Evaluating the Use of a Continuous Approximation for Model-Based Quantification of Pulsed Chemical Exchange Saturation Transfer (CEST)", Journal of Magnetic Resonance, 222: 88-95, 2012.

# 4.1 Introduction

The $MTR_{asym}$ is the most commonly used metric to measure the CEST effect, however, it depends on experimental parameters such as RF power [99] and saturation time [100]. Moreover, the calculated *in vivo* $MTR_{asym}$ includes not only the CEST effect, but also fat/lipid signal which causes artifacts such as banding around [121] or through [120] the brain, MT [122] and NOE [29]. These factors complicate the quantitative analysis of the CEST effect using $MTR_{asym}$, highlighting the need for a model-based approach to separate these effects and to move from a qualitative to quantitative and reproducible measure.

Unlike the $MTR_{asym}$ calculation which only relies on two saturation frequencies, the model-based approach fits a model of saturation exchanges to the data collected from a range of saturation frequencies. The model is based on the modified Bloch equations in section 2.2.3. The simplest model-based analysis of CEST effect consists of two pools: water and CEST agents; more pools can be added to the analysis to model the various extra effects observed *in vivo*. By having a separate pool for each confounding factor in the CEST experiment, a pure CEST effect can be determined from the data correcting for the confounds.

Performing model-based quantitative analysis of the CEST effect for CW-CEST is simple and is generally achieved using the analytical solution to the modified Bloch equations (Eqn. (8)). However, CW-CEST is not feasible in clinical applications due to SAR and hardware limitations, making pulsed CEST the only viable irradiation scheme for clinical translation currently. Finding the proton MR behavior in response to time varying RF power as present in the pulsed CEST scheme for model-based analysis is time consuming because the solution to the modified Bloch equations must be arrived at either using a numerical differential equation

solver or discretizing the pulses into a series of short continuous RF segments. In the latter case, referred to here as the discretization method, the individual segments are then solved using the simple analytical solution for CW-CEST (Eqn. (8)) with the magnetization being propagated through each of the segments, the final values from one segment serving as the initial conditions for the next one [31, 110].

Due to the combination of the repeated calculations required in the discretization method and the multiple iterations within the optimization algorithm used for model-based strategy, the analysis of pulsed CEST is often much slower than its continuous counterpart. Hence, pulsed CEST is often treated as CW-CEST by finding the equivalent average field (AF) [123, 124] or power (AP) [32] of the pulse train to perform the analysis using the faster solution to the modified Bloch equations under continuous saturation.

Recently, studies have shown that the continuous approximation (both AF and AP) produces narrower off-resonance excitations when compared with pulsed saturation [32] and that the $MTR_{asym}$ is different for pulsed CEST and CW-CEST when the labile proton exchange rate is more than 50 $s^{-1}$ [31]. These raise the issue whether pulsed CEST can be analyzed via the equivalent CW-CEST or a discretization method must be used.

In this chapter, the differences in the z-spectra from a pulsed saturation and its equivalent continuous approximation (AF and AP) were examined using simulations to determine the validity of the latter for the analysis of a pulsed CEST experiment. Additionally, model-based quantitative analysis of pulsed CEST data from tissue-like phantoms using the continuous approximation and discretization method were compared. The quantified parameters such as water center frequency shift and amine proton exchange rate were

evaluated to determine the extent of the errors introduced by using the continuous approximation when analyzing the pulsed CEST data.

# 4.2 Materials and Methods

## 4.2.1 Numerical Simulation

#### *4.2.1.1 Comparison of Z-spectra*

All the simulated results were generated and processed using MATLAB (Mathworks, Natick, MA, USA). The modified Bloch equations for a 2-pool exchange model (water and amine protons labelled as pool w and cest, respectively) were used to simulate z-spectra, assuming $B_0$ = 4.7 T. The details of the coupled equations used are given in Appendix A1. A pulsed saturation scheme consisted of 50 Gaussian pulses with flip angle (FA) of 180 ° and 50 % duty cycle (DC) was considered, where each pulse cycle had a total duration of 40 ms, $T_{pd}$ (Gaussian pulse + inter-pulse delay). The saturation was performed from -3.8 to 3.8 ppm (-760 to 760 Hz at 4.7 T) with 0.19 ppm (38 Hz) increments. To model pulsed saturation, the discretization method was used with each Gaussian pulse discretized into 1024 segments. Crusher gradients with alternating signs, assumed to have been applied during the inter-pulse delays, were modelled by setting the transverse magnetization to zero at the end of the inter-pulse delay. The readout was performed after all the Gaussian pulses had been applied.

The equivalent AF and AP of the Gaussian pulses were calculated according to the following formulas [32]:

$$AF = 1/T_{pd} * \int_0^{T_{pd}} B_1 dt \,, \tag{23}$$

$$AP = \sqrt{(1/T_{pd} * \int_0^{T_{pd}} {B_1}^2 dt)} \ , \qquad (24)$$

where $T_{pd}$ is the pulse duration and $B_1$ is the RF power amplitude. The total saturation time was 2 s (50 pulses x 0.04s/pulse).

The remaining variables in the model were set according to published values: longitudinal relaxation times, $T_{1w}$ = 3 s, $T_{1cest}$ = 1 s; transverse relaxation times, $T_{2w}$ = 60 ms, $T_{2cest}$ = 8.5 ms [89]; amine proton exchange rate, $k_{cest}$ = 50 $s^{-1}$; amine proton concentration, $M_{cest0}$ = 0.33 M and water proton concentration, $M_{w0}$ = 100 M (equivalent to 0.0033 for the amine to water proton concentration ratio, $M_{cest0}/M_{w0}$).

#### *4.2.1.2 Minimum Discretization Required by the Discretization Method*

The computational time required to compute a z-spectrum using the discretization method is correlated with the number of segments used to generate a discrete approximation to the pulse shape. In order to aid the comparison of the discretized and continuous approximation for model fitting, the minimum number of segments, *N*, required for the former was investigated to minimize the processing time.

The pulsed CEST effect depends on the pulsed parameters used (FA, $T_{pd}$, DC and pulse shape). A range of pulsed parameter values was simulated: FA varied 60 ° to 300 ° with intervals of 60 °, $T_{pd}$ = 20, 40, 80, 100 and 200 ms, and DC changed from 0.3 to 0.8 with 0.1 increments. The rest of the parameters used were the same as above.

The Gaussian pulse was discretized into $2^n$ segments ($n$ = 1 to 10) and the 1024 segment result was used as the benchmark. RMS error between the spectra generated using the reduced number of segments and the benchmark was calculated; the smallest number of

segments which had a normalized RMS error smaller than 0.1 %, was chosen as *N* for that set of pulsed parameters.

## 4.2.2 *In Vitro*

### *4.2.2.1 Phantom Preparation*

Tissue-like phantoms were prepared according to Sun et al. [105] using creatine and agarose (Sigma Aldrich, St. Louis, MO, USA). Creatine was added to deionized water first to reach concentrations of 100 and 125 mM. Once the creatine had fully dissolved, agarose was added to form 3 % of the mixed solution and then heated to boiling. After that, the mixed solution was maintained at 50 °C and titrated to pH values of 5.5, 6 and 6.5 before being transferred to different 2 ml vials. A plastic container was used to house all the vials and filled up with agar to minimize field inhomogeneity. The phantoms were left to solidify at room temperature prior to the MRI experiment.

### *4.2.2.2 MRI Experiments and Data Processing*

All images were acquired using a 4.7 T Varian DirectDrive$^{TM}$ spectrometer (Agilent Technologies, Santa Clara, CA, USA) at room temperature. The $B_0$ was shimmed to minimize field inhomogeneity artifacts and the RF field was calibrated before experiments. The pulsed parameters used were identical to the simulation: 50 Gaussian pulses, FA = 180 °, $T_{pd}$ = 40 ms, DC = 50 % and saturation frequencies from -3.8 to 3.8 ppm (0.19 ppm increments). Crusher gradients with alternating signs were applied after each irradiation pulse to spoil the residual transverse magnetization. A single-slice spin echo EPI readout was used at the end of the saturation, with a FOV of 80 mm x 80 mm, matrix size of 64 x 64, slice thickness of 1 mm, bandwidth of 250 kHz, TE of 20 ms and TR of 4 s. An unsaturated scan with the same image properties was also acquired. The CEST data were collected in about 6 minutes.

Besides CEST imaging, relaxation time and magnetic field maps were obtained to account for the inhomogeneity in the scan. An inversion recovery sequence with eight inversion intervals from 100 to 6000 ms was used to measure the $T_1$ relaxation time of the water pool. Six separate spin echo images with TEs from 23 to 100 ms were measured to determine the $T_2$ relaxation time of the water pool. The $T_1$ and $T_2$ maps of the water pool were obtained by least-square fitting of the image intensities against the inversion intervals and TEs, respectively. WASSR was applied to find the main magnetic field inhomogeneity. The acquisition parameters were the same as for the CEST imaging, except that the FA was set to 61 °. A $B_0$ map was generated by first finding the saturation frequency that recorded the lowest magnetization, then seven saturation frequencies above and below the minimum point were interpolated to intervals of 0.0019 ppm (0.38 Hz). The water center frequency shift was determined using the Maximum Symmetry algorithm [74] based on the interpolated data. The saturation frequency at which the magnetization was minimum was used as the initial value for the search.

All the maps and *in vitro* CEST data were processed using nonlinear least-square curve fitting function, *lsqcurvefit* in MATLAB (Mathworks, Natick, MA, USA). A 3-pool model, which consisted of water (w), amine (cest) and MT, was used to fit to the collected data; the coupled equations are given in Appendix A2. A Gaussian lineshape function, which has been found to be more appropriate for tissue-like phantoms prepared using agarose, was used to model the MT effect [112].

Model-based analyses using the continuous approximation and discretization method were performed on the *in vitro* data. For the latter, it was discretized using the value of $N$ found in the simulation. There were 16 variables in the modified Bloch equations for a 3-pool

model: amplitude of the RF pulse ($\omega_1 = 2\pi B_1$, $B_1$ is determined by the FA but will vary in practice due to field inhomogeneity), longitudinal ($T_{1s}$) and transverse ($T_{2s}$) relaxations, proton concentrations ($M_{s0}$), exchange rates ($k_s$) and resonance frequency of the pools ($\omega_s$), where *s* refers to each of the pools w, cest and MT. However, the z-spectrum is not sensitive to some of these variables ($T_{1cest}$, $T_{2cest}$, $T_{1MT}$) and some can be determined relatively accurately prior to the CEST experiment ($T_{1w}$, $\omega_{cest}$, $\omega_{MT}$) or calculated from the equilibrium condition, for example, $C_w$. As a result, only nine variables ($T_{2w}$, $T_{2MT}$, $M_{w0}$, $M_{cest0}$, $M_{MT0}$, $k_{cest}$, $k_{MT}$, $\omega_w$ and $B_1$) were fitted. Field inhomogeneity was assumed to shift the water center frequency within ± 0.2 ppm and to affect the distribution of $B_1$ around ± 10 % of the applied FA. Since it is difficult to separate the effect of the amine proton exchange rate ($k_{cest}$) and concentration ($M_{cest0}$) (chapter 3) [114, 115], the latter was only allowed to vary within ± 5 % of literature values derived from similar phantoms [89, 117]. Although $T_{2w}$ and $M_{w0}$ could be determined using the multiple TE acquisition scheme and from the unsaturated data respectively, they were still treated as parameters to be fitted (within ± 20 % of the measured values). The search ranges of the properties of the MT pool ($T_{2MT}$, $M_{MT0}$ and $C_{MT}$) were set according to Zu et al. [32], who used the same phantoms. The remaining variables were assumed to be constant: $T_{1cest}$ = 1 s, $T_{2cest}$ = 8.5 ms, $T_{1MT}$ = 1 s, resonance frequency of amine protons, $\omega_{cest}$ = 1.9 ppm + $\omega_w$ [89], resonance frequency of MT pool, $\omega_{MT} = \omega_w$ [42] and $T_{1w}$ was determined using the inversion recovery sequence.

The sum of square residual and coefficient of determination, $R^2$, using discretized and continuous model fitting were calculated to assess the goodness of fit. The fitted $\omega_w$ using the model-based methods were compared with the WASSR results to study the discrepancies between them. Two-tailed t-tests were performed between the quantified $k_{cest}$ using the

different approaches to examine whether the estimated parameter values varied significantly. The CV (standard deviation divided by the mean) of the fitted $k_{cest}$ was also calculated to assess the performance of the different model fitting approaches.

# 4.3 Results

## 4.3.1 Numerical Simulation

The z-spectra generated using the discretization method and its continuous approximation (AF and AP) are shown in Figure 4.1. The AF approximation was a poor match to the pulsed spectrum; it underestimated the saturated magnetization across the simulated offsets. The z-spectrum generated using the AP approximation matched well to the spectrum produced by the discretization method, except at the frequency offsets near the water center frequency ($\omega_w$ - 0 ppm) and chemical shift of amine protons ($\omega_{cest}$ - 1.9 ppm), indicated by the green circles. Consequently, only the AP continuous approximation was used to perform the continuous model fitting for the phantom data.

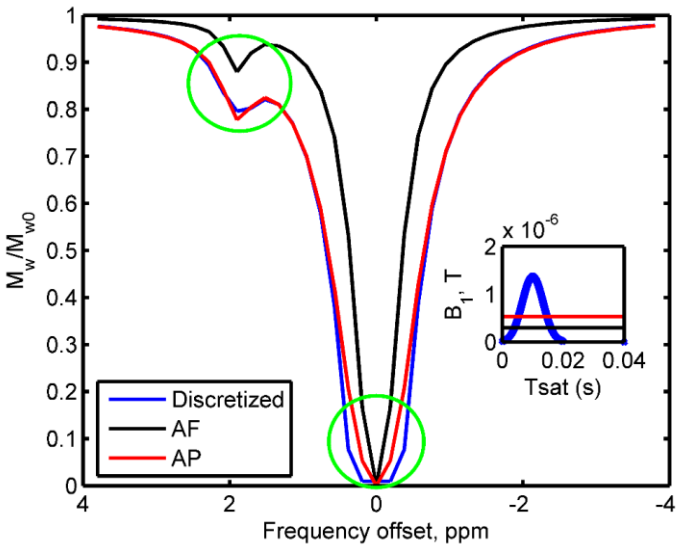


**Figure 4.1: Simulated z-spectra using continuous approximation (AF and AP) and discretization method. The green circles highlight the major differences between the different methods. The right inlet plot shows a single Gaussian pulse with its equivalent AF and AP.**

Figure 4.2 shows the values of *N* required for different pulsed parameters (FA, $T_{pd}$ and DC) to achieve a normalized RMS error that was less than the 0.1 % threshold. The smallest and largest number of segments needed within the investigated pulsed parameter ranges were 16 and 128, respectively. For the set of pulsed parameters used in the *in vitro* study, 32 segments per pulse were found to be sufficient.

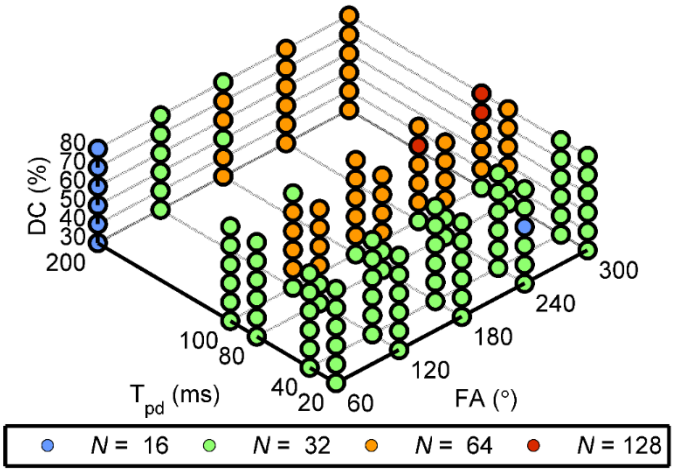


**Figure 4.2: The minimal number of discretization, *N*, required to achieve normalized RMS error to be less than 0.1% when compared with the benchmark (1024 segments) for different set of pulsed parameters. This four dimensional relationship (FA (*x*), $T_{pd}$ (*y*), DC (*z*) and *N* (color)) can be read by following the grid lines along each axis: there will always be 6 'balls' along the *z* direction which represent DC values from 30 to 80 %.**

## 4.3.2 *In Vitro*

The measured z-spectra corrected using the WASSR map for different creatine concentrations and pH values are shown in Figure 4.3a) and b), respectively. Figure 4.3c) shows the $MTR_{asym}$ of the phantoms after $B_0$ correction using the WASSR map and its corresponding means and standard deviations are presented in Figure 4.3d). When either creatine concentration or pH value increased, the dip of the amine pool and $MTR_{asym}$ became bigger. The largest $MTR_{asym}$ recorded was 16.7% for the 125 mM creatine phantoms with pH 6.5.

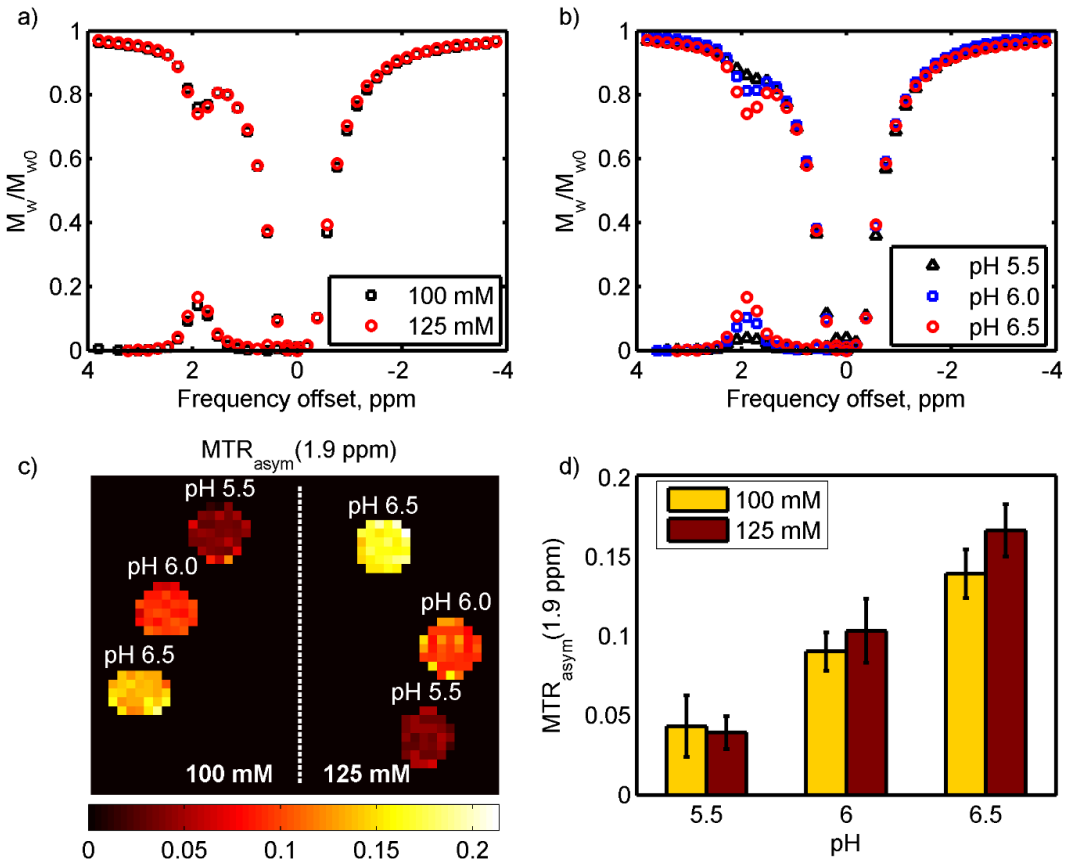


**Figure 4.3: (a) Measured z-spectra of different creatine concentration phantoms at pH 6.5. (b) Measured z-spectra of 125 mM creatine phantoms with different pH values. The asymmetry analysis spectra are plotted underneath the z-spectra in each plot. (c) MTR$_{asym}$ image at 1.9 ppm and (d) the means and standard deviations of MTR$_{asym}$(1.9 ppm).**

$R^2$ values calculated using $N$ sufficient to assure accuracy obtained from the simulation for the discretized model fitting on the phantom data are shown in Table 4.1. Excellent fits were found for all the measured CEST data ($R^2$ > 99). The fitted spectra using continuous and discretized model-based approaches for a 125 mM creatine phantom at pH 6 are shown in Figure 4.4a). The discretization method was able to fit the measured data with small residual errors at all the saturation frequencies. Similarly to the simulated data in Figure 4.1, the AP continuous method also fitted with small error, except near $\omega_w$. The fitted errors using the discretization method were substantially lower than its continuous (AP) counterparts for all the phantom data, as shown in the normalized sum of square error plot in Figure 4.4b).

**Table 4.1: Coefficient of determination, $R^2$ (mean ± standard deviation, %), for discretized model fitting.**

| Phantom | pH 5.5 | pH 6.0 | pH 6.5 |
|---|---|---|---|
| **100 mM** | 99.82 ± 0.2 | 99.93 ± 0.05 | 99.87 ± 0.07 |
| **125 mM** | 99.94 ± 0.05 | 99.92 ± 0.06 | 99.9 ±0.06 |

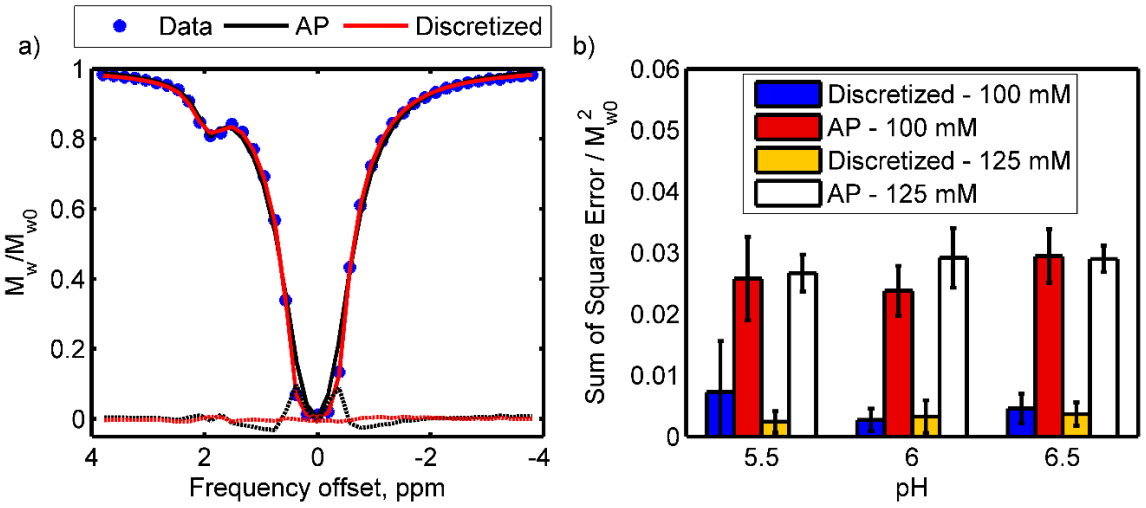


**Figure 4.4: (a) Measured data of phantom with 125 mM creatine concentration at pH 6 and continuous (AP) and discretized model fitted z-spectra. The residuals are plotted below the fitted spectra (dotted lines). (b) Normalized sum of square error plot of continuous (AP) and discretized model fitting for phantoms with different pH values and concentrations.**

Figure 4.5 shows the fitted values of water center frequency shift, $\omega_w$, obtained using the discretized and continuous model-based approaches. The results matched well to each other and also to the $B_0$ map generated using WASSR. The RMS errors and maximum difference between the model fitted $\omega_w$ and the WASSR map were about 1 and 2 Hz, respectively, for both methods.

Quantification of amine proton exchange rates, $k_{cest}$, using the continuous and discretized model-based approaches is shown in Figure 4.6. The difference in the CV of the fitted results ($CV_{AP} - CV_{discretized}$) are shown in Table 4.2, where positive values indicate the discretized fitted results had smaller variation than the continuous ones. All the CV differences were positive except the results for the phantom with 100 mM creatine concentration at pH 6; these indicated that the discretized model fitting was able to quantify

the parameter with higher precision. However, when two-tail t-tests were performed on the fitted results, no significant difference was found at a 5 % significance level, except for the 100 mM creatine concentration at pH 6 (Figure 4.6c).

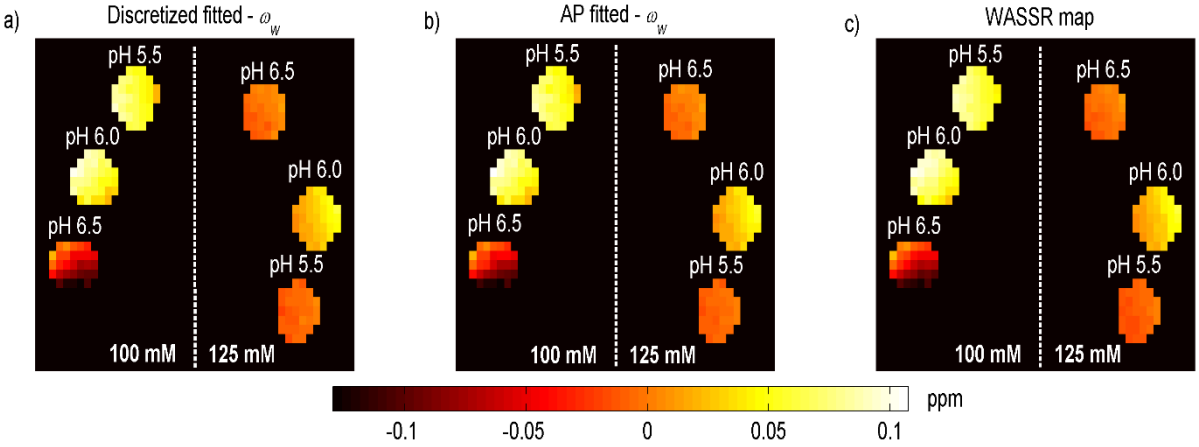


**Figure 4.5: Fitted values of water center frequency shift, $\omega_w$, using (a) discretized and (b) AP continuous model-based analysis, (c) is the $B_0$ map generated using WASSR.**

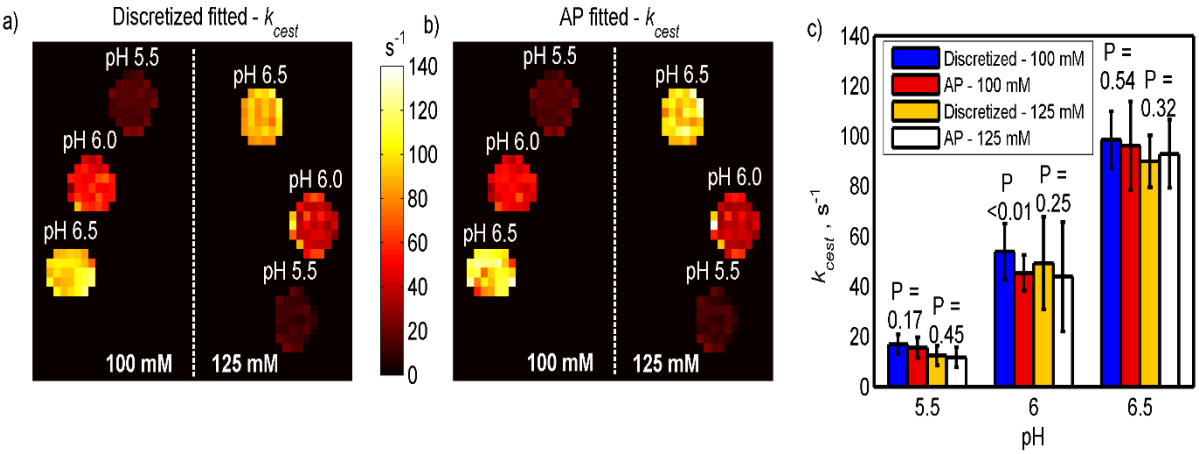


**Figure 4.6: Fitted values of amine proton exchange rate, $k_{cest}$, using (a) discretized and (b) AP continuous model-based analyses. The mean and standard deviation of fitted $k_{cest}$ using different methods are shown in (c). The P values displayed above the bars are the results of the two-tail t-tests (P < 0.05).**

**Table 4.2: Difference of coefficient of variation (CV) for the fitted amine proton exchange rate ($k_{cest}$) using discretized and continuous (AP) model-based analysis. * Positive values mean that discretized fitted results have smaller variation.**

| Phantom | $CV_{AP} - CV_{discretized}$ * | | |
|---|---|---|---|
| | **pH 5.5** | **pH 6.0** | **pH 6.5** |
| **100 mM** | 0.0305 | -0.0491 | 0.0690 |
| **125 mM** | 0.0290 | 0.1217 | 0.0321 |

## 4.4 Discussion

This study illustrates the differences in z-spectra obtained using continuous and pulsed saturation, and how these discrepancies can affect the quantified parameters such as $\omega_w$ and $k_{cest}$ using continuous and discretized model-based analysis. As suggested by Zu et al. [32], the differences are caused by the irradiation schemes used, where CW-CEST is able to saturate the protons more efficiently, leading to narrower off-resonance excitation around the frequency offset of water and amine protons, as shown in the simulated (Figure 4.1) and measured (Figure 4.4a) results.

It is apparent from Figure 4.4b) that the discretized model-based approach was able to fit better than its continuous (AP) counterpart but the smaller fitted errors of the former did not translate to significantly better quantification of $\omega_w$ and $k_{cest}$, as shown in Figure 4.5 and Figure 4.6. Although AF is not suitable for fitting the z-spectrum, the magnitude of its $MTR_{asym}$ may be approximately equal to the $MTR_{asym}$ calculated from AP for certain pulsed parameters and labile proton exchange rate. The quantified results of $\omega_w$ verify that model-based analysis can be used to determine the water centre frequency shift due to field inhomogeneity and that the additional WASSR scan is not necessarily required when the full z-spectrum is available.

When the two-tailed t-tests were performed for the estimated $k_{cest}$ for 100 mM creatine phantom at pH 6, the quantified parameter ($k_{cest}$) using different model-based approaches was found to be significantly different, as shown in Figure 4.6c). This may be caused by the strong correlation between each of the following factors: $T_{2w}$ [110], FA and $M_{cest}$, with $k_{cest}$. The influence of $T_{2w}$ and FA on $k_{cest}$ is significant because the resonance

frequency of the amine protons investigated is just 1.9 ppm away from the water resonance. $M_{cest}$ was estimated from the literature and derived from the equilibrium condition which makes the absolute quantification of each of them ($k_{cest}$ and $M_{cest}$) difficult. As suggested by Sun et al. [115], performing model fitting on data measured from multiple RF saturation powers may be one of the ways to achieve independent quantification of $k_{cest}$ and $M_{cest}$ because optimal RF power varies strongly with $k_{cest}$ but has minimal dependence on $M_{cest}$. However, this is not the scope of this study as only a single $B_1$ was used to perform the saturation. When model fitting was performed on the collected CEST data, all these parameters ($T_{2w}$, FA, $M_{cest0}$ and $k_{cest}$) were allowed to vary; the strong correlation between them might have contributed to the significantly different result in the quantification of $k_{cest}$ for 100 mM creatine phantom at pH 6.

Conventionally, the saturation frequencies of CEST are uniformly distributed across the investigated range. However, this kind of sampling schedule will contain samples that are minimally informative to the parameters of interest [125]. For example, $k_{cest}$ changes mainly affect saturation frequencies near the chemical shift of the exchangeable protons (Figure 4.3b). In chapter 3, an optimal sampling schedule (OSS) was introduced to maximize the information for the parameters of interest from the measured data. OSS selects the saturation frequencies based on the parameter sensitivity functions which describe how sensitive the data are to changes in the parameter values at a particular saturation frequency. When an OSS was optimized for $\omega_w$, $M_{cest0}$ and $k_{cest}$, the algorithm proposed a schedule that sampled repeatedly around the water center frequency and the chemical shift of the exchangeable protons with minimal or no samples at the other frequency offsets. By doing so, better SNR data are achievable, resulting in an improvement in the accuracy of the

important parameters estimated from the model fitting. The results of this study, namely those in Figure 4.1 and Figure 4.4a), indicate that the predominant differences between the pulsed and continuous z-spectra occur around the two resonances which coincide with the frequency offsets most sampled by the OSS. This might imply that quantitative analysis of data acquired using pulsed CEST with an OSS strategy may not be feasible with the continuous approximation and in this case the discretization method may have to be used.

In practical data analysis scenarios, the results in Figure 4.2 indicate that the number of discretized segments required by the discretization method varies according to the pulsed parameters used and could be reduced from the benchmark (1024 segments) to minimize the computational cost. Previously, analysis has been performed by discretizing each pulse into 64 [31] or 512 [110] segments. The computation time required to calculate a spectrum using 512 segments per pulse was roughly 16 times (9.8 min/0.629 min) longer than 32 segments per pulse used in this study and 4 (9.8 min/2.483 min) times longer than the largest discretization needed for the range of pulsed parameters simulated. The computational time reduction above was recorded from an Intel Xeon CPU E5520 @ 2.27 GHz with 8G of RAM. When discretized model fitting, which requires iterative calculation of the magnetization, is applied, using a smaller number of discretized segments is important as it will result in a substantial reduction in computational cost. Despite the reductions in computational costs afforded by the reductions in the number of discretization required in practice, analysis of pulsed CEST data using a discretized pulse train is still high compared to the continuous equivalent (a few seconds to calculate a spectrum per iteration).

APT imaging relies on the exchange of protons between the endogenous amide mobile proteins in the composite backbone with the bulk water to produce contrast at the cellular

protein level. The APT effect observed *in vivo* is small due to the low concentration of the proteins and the endogenous amide protons involved in the chemical exchange have slow exchange rates, 28 $s^{-1}$ [22]. When an evenly distributed sampling schedule and a pulsed irradiation scheme are used in the APT imaging, the results of tissue-like phantoms with pH 5.5 in Figure 4.5 and Figure 4.6 suggest that AP continuous model-based approach can be applied in place of the computationally expensive discretization method in the quantitative study, assuming that the differences in the resonance frequency and magnetic properties of amine and amide protons have negligible effect.

In order to broaden the applicability of this study to a wider range of acquisition strategies and parameter values, additional simulations were performed by comparing the sum of square and $MTR_{asym}$ difference of the simulated z-spectra generated by AP and the discretization method, taking the results from the phantom study as the benchmark. Any other set of pulsed parameters which produced a sum of square and $MTR_{asym}$ difference smaller than the benchmark should also be able to produce the same quantitative fitting results – no significant difference between the quantified parameters using either approaches. The pulsed and model parameter values used to generate the results in Figure 4.2 were investigated, except $k_{cest}$ was set to be 28 $s^{-1}$ which was the amide proton exchange rate found in APT imaging. The result is presented in Figure 4.7, where white circles refer to the sets of pulsed parameters which had a smaller sum of square and $MTR_{asym}$ difference than the benchmark and black circles represent the opposite. Since the investigated differences were smaller than the benchmark, these sets of pulsed parameters should also be able to generate equivalent quantitative fitting results for the important model parameters when the AP continuous approximation is used.

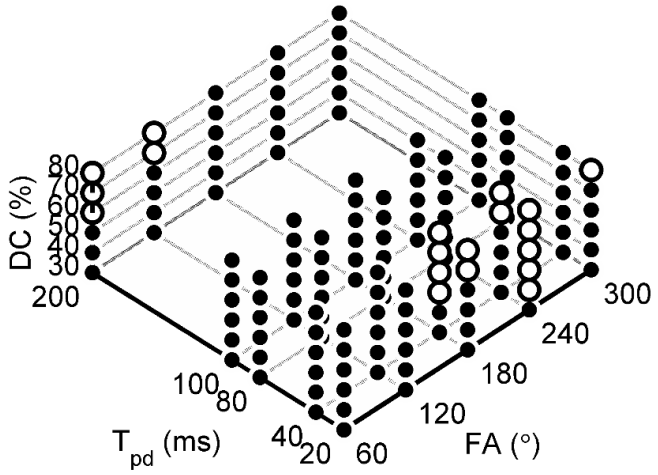


**Figure 4.7: The other sets of pulsed parameters which should produce equivalent quantitative fitting results (white circles) for the important model parameters investigated when AP approximation is used. Black circles represent the sets of pulsed parameters that had a sum of square and $MTR_{asym}$ difference bigger than the benchmark (the one used in the phantom study).**

However, using AP continuous approximation to replace the discretization method may not be translated to a pulsed CEST experiment that involves labile protons with high exchange rate such as PARACEST agents because $MTR_{asym}$ has been observed to be different between CW-CEST and pulsed CEST when $k_{cest}$ is higher than 50 $s^{-1}$ and when the exchange rate increases further, the difference becomes larger [31]. For the pulsed CEST study in this higher exchange regime, the discretization method may need to be applied for more accurate data fitting and model-based quantitative analysis.

There are multiple effects or metabolites such as amide, NOE, fat and MT that can affect the *in vivo* CEST experiment. In order to separate these confounding effects or metabolites and to model the z-spectrum accurately for quantitative model-based analysis, each of them should be treated as a separate pool. A 3-pool model which consists of water, the labile protons of interest and MT may be the minimum required to model the *in vivo* environment. However, the z-spectra acquired at 7T reveal a broad group of resonances between 0 to 5 ppm, and appreciable saturation effects observed between 0 to -5 ppm [104].

Thus, it is possible that a 3-pool exchange model would be insufficient to perform the quantitative model-based analysis on a full z-spectrum. Having multiple pools in the model-based analysis is a challenging task even when the AP continuous approximation is used because the computational cost of calculating the matrix exponential in the analytical solution (Eqn.(8)) increases exponentially with the number of pools. Furthermore, increasing the number of pools in the analysis requires more parameters to be fitted from the data, leading to a higher risk of over-fitting and thus inaccurate results. The OSS discussed above may be one possible solution, since by selectively saturating certain frequency offsets, the contaminations from other labile pools can be avoided. Other simplified analytical approximations to the model solutions such as the relationship in [126] could also be considered, assuming that the inaccuracies introduced by the simplification can be acceptably accounted for. It is believed that the applicability of this study (use of AP approximation in place of discretization method to analyse a pulsed CEST experiment) will still hold if the *in vivo* environment can be modelled accurately for slowly exchanging protons.

## 4.5 Summary

Studies on tissue-like phantoms with slow exchange protons saturated by a series of short Gaussian pulses show no significant difference for the important fitted model parameters such as water center frequency shift and amine proton exchange rate when quantitative model-based analysis using either average power approximation or discretization method is used. This suggests that when APT imaging is performed using a pulsed saturation with certain pulsed parameters, the fast continuous approximation (average power) to the time dependent RF irradiation pulses can replace the computationally expensive discretization approach for quantitative model-based analysis.

# Chapter 5

# Comparing Different Methods of Quantifying MRI APT Effect in Hyper-acute Stroke Patients [‡]

[‡] Parts of this chapter have been published in NMR in Biomedicine with open access, no permission is required to reproduce the content:
Y.K. Tee, G.WJ. Harston, N.P. Blockley et al., Comparing Different Analysis Methods for Quantifying the MRI Amide Proton Transfer (APT) Effect in Hyperacute Stroke Patients, NMR in Biomedicine, in press.

# 5.1 Introduction

In a healthy brain, when the metabolic rate of tissue increases, the associated increase of glucose and oxygen demands are met by an increase in perfusion. When ischemic stroke happens, the blood flow is impeded and an imbalance arises due to low or no metabolic supply, leading to hypoxia and finally cerebral infarction as a result of prolonged ischemia [6-8]. Consequently, intra-venous thrombolysis or mechanical thrombectomy is performed, if clinically feasible, to restore the blood flow to salvage as much tissue as possible.

The identification of tissue in the penumbra, i.e. tissue that can be salvaged if re-perfused, via the imaging of pH has been suggested recently because the accumulation of lactate from anaerobic glycolysis in the absence of oxygen supply causes the pH to drop [52]. Based on the metabolic change proposed by Hossmann (Figure 1.1), lactacidosis happens prior to cerebral infarction; thus by assessing the metabolic state of the tissue, more specifically pH changes, it is hypothesized that pH imaging may potentially offer a prediction of ischemic injury.

APT imaging using the CEST mechanism is capable of inferring intracellular pH through the transfer of protons from the amide group in the backbone of proteins and/or peptides to water. This process is base-catalysed in the physiological pH range (6.5 to 7.5) and hence pH-dependent [22]. The determination of intracellular pH through APT imaging has been demonstrated in animal models [22, 91]. Sun et al. [50] showed that the quantified APT effect in animal models was highly correlated with the final infarct tissue area defined using $T_2$ hyper-intensity at 24 hours, suggesting that thresholds may exist to define tissue outcome following ischemic stroke. It is generally agreed that the APT effect becomes smaller in the

infarcted and salvageable tissue during the hyper-acute period, owing to pH reduction as a result of the accumulation of lactate.

The first application of APT imaging in stroke patients was reported by Zhao et al. [53]. However, the reported cases had a mean onset time of 4.3 days which is far beyond the therapeutic window (< 6 hours) and thus the initial assumption (decrease of APT effect being mainly due to pH reduction) may not hold because secondary phenomena after stroke, such as vasogenic oedema formation, can lead to changes in the water relaxation time and concentration, undermining the quantified effect. In addition, there may be a change in the amide proton concentration due to cell depolarisation and loss of cytoplasm which would also modulate the APT signal.

Despite the potential of APT imaging to measure pH, most of the literature so far has focused on generating pH-weighted contrast rather than quantitative pH maps. The most commonly used metric to measure pH-weighted saturation transfer image is $MTR_{asym}$ but this metric is dependent on experimental parameters [100] and contaminated by various other transfer of magnetization effects [21, 28, 29]. Furthermore, NOE has recently been shown to be pH sensitive under low power saturation [113], making the use of signal measured at -3.5 ppm less suitable as a reference for APT quantification.

In this chapter, a recently introduced quantitative Bayesian model-based analysis [44] and conventional approaches such as $MTR_{asym}$ were thus studied to evaluate their sensitivity to the APT data acquired from healthy subjects and hyper-acute stroke patients imaged within and approximately 6 hours of ischemic onset. Statistical evaluations were performed between the infarct core and contralateral normal appearing tissue calculated using the different approaches to study their efficacies for clinical stroke imaging.

# 5.2 Theory

## 5.2.1 Asymmetry Analysis

In an APT imaging experiment, saturation is usually performed across a range of frequency offsets. The APT effect is often calculated, following the practice in MT imaging, using $MTR_{asym}$ (Eqn. (14)):

$$MTR_{asym} = \frac{M(-\Delta\omega) - M(\Delta\omega)}{M_0}.$$

This analysis inherently assumes that all the non-APT effects such as spillover and MT effects are symmetric about the water centre frequency; thus, the pure APT effect can be obtained by taking the difference between the signals measured at positive and negative offsets.

Various other forms of asymmetry measures, based on the concept of Eqn.(14), have been studied using phantoms, PARACEST agents and animal models, and it has been found that a complementary approach denoted as $ST^{com}$, where ST stands for saturation transfer, is more suitable for *in vivo* applications [101]. For consistency in this work, $ST^{com}$ is renamed as $MTR_{asym_comp}$, and can be calculated using Eqn. (15):

$$MTR_{asym_comp} = \frac{M(-\Delta\omega) - M(\Delta\omega)}{M_0 - M(-\Delta\omega)}.$$

Recent studies have shown that the symmetric assumption does not hold, especially *in vivo*, due to inherent asymmetries in the MT or contributions from the NOE [21, 29, 88, 113]. Hence, quantifying the APT effect using $MTR_{asym}$ contains not only the APT effect (APTR), but also contributions from other transfer of magnetization effects, $MTR'_{asym}$ (Eqn. (20)):

$$MTR_{asym} = MTR'_{asym} + APTR\ .$$

As a result of the contributions from $MTR'_{asym}$, quantification of the APT effect using the above metric often results in negative amplitude when a low saturation power (around 0.5 μT) is used, which would not be expected from a symmetric z spectrum [44, 104]; thus, these metrics are usually regarded as producing APT- or pH-weighted images. Although the complementary approach is claimed to perform better than the conventional metric in a biological environment, it still suffers from the same confounding factors in the negative frequency offsets.

## 5.2.2 Model-based Analysis

In order to quantify the pure APT effect, a model-based approach has been proposed [44, 106, 110, 125], where the full modified Bloch equations in section 2.2.3 are fitted to the measured data, including pools for water, amide and MT asymmetric effects. Using the fitted parameters from the model-based analysis, a further quantitative metric can be calculated, denoted as APTR*. This measure uses the parameters obtained from model-fitting to generate an ideal 2-pool (water + amide) model and to compare it to an ideal 1-pool model of water, where both the ideal 1- and 2-pool model are simulated using the fitted parameters within the multi-pool fit, to obtain the pure APT effect (Eqn. (19)) [44, 125]:

$$APTR^* = \frac{M_{1-pool}(\Delta\omega) - M_{2-pool}(\Delta\omega)}{M_0}.$$

Although a greater number of pools can be used to perform the model fitting as required and thus correct for asymmetries in the z-spectrum, only the fitted model parameters of water and the amide pool are used to calculate APTR*. In principle, APTR* provides a single quantitative measure of the APT effect (combining both amide proton exchange rate and

concentration contributions) without $B_0$ inhomogeneity, spillover, MT and NOE influences, since the latter effects (MT and NOE) can be accounted for by grouping them as a separate pool in the model-fitting [44, 122].

# 5.3 Materials and Methods

## 5.3.1 Subject Recruitment

Six patients (76.8 ± 18 years) presenting with hyper-acute stroke symptoms with mean onset time of 3 hours 44 minutes were recruited and scanned following informed consent or agreement from a representative according to a research protocol agreed by the UK National Research Ethics Service committee (ref: 12/SC/0292). Thrombolysis was given to three of the patients prior to or during the MRI scans. All the patients had a follow-up scan on day 7 after the ischemic onset. The details of the patient recruitment are listed in Table 5.1. Two healthy volunteers (28 and 36 years) were also scanned to act as the control.

**Table 5.1: Summary of details and clinical symptoms of the patients recruited in this study, where TACS stands for total anterior circulation stroke.**

| No. | Age | Sex | Image time after ischemic onset (hr:min) | Stroke location | Symptoms/Types | Thrombolysis |
|---|---|---|---|---|---|---|
| 1 | 92 | M | 2:50 | L | TACS | Yes |
| 2 | 86 | F | 3:09 | L | TACS | No |
| 3 | 80 | F | 5:46 | L | TACS | No |
| 4 | 94 | M | 6:10 | L | Dysphasia and mild right sided weakness | Yes |
| 5 | 52 | F | 2:48 | L | TACS | Yes |
| 6 | 57 | M | 1:43 | R | Isolated left weakness and sensory loss | No |

## 5.3.2 MRI Experiment

All the patient MRI scans were performed using a 3T Siemens Verio scanner in the Oxford Acute Vascular Imaging Centre located at the John Radcliffe Hospital, UK. The total scan time was limited to 25 minutes/session.

The following MRI sequences were applied to each patient unless stated otherwise: $T_1$ structural image with pixel dimension = 1.8 x 1.8 x 1.0 $mm^3$, FOV = 228 mm, TR = 2040 ms and TE = 4.55 ms; DWI with 3 directions, spatial dimension = 1.8 x 1.8 x 2.0 $mm^3$, FOV = 240 mm, 4 averages, b = 0 and 1000 $s/mm^2$, TR = 9000 ms and TE = 98 ms; multi-post labelling delay vessel-encoded pseudo-continuous arterial spin labelling PWI [127] with pixel dimension = 3.4 x 3.4 x 4.5 $mm^3$, FOV = 220 mm, TR = 4080 ms and TE = 14 ms; and single slice APT imaging with pixel dimension = 3.4 x 3.4 x 5.0 $mm^3$, where the plane was selected by an experienced clinician based on the lesion seen on the DWI scan. The APT saturation was performed with 50 Gaussian pulses with flip angle = 184° and duration of 20 ms with 20 ms spacing each, to achieve an equivalent continuous saturation $B_1$ value of 0.55 μT (average power). Crusher gradients were applied between pulses to spoil the residual transverse magnetization. A spin-echo EPI readout (TR = 5s, TE = 23 ms, matrix 64 x 64 and 6/8 partial Fourier) was performed after all the Gaussian pulses had been applied. Data were acquired for a range of saturation frequency offsets from -4.5 to 4.5 ppm using a semi-OSS, with more sampling points placed at and around the resonance frequency of amide protons [125], and at ± 300 ppm (treated as unsaturated images). The semi-OSS acquired offsets from -4.1 to -2.9 ppm and from -0.9 to 0.9 ppm, both with 0.3 ppm intervals and at -50, -30, 2.9, 3.1, 3.2, 3.3, 3.4, 3.4, 3.5, 3.5, 3.6, 3.6, 3.7, 3.8, 3.9, 4.1, 30 and 50 ppm. Water excitation using 1-2-1 binomial pulses was applied to suppress the fat signal prior to EPI readout.

The same MRI scanning protocols were applied in the follow-up scan, except that the APT imaging was replaced by fluid-attenuated inversion recovery (FLAIR) with pixel dimension = 1.9 x 1.9 x 2.0 mm, FOV = 240 mm, TR = 9000 ms and TE = 96 ms to define the infarction. For the healthy subjects, only the $T_1$ structural and APT scans were acquired, and there was no follow-up scan.

### 5.3.3 Data Processing and Analysis

The brain extraction tool (BET) in the FSL package [128] was used to remove the skull and non-brain areas in all the collected data. For the DWI and PWI data, the default settings were used. When extracting the brain from the $T_1$ and FLAIR images, the bias field correction option was selected. Since the FOV of the APT image in the z-direction was small, the brain in APT images was extracted by padding the end slices in both directions, copying the end slices several times, running the tool and then removing the added slices (option Z in BET).

Quantitative cerebral blood flow maps were derived for each brain-feeding artery separately using the vessel-encoded perfusion data, as described previously [127], before combining them to give a map of the total blood flow in each voxel.

All the imaging modalities were transferred to the $T_1$ space using FMRIB's Linear Image Registration Tool (FLIRT) in the FSL package [129]. Rigid body registration with six degrees of freedom and correlation ratio cost function were applied to register each imaging modality to $T_1$, except for the single slice APT data.

For the APT data, the different frequency offset brain images were first registered to the unsaturated APT brain image using 2D rigid body registration with three degrees of freedom. Subsequently, a 3-pool model consisting of water (w), amide (APT) and

magnetization transfer + nuclear Overhauser effect (MT+NOE) following [44] was fitted pixelwise to the motion-corrected z-spectrum using a Bayesian algorithm [130] (www.fmrib.ox.ac.uk/fsl/baycest) with the prior values of each parameter given in Table 5.2 and treating the pulsed saturation as its continuous approximation using AP [106].

**Table 5.2: Model parameters with prior values expressed as mean and standard deviation (SD) of a normal distribution, modified from [44].**

| | ***Water Pool*** | | ***APT Pool*** | | ***MT + NOE Pool*** | |
|---|---|---|---|---|---|---|
| ***Parameter*** [A] | **Mean** | **SD** | **Mean** | **SD** | **Mean** | **SD** |
| $M_0$ | 0 | $10^6$ | - | - | - | - |
| $M_{APT0,\ (MT+NOE)0}$ / $M_{w0}$ | - | - | 0.09/112[B] | 0.02/112[B] | 0 | 0.01 |
| $k_{APT,\ (MT+NOE)}$, (Hz) | - | - | 20 | - | 30 | - |
| $log(k_{APT,\ (MT+NOE)})$ | - | - | 3.0 | 1.0 | 3.4 | 1.0 |
| $T_1$, (s) | 1.3 | 0.15 | 0.77 | 0.15 | 1.0 | 0.15 |
| $T_2$, (ms) | 70 | 14 | 10 | 2 | 0.2 | 0.04 |
| $\omega$, (ppm) | 0 | 0.1 | 3.5 | 0.1 | -2.41 | 0.1 |

A. Glossary: $M_{i0}$ – initial magnetization; $k_i$ – exchange rate; $T_{1i}$ – longitudinal relaxation time; $T_{2i}$ – transverse relaxation time; $\omega_i$ – chemical shift of each pool with respect to water; *i* refers to water, APT or (MT+NOE) pool.

B. The mean and standard deviation of *in vivo* amide concentration were set to include the reported values in the literature: 72 mM [22] and 100 ± 8 mM [88], where 112 M is the concentration of water protons.

The shift of the z-spectrum due to $B_0$ inhomogeneity was corrected pixelwise using the fitted water centre frequency from the model fitting. $MTR_{asym}$ was obtained by finding the area under the curve from 3.3 to 3.7 ppm according to Eqn. (14) using the shift-corrected z-spectrum at each pixel, likewise $MTR_{asym_comp}$ which was calculated following Eqn. (15), where $M_0$ became the unsaturated signal multiplied by the frequency range considered (3.7 – 3.3 = 0.4 ppm).

Previously, a relationship between the based-catalysed amide proton exchange rate and intracellular pH has been calibrated using phosphorus and WEX spectroscopy [22]:

$$pH = 6.4 + \log_{10}\left(\frac{k_{APT}}{5.57}\right). \quad (25)$$

For the proposed model-based approach, an idealised APTR* versus pH relationship could also be formed using the relationship above and simulations. By assuming water and amide proton concentrations equal to 112M and 100mM [88], respectively, and the remaining parameters in the 2-pool exchange model (water and APT) to have the mean values in Table 5.2, saturated by $B_1$ = 0.55 μT and saturation time = 2 s (to match the experiment), a range of idealised APTR* versus different pH values (calculated from Eqn. (25) by varying amide proton exchange rates) could be simulated and a relationship between them could be formed.

For the collected APT data, the idealised APTR* could be calculated according to Eqn. (19) using only three parameters from the model fitting: 1) fitted unsaturated signal, $M_{w0}$; 2) fitted amide proton exchange rate, $k_{APT}$; and 3) fitted amide proton signal, $M_{APT0}$. Since the variations of the remaining parameters in the ideal 1- and 2-pool exchange model should have been accounted for by the fitting algorithm, they were assumed to have the values from the simulations used to generate the idealised APTR* vs pH relationship. Both $k_{APT}$ and $M_{APT0}$ were used to calculate the idealised APTR* instead of just the $k_{APT}$, which is related to pH, because both these parameters will affect the z-spectrum at the amide resonance and it has been proved difficult to separate their effects in model fitting using single saturation power (chapter 3) [44, 125]. The $M_{w0}$ was also included to normalize the measured signal. The idealised APTR* will be simply referred to as APTR* hereafter.

The quantified APT effects using the different metrics ($MTR_{asym}$, $MTR_{asym_comp}$ and APTR*) were transformed to the $T_1$ image space using FLIRT by first registering the unsaturated APT brain image to the corresponding $T_1$ slice utilising a rigid body registration

with three degrees of freedom to obtain the transformation matrix. The calculated maps were then transformed to the $T_1$ space by applying the saved transformation matrix so that all the different imaging modalities could be assessed in a common space.

The $T_1$ structural data were segmented using FMRIB's Automated Segmentation Tool (FAST) [131] into cerebrospinal fluid (CSF), grey and white matter (GM & WM) using a 0.1 Markov random field beta value for the main segmentation phase and bias field smoothing. The generated partial volume estimates were used to minimize the contamination of the non-brain area in the statistical evaluations below.

### 5.3.4 Healthy Subjects

The healthy subjects were recruited to act as the control because under normal physiological conditions, both intra- and extracellular pH are tightly regulated by the body buffering system and cellular ion transporters. As a result, the APT signal across different compartments of the brain should be relatively homogeneous, reflecting the assumption that APT provides a direct measure of pH. Two criteria were used to assess the efficacy of the different quantification methods in the healthy controls: 1) contrast between GM and WM in the brain, C = $(M_{GM} - M_{WM})/(M_{GM} + M_{WM})$, where $M$ is the average signal of the studied metrics in a region of interest (ROI); and 2) CV, defined as the ratio of the standard deviation to the mean of the respective quantification method, in both GM and WM to study its precision. The most suitable APT quantification method for a healthy brain should produce the smallest CV in the GM and WM, and have minimum contrast between these ROIs. In order to minimize partial volume effects and contamination from non-brain areas such as CSF, the GM and WM masks were created using an 80 % threshold on the GM and WM partial volume estimates generated by FAST.

### 5.3.5 Stroke Patients

The average z-spectra within a ROI in the ischemic area, indicated by hyper-intensity in the admitted DWI data (b = 1000), and the contralateral normal appearing tissue were plotted to study their differences. The coefficient of determination, $R^2$, was calculated to assess the goodness of fits for the model-based analysis in each ROI.

The infarct core mask of each patient was determined by finding an overlapping area between hyper-intensity in the DWI data (b = 1000) acquired during admission and hyper-intensity in the FLAIR images collected during follow-up scans. By transforming the masks drawn on different imaging modalities to the hyper-acute $T_1$ data space using FLIRT, two-tailed unpaired t-tests were performed on the quantified hyper-acute APT effect using the different approaches between the infarct core and contralateral normal appearing tissue, to examine which metric was more suitable to differentiate them.

The t-tests were performed twice for $MTR_{asym}$ and $MTR_{asym_comp}$; once directly on the calculated values and the other within a specified range: $MTR_{asym} < 0$; $-1.5 < MTR_{asym_comp} < 0$. This was done to minimize the influence of measurement noise and artefacts such as imperfect fat suppression. In order to minimize the contamination from CSF to the tissue APT signal, the statistical tests were only performed on the tissue mask created below the 20 % threshold on the CSF partial volume estimates generated by FAST.

For the hyper-acute APT effect quantified using the different approaches, the contrast between the infarct core and the contralateral normal appearing tissue, and the CV in the contralateral tissue of each respective measure were both calculated. The most suitable APT quantification method for the patient data should produce the highest contrast between the

infarct core, C, and the contralateral normal appearing tissue, and yet have the smallest CV (variation) in the contralateral tissue, $CV_{Contralateral}$. Thus, the contrast-to-noise ratio (CNR), defined as CNR = $C/CV_{Contralateral}$, was calculated to assess which APT quantification method was most suitable for clinical stroke imaging.

## 5.4 Results

The representative z-spectra and model-based fits in the ischemic area (hyper-intensity on the admitted DWI data) and the contralateral normal appearing tissue of patients 3 and 4 are plotted in Figure 5.1. From the measured data, the z-spectra in the ischemic area were found to have higher magnitude of magnetization ratio (smaller saturation effect) at the chemical shift of amide protons, as well as at the negative frequency offsets (aliphatic range) when compared to the contralateral ROI. Very good fits were obtained using the 3-pool model, where $R^2$ ≥ 98.6% in the ischemic and contralateral ROIs. The main discrepancy between the fits and measured data was found to be around the water centre frequency.

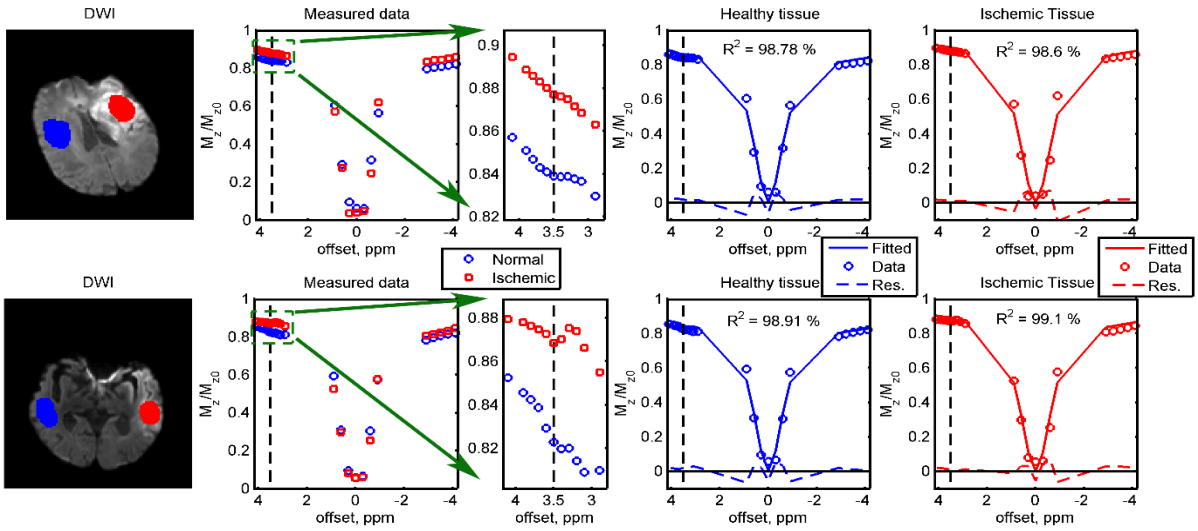


**Figure 5.1: Measured z-spectra after $B_0$ correction and model fits in the different ROIs of patient 3 (top row) and 4 (bottom row), where the red area indicates the ischemic tissue (hyper-intensity on DWI data (b = 1000) acquired during admission) and the blue region refers to the contralateral normal appearing tissue. Very good fits were obtained in the ROIs with the coefficient of determinant, $R^2$ ≥ 98.6 %. The vertical black dashed lines represent the chemical shift of amide protons and the blue/red dashed lines underneath the fits and measured data are the residual.**

The quantified APT effects in the healthy volunteers using the different metrics are shown in Figure 5.2. There were some intra- and inter-subject variations in the quantified APT effect using the different methods in the GM and WM, but no obvious low signal areas were observed. The mean, standard deviation and CV of GM and WM along with the contrast from each metric are presented in the bottom row of Figure 5.2. The APT effect was found to be negative when asymmetry measures ($MTR_{asym}$ and $MTR_{asym_comp}$) were used, with the APT effect in the WM more negative than in the GM. When the APT effect was quantified using APTR*, positive differences were obtained; WM had consistently smaller APTR* magnitude than the GM. APTR* was found to have the smallest CV in the GM and WM (≤ 13.81 %), and also the smallest contrast between these tissue areas ($C_{avg}$ = 3.48 %). $MTR_{asym}$ had the highest contrast between GM and WM but a smaller CV than $MTR_{asym_comp}$ in each region.

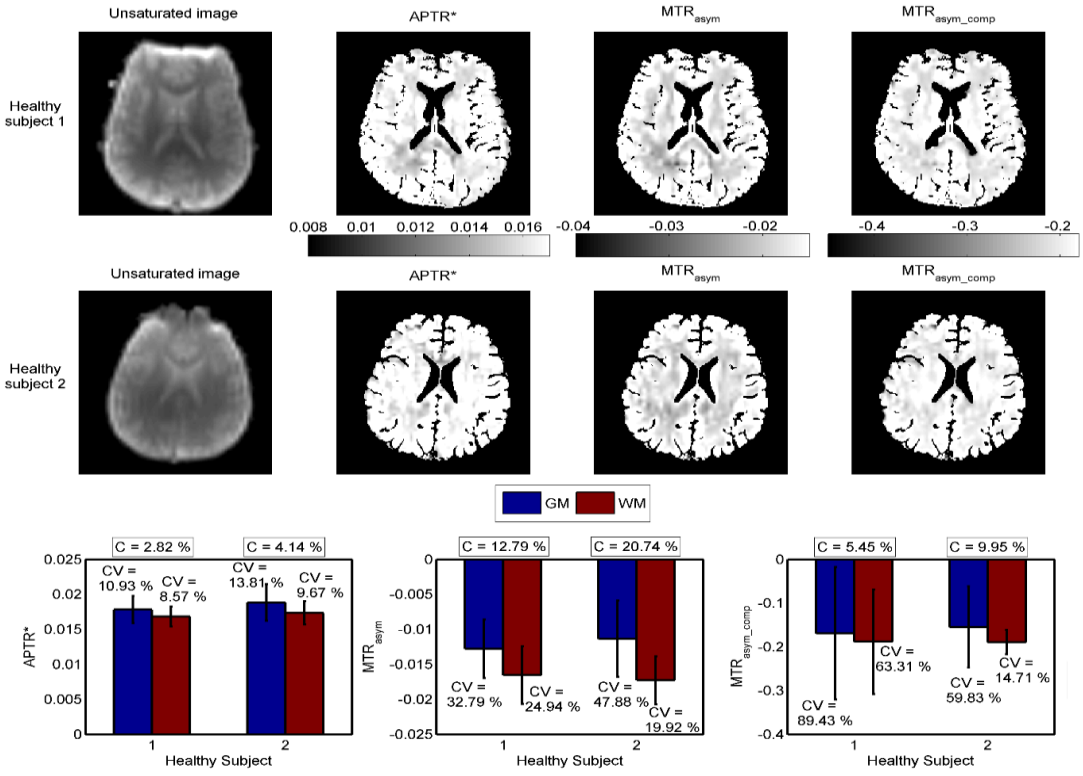


**Figure 5.2: APT unsaturated images and calculated maps of APTR*, $MTR_{asym}$ and $MTR_{asym_comp}$ of healthy volunteers. Tissue masks generated from FAST have been used to mask out the non-tissue areas such as CSF; thus, the scale bar does not reflect the quantified APT effect in these areas. The bar graphs and error bars are the means and standard deviations, respectively, of each metric in the GM and WM. CV stands for coefficient of variation and C refers to the contrast between the GM and WM.**

Figure 5.3 shows the calculated APT effect using $MTR_{asym}$, $MTR_{asym_comp}$ and APTR* for patient 3, along with the different imaging modalities collected on admission and the follow-up FLAIR image in the APT plane. A large hypo-perfused area was observed in the left hemisphere during the initial scan. APTR* and $MTR_{asym_comp}$ showed a low signal area in the ischemic region based on the hyper-intensity area in the DWI image (b = 1000) but smaller than the hypo-perfused region. For $MTR_{asym}$, the difference between ischemic and healthy tissue was less obvious when compared to the other two metrics. In the day 7 follow-up FLAIR scan, the infarction became congruent with the initial hypo-perfused area.

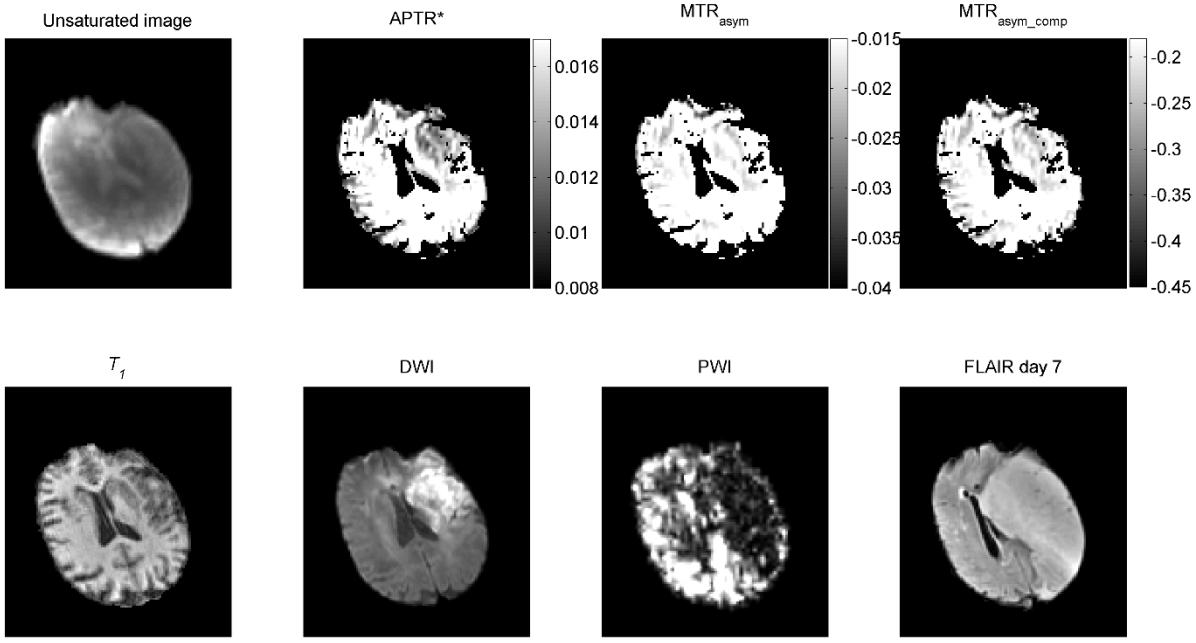


**Figure 5.3: Patient 3 data (APT, $T_1$, DWI (b = 1000) and PWI) and the processed APT results (APTR*, $MTR_{asym}$ and $MTR_{asym_comp}$) on admission, and follow-up FLAIR image on day 7. Tissue masks generated from FAST have been used to mask out the non-tissue areas such as CSF; thus, the scale bar does not reflect the quantified APT effect in these areas.**

Results from a further patient are shown in Figure 5.4. It was observed that $MTR_{asym}$, $MTR_{asym_comp}$ and APTR* all showed a low signal region that was larger than the ischemic tissue based on the hyper-intensity area on the DWI data. PWI data were not acquired in this subject on admission due to technical and time constraints. The hyper-intensity area on the FLAIR image acquired during the day 7 follow-up scan was approximately the size of or slightly larger

than the initial hyper-intensity area on the DWI image but not as big as the low signal region presented by $MTR_{asym}$, $MTR_{asym_comp}$ and APTR*.

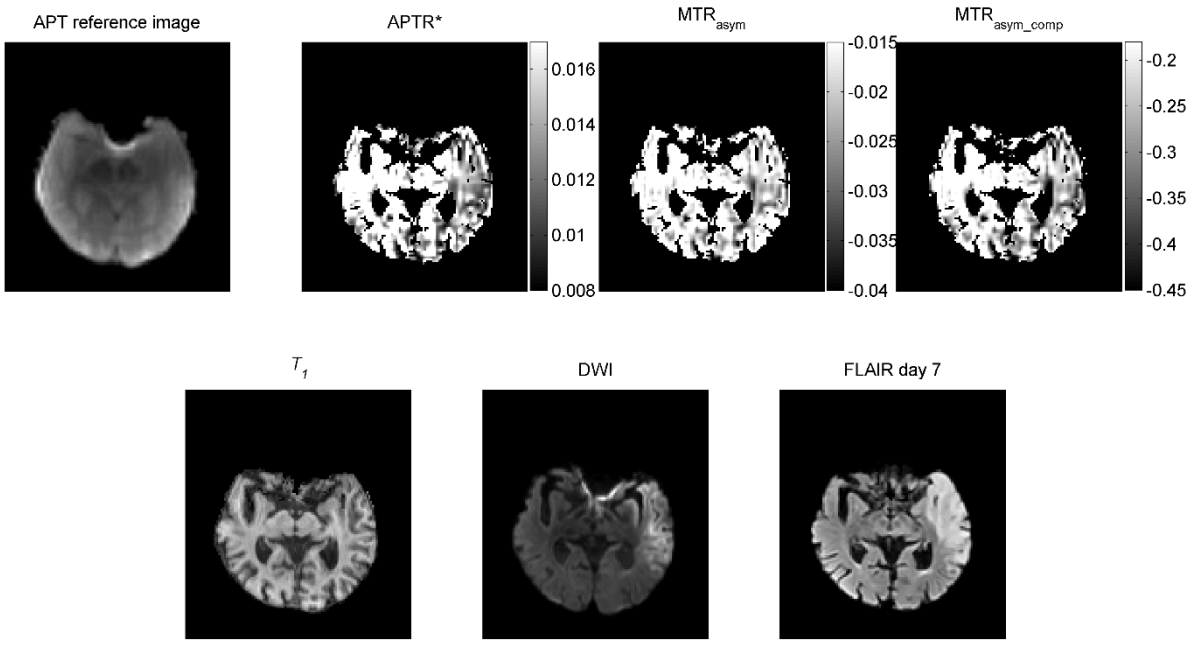


**Figure 5.4: Patient 4 data (APT, $T_1$ and DWI (b = 1000)) and the processed APT tissue results (APTR*, $MTR_{asym}$ and $MTR_{asym_comp}$) on admission, and follow-up FLAIR image on day 7. PWI was not acquired in the initial scan due to technical and time constraint. Tissue masks generated from FAST have been used to mask out the non-tissue areas such as CSF; thus, the scale bar does not reflect the quantified APT effect in these areas.**

The mean and standard deviation of each metric in the infarct core and contralateral normal appearing tissue area of each patient are shown in Figure 5.5, along with the results of the t-tests. Significant differences between APTR* in the infarct core and contralateral tissue were found for all the patients at a 5% significance level. The calculated APTR* was consistently lower in the infarct core than in the contralateral tissue with the group means and standard deviations equalling 0.0147 ± 0.0026 and 0.019 ± 0.004, respectively. When the unbounded $MTR_{asym}$ and $MTR_{asym_comp}$ in these regions were studied using the t-tests (Figure 5.5 b and c), most of the results showed significant differences but large standard deviations were observed such as $MTR_{asym_comp}$ in patients 1 and 2. When the bounded $MTR_{asym}$ and $MTR_{asym_comp}$ between the infarct core and contralateral normal appearing tissue were

analysed, significant differences between these two regions were found for all the patients at a 5 % significance level, except $MTR_{asym_comp}$ in patient 6 (labelled by a '++' symbol in Figure 5.5e). The quantified APT effect using the asymmetry measures ($MTR_{asym}$ and $MTR_{asym_comp}$) showed more negative signal in the infarct core when compared to the contralateral tissue in all cases. The group means and standard deviations of $MTR_{asym}$ were -0.012 ± 0.0055 (contralateral) and -0.0165 ± 0.0068 (infarct core). For $MTR_{asym_comp}$, the group results in the contralateral region and infarct core were -0.163 ± 0.108 and -0.233 ± 0.103, respectively. There were inter-subject variations for all the metrics investigated in either of the ROIs.

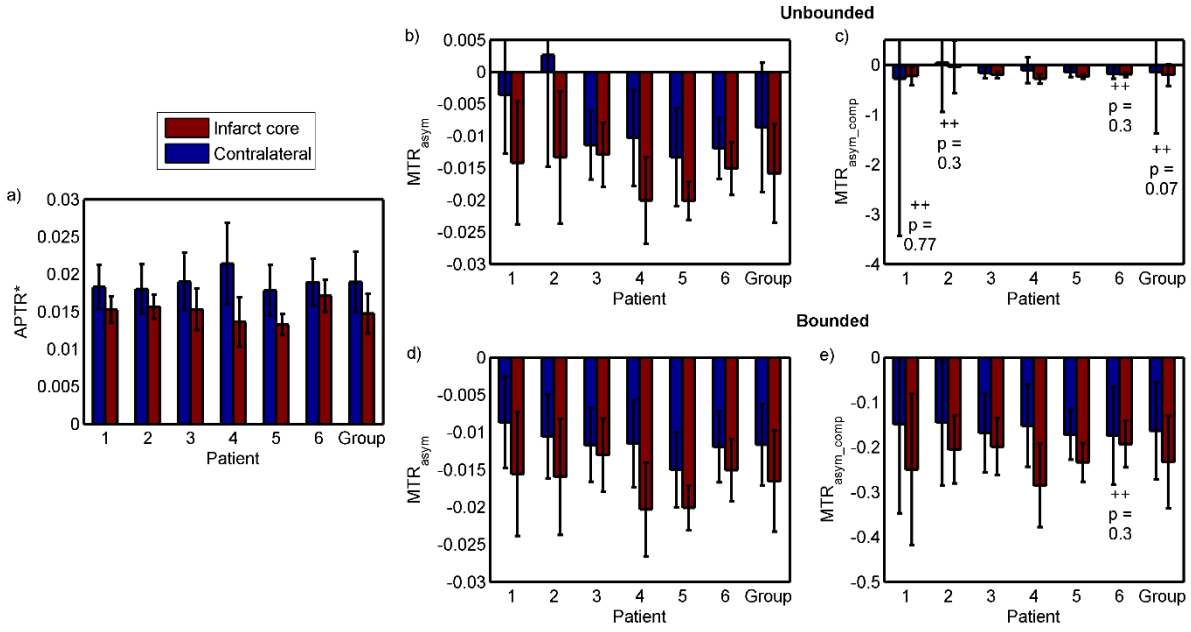


**Figure 5.5: Results of unpaired t-tests at a 5% significance level between the infarct core and contralateral normal appearing tissue region of APTR*, $MTR_{asym}$ and $MTR_{asym_comp}$, where the '++' symbols represent the non-significant differences found and the unlabelled results refer to significant differences and the 'group' label represents the average results of all the patients. The bar graphs and error bars refer to the means and standard deviations of each metric, respectively. Bounded results indicate only $MTR_{asym}$ smaller than 0 and $MTR_{asym_comp}$ within -1.5 and 0 were included, whereas unbounded refers to the results studied directly on all the calculated values.**

Table 5.3 shows the contrast between infarct core and contralateral normal appearing tissue, and the calculated CV in the contralateral tissue for all the patients; for the asymmetry analyses ($MTR_{asym}$ and $MTR_{asym_comp}$), only the bounded results are included. Although the

contrast of APTR* for each patient was not as high as the other two metrics, it was able to quantify the contralateral APT effect with smaller variation. Thus, when the ratio of contrast over $CV_{Contralateral}$ was assessed, APTR* was able to produce the highest CNR, followed by $MTR_{asym}$ and $MTR_{asym_comp}$.

**Table 5.3: Contrast (C) between infarct core and contralateral normal appearing tissue, and coefficient of variation (CV) in the contralateral tissue of APTR*, $MTR_{asym}$ and $MTR_{asym_comp}$ of each patient. All the results are expressed in percent (%); only bounded $MTR_{asym}$ and $MTR_{asym_comp}$ are included.**

| Patient | $CV_{CONTRALATERAL}$ | C | $CNR = C/CV_{CONTRALATERAL}$ |
|---|---|---|---|
| **APTR*** | | | |
| 1 | 16.08 | 9.01 | 56.03 |
| 2 | 18.46 | 7.04 | 38.14 |
| 3 | 20.51 | 10.82 | 52.75 |
| 4 | 25.33 | 22.23 | 87.76 |
| 5 | 19.02 | 14.79 | 77.76 |
| 6 | 16.52 | 5.01 | 30.33 |
| | | **Average** | **57.13** |
| | | | |
| **$MTR_{asym}$** | | | |
| 1 | 70.44 | 28.46 | 40.40 |
| 2 | 53.39 | 20.35 | 38.12 |
| 3 | 41.94 | 5.40 | 12.88 |
| 4 | 50.49 | 27.66 | 54.78 |
| 5 | 33.60 | 14.49 | 43.13 |
| 6 | 39.97 | 11.67 | 29.20 |
| | | **Average** | **36.42** |
| | | | |
| **$MTR_{asym_comp}$** | | | |
| 1 | 133.55 | 25.30 | 18.94 |
| 2 | 95.71 | 16.92 | 17.68 |
| 3 | 51.75 | 8.33 | 16.10 |
| 4 | 60.43 | 30.46 | 50.41 |
| 5 | 32.27 | 15.12 | 46.85 |
| 6 | 62.22 | 5.14 | 8.26 |
| | | **Average** | **26.37** |

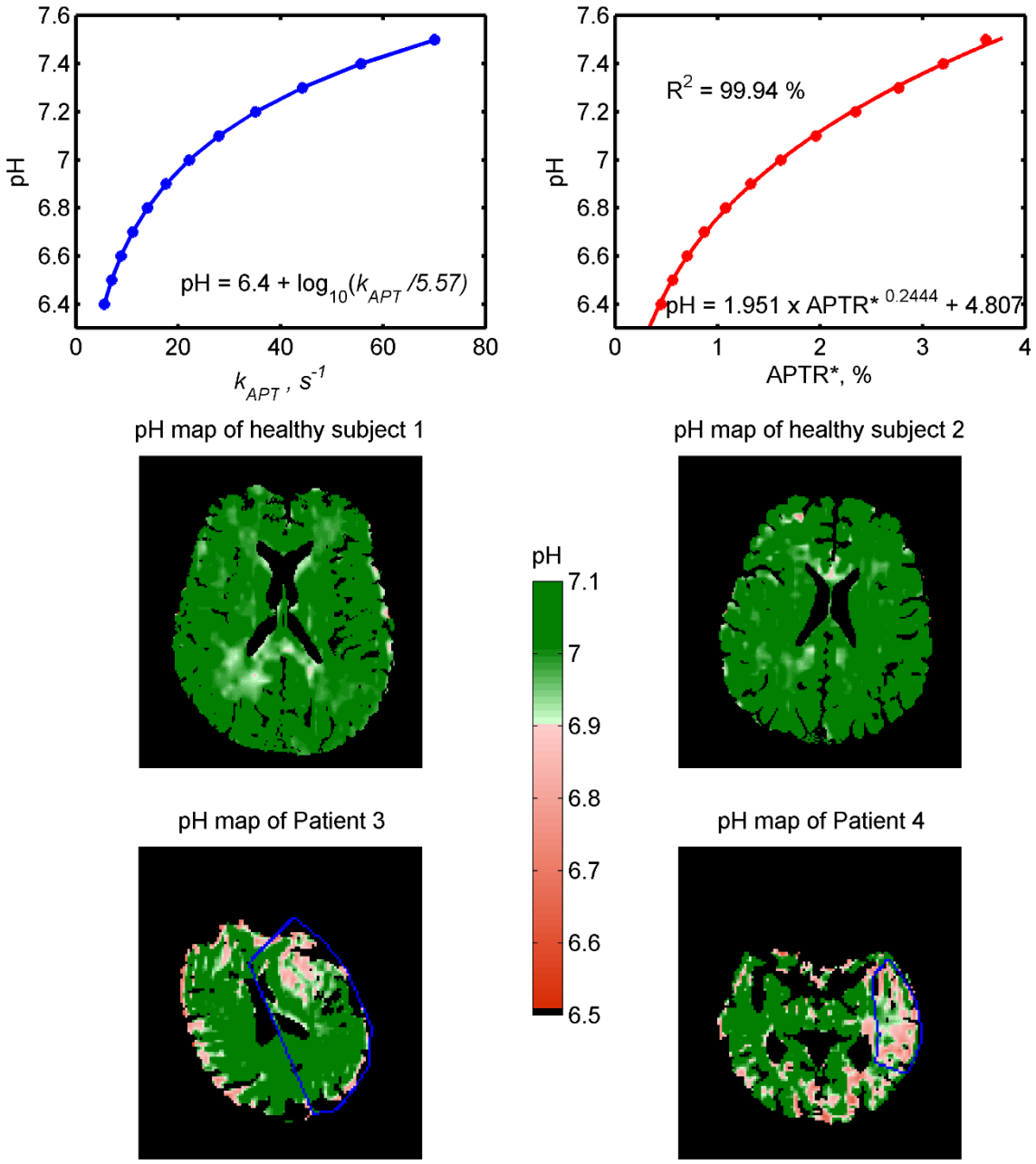


**Figure 5.6: (Top-left) A logarithmic relationship between pH and amide proton exchange rate proposed by Zhou et al. [22]. (Top-right) The pH vs APTR* relationship formed by simulations; very good fits were obtained ($R^2$ = 99.94%) for the pH values from 6.4 to 7.5. The middle and bottom row shows the quantitative pH map of healthy subjects and patients presented in Figure 5.3 and Figure 5.4, respectively, generated using the pH and APTR* relationship found. The pH scale was set based on the logarithmic relationship study [22], where pH values of 7.1 and above were normal (green), 7.1 to 6.9 were hypercapnia (light green) and below 6.9 was ischemic (pink to red). The blue lines in the patient images represent the area of infarction observed on day 7 follow-up FLAIR data. Tissue masks generated from FAST have been used to mask out the non-tissue areas such as CSF; thus, the colour scale does not reflect the quantified APT effect in these areas.**

A logarithmic relationship between the intra-cellular pH and amide proton exchange rate has previously been derived using phosphorous and WEX spectroscopy (Figure 5.6 – top-left). Using this logarithmic relationship and assuming the model parameters in water and amide pools had the mean values in Table 5.2, a further relationship between pH and APTR* was formed, where pH = 1.951 x APTR*$^{0.2444}$ + 4.807 (Figure 5.6 – top-right). Based on the pH and APTR* relationship formed, quantitative pH maps of the healthy volunteers and patients were produced as shown in Figure 5.6. Relatively homogenous pH maps were obtained for the healthy subjects whereas in the representative patient cases, lower pH values were noticeable in the ischemic area based on hyper-intensity on the admitted DWI data. Lower values were also observed around the edge of the brain and tissue areas proximal to CSF in patient data, as well as in healthy subjects but to a much smaller extent when compared to the former.

# 5.5 Discussion

This study examines different ways of quantifying the APT effect on data acquired in hyper-acute stroke patients: $MTR_{asym}$, $MTR_{asym_comp}$ and APTR*. From the results, APTR* was able to generate the smallest contrast and CV in the healthy subjects, which is desirable. When APTR* was applied to quantify the APT effect in the hyper-acute stroke patient data, significant differences were found between the infarct core and contralateral normal appearing tissue for all the patients. Without setting a proper bound for the statistical analyses, $MTR_{asym}$ and $MTR_{asym_comp}$ were found to have large variations within the ROIs. These asymmetry measures appear to be more susceptible to artefacts such as noise, imperfect fat suppression and measurement errors than the model-based analysis. When a low RF irradiation power was used in the APT imaging, the resultant $MTR_{asym}$ and $MTR_{asym_comp}$ were

found to be mostly negative unlike APTR*. Thus any pH estimation based on the asymmetry measures would be more strongly influenced by the aliphatic signal, conflicting with its intended use as a metric to describe the APT effect. Nevertheless, the asymmetry analysis method did demonstrate the ability to identify apparent APT effects. Since they can be calculated more quickly than the model-based approach, they remain suitable as a first approximation and as a means of generating non-quantitative contrast images.

APT experiments are commonly performed using a higher saturation power than that used in this study to maximize the contrast and to generate a positive difference when asymmetry analysis is used to quantify the effect. However, high power contributes to large spillover and MT effects [34], making the use of asymmetry analysis less specific to the APT effect alone. Based on the efficiency theory [29, 104], only a small power is required to fully saturate the protons that are in slow exchange with the water protons such as amide, ~ 28 Hz [22]. Therefore, the APT experiments in this study were performed using a small irradiation power to minimize the contamination from other transfer of magnetization effects. The difference in the irradiation power used may, however, have influenced the efficacy of the asymmetry measures here.

In order to speed up the model-based analysis, the average power of the Gaussian pulses was used instead of a discretization method which segments each pulse into *N* intervals; the final magnetization is achieved by propagating the calculation through all the intervals, with the calculated signals at one segment used as the initial conditions for the following one. Due to this simplification, the model fitting was not able to fit the signal well around the water centre frequency (Figure 5.1) because the continuous irradiation scheme is able to saturate the pool more efficiently, leading to narrower off resonance excitation when

compared to the pulsed saturation as used in this study. Nevertheless, the differences between the fitted parameters using the continuous approximation and discretization method for a semi-OSS and slow exchange rate protons such as amide should be small; thus, this should not affect the APTR* results here significantly [106]. This was evidenced by the relatively homogenous APTR* results obtained in the healthy subjects and significantly lower APTR* signals in the ischemic region when compared to the contralateral tissue in the patients.

When the average z-spectra across a ROI in the ischemic and contralateral tissue of patients were analysed, the APT effect was observed to decrease in the ischemic region, as was the signal in the aliphatic range when compared to the contralateral side, as shown in Figure 5.1. The change at 3.5 ppm has been attributed to the accumulation of lactate when the ischemic stroke happens, leading to pH reduction [50, 52] and a slower amide proton exchange rate, and hence a smaller APT effect [21, 22]. The post stroke effect in the aliphatic range has not been widely reported. A previous study on the animal model suggests that the saturation effect at the negative offsets is pH insensitive [102] whereas recent literature shows that the effect is pH dependent [113] under low power saturation such as the study presented here. This discrepancy may arise from the different RF irradiation powers used because NOE has been shown to be power dependent [132]. The change at the negative frequency offsets is not surprising because the brain undergoes cascaded and complex physiological adaption after ischemic injury. These adaptations have been previously reported by many spectroscopy studies such as noticeable changes in the aliphatic range during severe energy failure [133] and an increase of neutral lipid droplets in the infarcted region following induced stroke [134].

In general, it is accepted that the pH will drop in the infarct core after stroke due to the accumulation of lactate. However, it is difficult to determine whether the same degree of pH reduction also occurs in the penumbra. Thus, the comparisons of the different APT quantification methods were only performed between the infarct core and contralateral normal appearing tissue, and any other specific evaluations that could not be generalised further were not implemented. Although follow-up FLAIR data were acquired in this study, it was not suitable for defining the final infarct because the brain usually suffers from extensive swelling about a week after the ischemic injury, such as was seen in patient 3. Hence, it was difficult to accurately delineate the final infarct based on the FLAIR data at this time point and this was not used to further sub-divide the regions into ischemic penumbra and benign oligemia.

Only three fitted parameters were used to calculate the APTR* because including all the fitted parameters for the calculation required different APTR* vs pH relationships to be formed for each possible combination of parameters in the ideal 2-pool exchange model to perform the pH conversion. However, when only the selected parameters ($k_{APT}$, $M_{w0}$ and $M_{APT0}$) were used for the ideal quantification, a single APTR* vs pH relationship was adequate to convert the quantified APT effect into a quantitative pH map. Using the relationship of pH and APTR* found from simulation, quantitative pH maps were demonstrated in healthy subjects and hyper-acute stroke patients. When the proposed method was applied on the healthy volunteers, relatively homogenous pH maps were obtained, which is expected, because the body will try to maintain homeostasis. In patients, lower pH values were observed in the ischemic area as shown in Figure 5.6. These are the first quantitative pH maps

generated from APT imaging in hyper-acute stroke patients to the best of the author's knowledge.

Although realistic pH maps were generated in this study, artefacts (low pH values) were seen in the non-ischemic tissue area too, especially in the patient cases. There are a few possible factors that might explain this. Firstly, Eqn. (25) is formed using phosphorus spectroscopy by assuming that phosphate species experience the same intracellular environment as amide protons [22], which remains to be validated. Secondly, the derived relationship (Eqn. (25)) has been found to show some discrepancies with an APT study carried out elsewhere [93]. The difference has been suggested to be due to the calibrated $MTR_{asym}$ vs pH relationship, which may not be the same at different centres because the imaging technique is not standardized [21]. Furthermore, since $MTR_{asym}$ is known to contain not only the APT effect, recalibration may be necessary to form a more accurate relationship between pH and APTR* as the latter can quantify the pure APT effect by removing all the other contaminating effects using the model-based analysis. Finally, the concentration of amide protons was set to be 100 mM across the brain in the simulations to generate the pH and APTR* relationship. This is probably the one of main factors contributing to the artefacts seen on the generated pH maps, aside from the motion artefacts, because there is zero or minimal endogenous mobile protein and peptide concentration in non-tissue areas such as the CSF. Partial volumes of these low or no amide concentration regions within the tissue area may cause the model to estimate it as a low APT effect. This effect is likely to be more pronounced in the older patients observed here compared with the younger healthy subjects because of atrophy. This issue has also been reported by others using $MTR_{asym}$ [53], suggesting that a better post-processing partial volume correction technique than the one applied here is

required because the APT slice is normally thicker than the $T_1$ structural image used for segmentation.

The published literature on the application of APT imaging in stroke patients to date has a mean onset time of 4.3 days after the ischemic onset [53]. Even though the patients are scanned in the delay phase, the APT effect quantified using $MTR_{asym}$ still showed a lower signal in the ischemic area when compared to the contralateral normal appearing tissue. However, the quantified signal may not reflect the pH effect alone because the initial assumptions regarding negligible change of water relaxation time and concentration will not hold at this stage of stroke evolution. Oedema formation and inflammation are common secondary phenomena after stroke that can alter the magnetic properties of water. There may also be a change in the amide proton concentration due to the loss of cytoplasm days after the onset. Additionally, a change in the diffusivity in the ischemic area could possibly affect the exchange rate between water and amide protons. As a result, various other MRI acquisitions are required to account for all these variations such as the methods used in a previous preclinical study [91] in order to quantify the APT effect using the asymmetry analysis. However, this will increase the patient scan time beyond what is suitable for clinical stroke diagnosis, suggesting that the model-based analysis, which can account for all these variations, might be preferable.

There are other ways to quantify the APT effect such as LDA [104] and a three offset measurement approach [102], but these methods were not considered in this chapter. Although they are less contaminated by the other transfer of magnetization effects, these approaches are still not able to account for the variations mentioned above. In addition, the three offset measurement technique requires the APT effect to have a clear dip which is not so well-defined when the acquisition is performed on a 3T clinical scanner. Consequently,

using this technique to calculate the APT effect will lower the sensitivity to the small signal change caused by pH drop and thus undermine the effect.

## 5.6 Summary

In this study, different APT quantification methods were assessed on data acquired from healthy volunteers and hyper-acute stroke patients. Clear changes in the APT signal in patients within the region of ischemia, as identified from DWI, were observed using all the quantification methods. It was found that the model-based approach was more robust and performed quantitatively better at quantifying the APT effect than the widely used asymmetry measures such as $MTR_{asym}$ on both the healthy and patient APT data. Results from the model-based analysis were used to generate quantitative pH maps using published calibration data; relatively homogenous pH maps were obtained in the healthy subjects and lower pH values were seen in the ischemic tissue of hyper-acute stroke patients.

The work presented here has provided the technical capability to assess the clinical utility of APT imaging in the acute stroke management; larger patient datasets are required to aid the investigation on whether a threshold for the quantified APT effect exists to help to define tissue outcome following ischemic stroke.

# Chapter 6

# Conclusions and Future Work

# 6.1 Conclusions

Stroke is one of the leading causes of death and adult disability worldwide. Although rtPA has been shown to increase the survival rate and to reduce the disability of ischemic stroke patients, the main barriers to its wider clinical use are its restricted therapeutic window and complications, which lead to intracranial haemorrhage after the administration. Recently, APT imaging has been suggested to improve patient selection for thrombolytic treatment via imaging of intra-cellular pH because lactacidosis happens prior to cerebral cell death. However, the most widely used asymmetry analysis for the APT quantification suffers from many contaminations and is only able to generate pH-weighted contrast, not quantitative pH, maps without acquiring extra scans to correct for various stroke and non-stroke related confounding factors.

In this thesis, studies focused on moving from a qualitative (asymmetry analysis) to a more quantitative and reproducible measure (model-based analysis) for APT imaging. When performing the APT experiment, an evenly distributed sampling schedule is usually used because it is simpler to implement in the scanner and the sampling schedule enables water shift correction through interpolation. Chapter 3 shows that this kind of sampling schedule is not optimized for the parameters of interest such as labile proton exchange rate because there is negligible change around most of the collected data at the different frequency offsets when the important parameters vary. Thus, an optimization algorithm previously applied to MT and ASL was implemented to generate an OSS that sampled repeatedly around the informative frequency offsets to improve the parameters of interest estimation. The proposed OSS was found to improve the quantification of both the CEST effect and important parameter estimation in the simulations and tissue-like phantoms with different

concentrations and pH values by maximising the information present in the collected data for quantitative model-based analysis.

In chapter 4, a few ways of performing the model-based analysis were assessed: the discretization method, which is more accurate in matching the measured pulsed APT data but computationally expensive, and the continuous approximation, which is less accurate in the data fitting but is much quicker. Statistical differences between the important fitted parameter values obtained using these two methods were assessed on tissue-like phantoms with different concentrations and pH values. No significant difference was found at a 5% significance level for the important fitted model parameters such as labile proton exchange rate which is related to pH, when either of the methods was used to fit the pulsed CEST data for slowly exchanging protons. This suggests that when APT imaging is performed using a pulsed saturation, the average power approximation can replace the computationally expensive discretization method for quantitative model-based analysis. This paves the way to speed up the model-based analysis and to produce a more quantitative pH measure than the commonly used asymmetry analysis which has been the focus of the CEST imaging research community to date.

Some widely used APT quantification methods and the model-based analysis were compared using APT data acquired from healthy volunteers and hyper-acute stroke patients in chapter 5. Since the average power approximation to a pulsed APT experiment shows some discrepancies with the OSS, a semi-OSS scheme inspired by the OSS was used in this chapter, where data from a range of frequency offsets were collected but the majority of the samples were placed at and near the resonance frequency of amide protons. From these studies, it was found that model-based analysis performed better in both healthy and patient cases,

where the quantified APTR* had the smallest variation and contrast in the healthy subjects, and produced the highest CNR when used to evaluate patient data. The patient APTR* results showed the same findings as previous preclinical studies, where the lower APTR* signal region was always bigger or equal to the DWI deficit area but smaller than the hypo-perfused region. Quantitative pH maps were produced, for the first time, for the healthy subjects and hyper-acute stroke patients using APT imaging: relatively homogenous pH maps were observed for the former whereas lower pH values were seen in the ischemic tissue of the latter. Although APTR* was more robust and performed quantitatively better than the widely used asymmetry analysis, the latter could be calculated relatively fast, thus making it suitable as a first approximation and as a means of generating non-quantitative contrast images.

Gadolinium contrast agents (Gd) are widely used in clinical MRI to improve PWI in stroke assessment. The purpose of use for Gd is to reduce the longitudinal relaxation time of water protons. Since APT effect is relaxation time dependent, it may be affected by the presence of residual Gd in the bloodstream. A study regarding the influence of Gd on the quantification of APT effect post-contrast is presented in Appendix A3. When unpaired two-tail t-tests were performed between the pre- and post-contrast APT effects, significant differences were found at a 5% significance level in some of the patients, suggesting that APT imaging should be performed prior to the contrast agent administration to avoid potential misinterpretation of the APT effect.

In this thesis, studies have focused on improving CEST imaging protocol and moving from contrast measurement to a more quantitative analysis, seeking a means of facilitating the translation of APT MRI into clinical stroke imaging. Although more validation and improvement are required to increase the efficacy of the model-based analysis, the work here

has contributed to the use of a more accurate APT quantification method for clinical stroke diagnosis. From the early but encouraging results obtained in this thesis, APT imaging, which can monitor the metabolic activity of tissue, does appear to provide complimentary information to the existing imaging modalities for acute stroke management and has the potential to offer more, such as prediction for ischemic injury.

## 6.2 Future Work

The work presented here has provided the technical capability and necessary analysis to assess the utility of APT imaging in a clinical setting. The next step would be to use the techniques developed here on a larger patient dataset to investigate whether a threshold for the quantified APT effect or for pH exists to help to define tissue outcome.

A preclinical study [50] reported that APT imaging acquired within 4 hours could be used to predict the final ischemic injury at 24 hours. The results in chapter 5 suggest that this may be true in well-controlled experiments but that there is still a large gap to translate the pre-clinical findings into clinical application [135]. Since some complex physiological changes happen after the occurrence of stroke and pH may evolve over time, acquiring APT data at multiple time points, and beyond 6 hours, may be necessary to predict the final ischemic injury. This is because some smaller scale clinical trials have reported that certain groups of ischemic patients who receive thrombolysis up to nine hours post-onset still show a positive outcome [13] which may be due to collateral circulation, preventing the development of haemodynamic failure.

Examples of APT data acquired at different time points are presented in Figure 6.1, where the temporal growth of low pH region may be a good indication of poor clinical

outcome; in this patient the National Institutes of Health stroke scale (NIHSS) increased from 24 at < 6 hours of onset to 28 on day 7 follow-up.

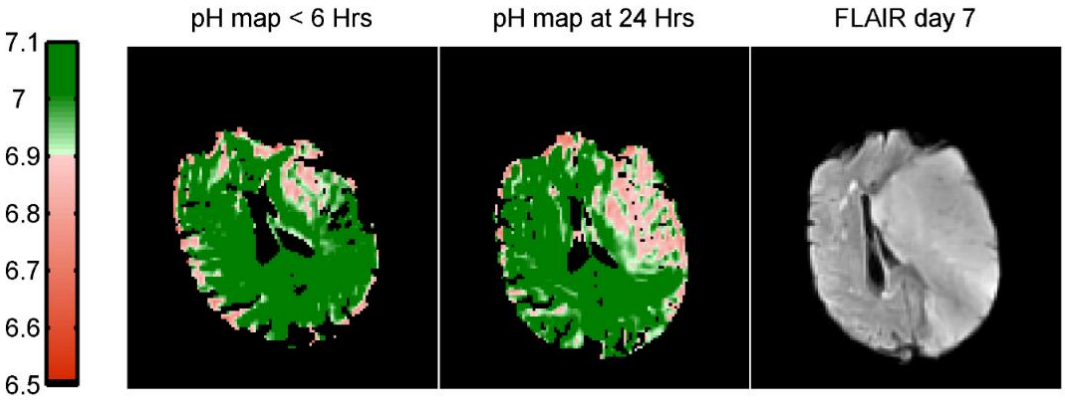


**Figure 6.1: pH maps generated based on the methods proposed in chapter 5. The growth of pH deficit area at a later time points may be an indication of poor clinical outcome, where a very large abnormality was observed in the follow up FLAIR data. The NIHSS at <6 hours was 24, at 24 hours was 25 and on day 7 follow-up was 28 (higher score indicates a more severe stroke and less likely to have a good outcome).**

Another source of transfer of magnetization effect which may be useful to understand stroke evolution and to improve the diagnosis will be presented in the next section. While this thesis has mainly concentrated on the use of model-based analysis for the ischemic stroke study, the findings or techniques developed here can also be applied to other CEST applications. The final section will thus discuss how the work here can be extended to other applications such as tumour diagnosis.

## 6.2.1 NOE

So far, all the endogenous CEST agents used in humans have resonance frequencies at positive frequency offsets with respect to the water resonance as shown in Table 2.1. However, the measured z-spectra from higher field strength scanners show that there are also some saturation effects in the negative frequency range. Only a few studies have investigated the negative offsets of the z-spectrum to date and conflicting results have been

published: some find the signal at this range to be pH insensitive [102] whereas when low power saturation is used, it has been reported to be pH dependent [113]. The RF irradiation power used is probably one of the reasons for this discrepancy. Additionally, Jones and co-workers [113] suggest that the use of three offset measurement and the choice of boundary images (Eqn. (17)) may lead to the lack of pH dependence found at the negative frequency offsets in this previous study.

The NOE is observed as a change in intensity of one resonance when the intensity of a neighbouring resonance is perturbed by saturation or inversion via dipole-dipole cross-relaxation. Various possible pathways, such as intra-molecular and inter-molecular transfer, and exchange-relay, have been proposed to contribute to the NOE [29, 113, 136]. Although the exact proportions of these contributions are still under debate and the subject of active research, the most widely used asymmetry analysis measures the combined effect of the difference between the positive and negative frequency offsets and shows that the contrast is different between the ischemic and contralateral tissue.

However, it was reported in a recent study that the amide protons have a different pH dependence than the NOE [113]. In chapter 5, the measured z-spectra in the hyper-acute stroke patients (Figure 5.1) showed that the negative offsets of the z-spectra were different between the ischemic and contralateral normal appearing tissue, suggesting that analysing these two saturation effects (CEST and NOE) separately may provide more information regarding the tissue state. Thus, one possible future study would be to use the model-based analysis proposed here to independently investigate these two saturation effects. The fitted parameters from the model-based analysis could be used to quantify the NOE effect (NOE*)

using the same way as that of calculating APTR* (Eqn. (19)), except that the ideal 2-pool exchange model would now become water + the 3rd pool (MT+NOE) in the model fitting.

An example of a NOE* result together with APTR*, DWI and follow up FLAIR images, is shown in Figure 6.2. From the figure, it is observed that a smaller NOE* signal is found in the ischemic tissue and that the lower signal area is not the same as the lower APTR* signal region. This suggests that NOE might be another potential source of signal that may possibly be useful in clinical stroke imaging and to enhance the understanding of stroke evolution and physiological changes after the ischemic onset. This is of course just one preliminary result highlighting the potential of the signal at the negative frequency offsets, and more work would need to be carried out to understand and to optimize this saturation effect.

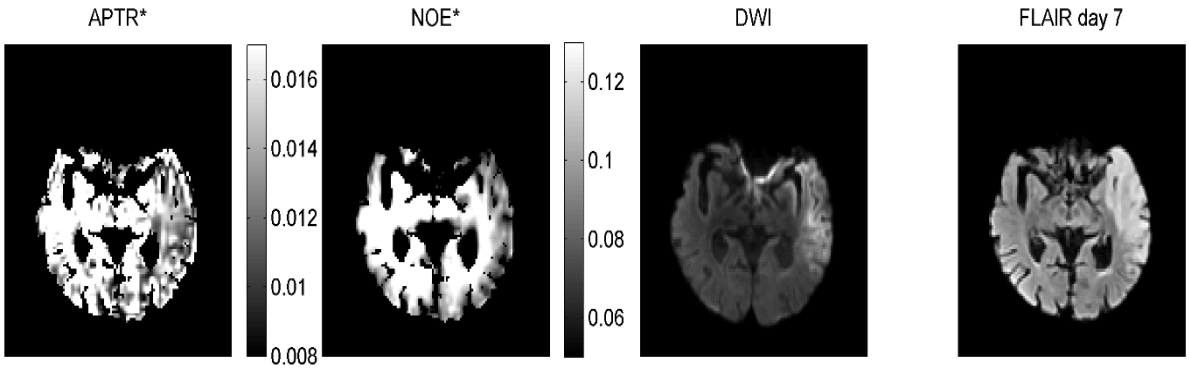


**Figure 6.2: APTR*, NOE*, DWI (b = 1000) and follow up FLAIR images of patient 4 in chapter 5, where the previous three were acquired around hyper-acute period and the latter was collected 7 days after the ischemic onset.**

## 6.2.2 Tumour Detection

As shown in chapter 2, CEST imaging has led to the study of many potential clinical applications in recent years. One of the first few proposed applications was tumour detection using endogenous mobile proteins and/or peptides. Initial studies on implanted 9L gliosarcoma tumours in the rat brain showed that $MTR_{asym}$ was higher in the tumour regions than in the contralateral normal appearing tissue, and that the tumour boundaries were

delineated better in the $MTR_{asym}$ image than in the conventional $T_1$-weighted, $T_2$-weighted and diffusion-weighted images [46].

Follow up studies in human brain tumours confirmed the initial preclinical work, where it was found that $MTR_{asym}$ was elevated in the tumour region when compared to the contralateral tissue [67] with the highest $MTR_{asym}$ signal seen in the tumour core [47]. The increase in the $MTR_{asym}$ signal was associated with higher endogenous mobile proteins and/or peptides in the tumours [46]. Other studies [25, 49] then reported that the $MTR_{asym}$ signal varied across the tumour region, leading to the suggestion that APT imaging could be used to differentiate between the tumour core and the necrotic region, as well as the surrounding oedematous area. Furthermore, the $MTR_{asym}$ signal was found to correlate well with the tumour grade, as only the high grade tumours were hyper-intense whilst the low grade tumours were iso-intense and indistinguishable from the normal tissue [47], highlighting the potential of APT imaging for non-invasive tumour grading. Later, the technique was shown to be able to differentiate between tumour recurrence and radiation necrosis [48, 137] which could not be achieved by conventional MRI modalities. Thus, the addition of APT imaging to conventional MRI techniques for tumour detection could potentially improve diagnosis and treatment planning by providing more accurate targets for biopsy, local chemotherapy, radiation therapy and tumour resection [49, 138].

APT imaging for tumour detection is usually performed using high power saturation pulses (2 – 4 μT) [46, 47, 53, 67] when asymmetry analysis is used to quantify the APT effect, in order to generate hyper-intensity in the tumour region and iso-intensity in the non-tumour tissue. High saturation power results in the typical published z-spectra showing featureless broad saturation effects, as shown in Figure 2.6. As mentioned in the previous chapters, a low

saturation power is adequate to fully saturate the slow exchange rate protons such as amides, whereas high saturation power leads to strong spillover effect and complicates the quantitative analysis.

An example of the $MTR_{asym}$ result and the measured z-spectra in the tumour region and contralateral normal appearing tissue of an APT experiment performed at 9.4 T using a moderate saturation power are shown in Figure 6.3; $MTR_{asym}$ shows an elevated signal in the tumour region and clear saturation effects at the positive and negative frequency offsets are observed.

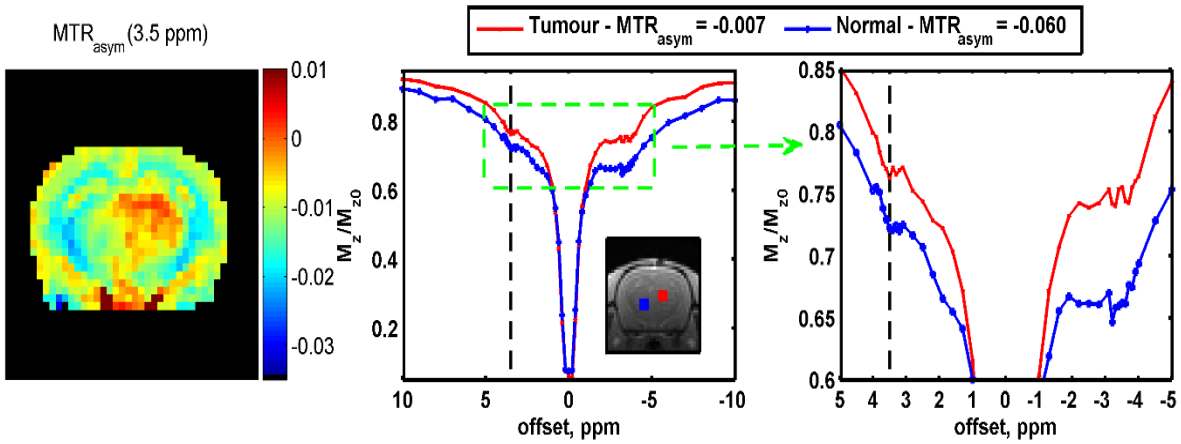


**Figure 6.3: $MTR_{asym}$ and the measured z-spectra in the tumour (red) and contralateral tissue (blue) of a rat brain at 9.4 T using a moderate saturation power (~1.8 µT). The black dashed lines are the resonance frequence of amide protons and the right most plot is the zoomed in z-spectra.**

Based on the studies of APT imaging for stroke in this thesis, it is clear that asymmetry analysis, such as $MTR_{asym}$, measures multiple transfer of magnetization effects in a mixed manner and that the analysis requires various other extra scans to correct for field inhomogeneity issues. Furthermore, when the positive and negative frequency offsets of the z-spectrum are analysed separately using LDA, the quantified effects have been reported to decrease in the tumour region, contradictory to $MTR_{asym}$ [113]. Higher water magnetic properties ($T_1$ and $T_2$) and water content in the tumours [139] due to larger extravascular

extracellular space may be the reason, leading to a reduction in the overall cell density and in all the saturation transfer effects. Nevertheless, this does not necessarily mean that the cellular protein content is smaller in the tumour region compared to the non-tumour tissue, because the water and amide concentration may increase disproportionately: the ratio of protein to water content may be smaller but the absolute protein content per cell may not. This strongly suggests that a model-based analysis has to be used to understand which factor(s) contributes to the difference of $MTR_{asym}$ in the normal and pathological tissue, and to separate and correct for the various confounding factors for more accurate quantification of the increase of absolute protein content in the tumour region.

# References


[1] The Stroke Association, "Stroke statistics," http://www.stroke.org.uk/sites/default/files/Stroke%20statistics.pdf, accessed on 5 May 2013, 2013.

[2] M. Nichols, N. Townsend, R. Luengo-Fernandez, J. Leal, A. Gray, P. Scarborough and M. Rayner, "European cardiovascular disease statistics 2012," European Heart Network, Brussels, European Society of Cardiology, Sophia Antipolis, 2012.

[3] N. Townsend, K. Wickramasinghe, P. Bhatnagar, K. Smolina, M. Nichols, J. Leal, R. Luengo-Fernandez and M. Rayner, "Coronary heart disease statistics 2012 edition," British Heart Foundation, London, 2012.

[4] J. Adamson, A. Beswick and S. Ebrahim. Is stroke the most common cause of disability? *J. Stroke Cerebrovasc. Dis. 13(4),* pp. 171-177. 2004.

[5] J. Hudson, A. Scharaschkin, M. Wilkins, K. Taylor, S. Ahmad and etc., "Reducing brain damage: faster access to better stroke care," 2005.

[6] K. Hossman. Pathophysiological basis of translational stroke research. *Folia Neuropathol. 47(3),* pp. 213-227. 2009.

[7] K. Hossmann. Pathophysiology and therapy of experimental stroke. *Cell. Mol. Neurobiol. 26(7-8),* pp. 1057-1083. 2006.

[8] K. Hossmann. Viability thresholds and the penumbra of focal ischemia. *Ann. Neurol. 36(4),* pp. 557-565. 1994.

[9] J. M. Smith, D. P. Bradley, M. F. James and C. L. H. Huang. Physiological studies of cortical spreading depression. *Biological Reviews 81(04),* pp. 457-481. 2006.

[10] M. Fisher and W. Schaebitz. An overview of acute stroke therapy: Past, present, and future. *Arch. Intern. Med. 160(21),* pp. 3196-3206. 2000.

[11] W. Hacke, T. Brott, L. Caplan, D. Meier, C. Fieschi, R. Von Kummer, G. Donnan, W. D. Heiss, N. G. Wahlgren and M. Spranger. Thrombolysis in acute ischemic stroke: Controlled trials and clinical experience. *Neurology 53(7),* pp. S3-S14. 1999.

[12] Royal College of Physicians, "National sentinel stroke clinical audit 2010 round 7," Public report for England, Wales and Northern Ireland, 2011.

[13] D. Toni, S. Lorenzano, M. L. Sacchetti, M. Fiorelli, M. De Michele and M. Principe. Specific therapies for ischaemic stroke: RTPA and others. *Neurol. Sci. 26(1),* pp. s26-28. 2005.

[14] W. Hacke, M. Kaste, E. Bluhmki, M. Brozman, A. Dávalos, D. Guidetti, V. Larrue, K. R. Lees, Z. Medeghri, T. Machnig, D. Schneider, R. Von Kummer, N. Wahlgren and D. Toni. Thrombolysis with alteplase 3 to 4.5 hours after acute ischemic stroke. *New Engl. J. Med. 359(13),* pp. 1317-1329. 2008.

[15] W. Hacke, M. Kaste, C. Fieschi, D. Toni, E. Lesaffre, R. Von Kummer, G. Boysen, E. Bluhmki, G. Höxter, M. -. Mahagne and M. Hennerici. Intravenous thrombolysis with recombinant tissue plasminogen activator for acute hemispheric stroke: The European Cooperative Acute Stroke Study (ECASS). *J. Am. Med. Assoc. 274(13),* pp. 1017-1025. 1995.

[16] W. Hacke, M. Kaste, C. Fieschi, R. Von Kummer, A. Davalos, D. Meier, V. Larrue, E. Bluhmki, S. Davis, G. Donnan, D. Schneider, E. Diez-Tejedor and P. Trouillas. Randomised double-blind placebo-controlled trial of thrombolytic therapy with intravenous alteplase in acute ischaemic stroke (ECASS II). *Lancet 352(9136),* pp. 1245-1251. 1998.

[17] C. S. Kase, A. J. Furlan, L. R. Wechsler, R. T. Higashida, H. A. Rowley, R. G. Hart, G. F. Molinari, L. S. Frederick, H. C. Roberts, J. M. Gebel, C. A. Sila, G. A. Schulz, R. S. Roberts and M. Gent. Cerebral hemorrhage after intra-arterial thrombolysis for ischemic stroke: the PROACT II trial. *Neurology 57(9),* pp. 1603-1610. 2001.

[18] C. Brekenfeld, L. Remonda, K. Nedeltchev, M. Arnold, H. P. Mattle, U. Fischer, L. Kappeler and G. Schroth. Symptomatic intracranial haemorrhage after intra-arterial thrombolysis in acute ischaemic stroke: assessment of 294 patients treated with urokinase. *J. Neurol. Neurosurg. Psychiatry 78(3),* pp. 280-285. 2007.

[19] M. Harada, N. Morita, M. Uno, J. Satomi, Y. Izumi, K. Asanuma, H. Nishitani, R. Kaji and S. Nagahiro. Incidence and clinical correlation of intracranial hemorrhages observed by 3-Tesla gradient echo T2*-weighted images following intravenous thrombolysis with recombinant tissue plasminogen activator. *Cerebrovasc. Dis. 29(6),* pp. 571-575. 2010.

[20] R. A. Gatenby and R. J. Gillies. Why do cancers have high aerobic glycolysis? *Nat. Rev. Cancer 4(11),* pp. 891-899. 2004.

[21] J. Zhou and P. C. M. van Zijl. Defining an acidosis-based ischemic penumbra from pH-weighted MRI. *Transl. Stroke Res. 3(1),* pp. 76-83. 2012.

[22] J. Zhou, J. Payen, D. A. Wilson, R. J. Traystman and P. C. M. Van Zijl. Using the amide proton signals of intracellular proteins and peptides to detect pH effects in MRI. *Nat. Med. 9(8),* pp. 1085-1090. 2003.

[23] M. A. Brown and R. C. Semelka, *MRI Basic Principles and Applications.* Wiley-Blackwell, 2003.

[24] R. B. Buxton. *Introduction to Functional Magnetic Resonance Imaging: Principles and Techniques.* Cambridge University Press, 2009.

[25] X. Zhao, Z. Wen, G. Zhang, F. Huang, S. Lu, X. Wang, S. Hu, M. Chen and J. Zhou. Three-dimensional turbo-spin-echo amide proton transfer MR imaging at 3-Tesla and its application to high-grade human brain tumors. *Mol. Imaging Biol. 15(1),* pp. 114-122. 2012.

[26] K. M. Ward and R. S. Balaban. Determination of pH using water protons and chemical exchange dependent saturation transfer (CEST). *Magnetic Resonance in Medicine 44(5),* pp. 799-802. 2000.

[27] K. M. Ward, A. H. Aletras and R. S. Balaban. A new class of contrast agents for MRI based on proton chemical exchange dependent saturation transfer (CEST). *J. Magn. Reson. 143(1),* pp. 79-87. 2000.

[28] J. Zhou and P. C. M. v. Zijl. Chemical exchange saturation transfer imaging and spectroscopy. *Prog Nucl Magn Reson Spectrosc 48(2-3),* pp. 109-136. 2006.

[29] P. C. M. van Zijl and N. N. Yadav. Chemical exchange saturation transfer (CEST): what is in a name and what isn't? *Magn. Reson. Med. 65(4),* pp. 927-948. 2011.

[30] T. Shah, L. Lu, K. M. Dell, M. D. Pagel, M. A. Griswold and C. A. Flask. CEST-FISP: a novel technique for rapid chemical exchange saturation transfer MRI at 7 T. *Magn. Reson. Med. 65(2),* pp. 432-437. 2011.

[31] P. Z. Sun, E. Wang, J. S. Cheung, X. Zhang, T. Benner and A. G. Sorensen. Simulation and optimization of pulsed radio frequency irradiation scheme for chemical exchange saturation transfer (CEST) MRI-demonstration of pH-weighted pulsed-amide proton CEST MRI in an animal model of acute cerebral ischemia. *Magn. Reson. Med. 66(4),* pp. 1042-1048. 2011.

[32] Z. Zu, K. Li, V. A. Janve, M. D. Does and D. F. Gochberg. Optimizing pulsed-chemical exchange saturation transfer imaging sequences. *Magn. Reson. Med. 66(4),* pp. 1100-1108. 2011.

[33] B. Schmitt, M. Zaiß, J. Zhou and P. Bachert. Optimization of pulse train pre-saturation for CEST imaging in clinical scanners. *Magn. Reson. Med. 65(6),* pp. 1620-1629. 2011.

[34] R. Scheidegger, E. Vinogradov and D. C. Alsop. Amide proton transfer imaging with improved robustness to magnetic field inhomogeneity and magnetization transfer asymmetry using saturation with frequency alternating RF irradiation. *Magn. Reson. Med. 66(5),* pp. 1275-1285. 2011.

[35] T. Jin, J. Autio, T. Obata and S. Kim. Spin-locking versus chemical exchange saturation transfer MRI for investigating chemical exchange process between water and labile metabolite protons. *Magn. Reson. Med. 65(5),* pp. 1448-1460. 2011.

[36] X. Song, A. A. Gilad, S. Joel, G. Liu, A. Bar-Shir, Y. Liang, M. Gorelik, J. J. Pekar, P. C. M. Van Zijl, J. W. M. Bulte and M. T. McMahon. CEST phase mapping using a length and offset varied saturation (LOVARS) scheme. *Magn. Reson. Med. 68(4),* pp. 1074-1086. 2012.

[37] J. S. Lee, R. R. Regatte and A. Jerschow. Isolating chemical exchange saturation transfer contrast from magnetization transfer asymmetry under two-frequency rf irradiation. *J. Magn. Reson. 215,* pp. 56-63. 2012.

[38] Z. Zu, V. A. Janve, J. Xu, M. D. Does, J. C. Gore and D. F. Gochberg. A new method for detecting exchanging amide protons using chemical exchange rotation transfer. *Magn. Reson. Med. 69(3),* pp. 637-647. 2013.

[39] J. I. Friedman, M. T. McMahon, J. T. Stivers and P. C. M. Van Zijl. Indirect detection of labile solute proton spectra via the water signal using frequency-labeled exchange (FLEX) transfer. *J. Am. Chem. Soc. 132(6),* pp. 1813-1815. 2010.

[40] N. N. Yadav, C. K. Jones, J. Hua, J. Xu and P. C. M. Van Zijl. Imaging of endogenous exchangeable proton signals in the human brain using frequency labeled exchange transfer imaging. *Magn. Reson. Med. 69(4),* pp. 966-973. 2013.

[41] J. Xu, N. N. Yadav, A. Bar-Shir, C. K. Jones, K. W. Y. Chan, J. Zhang, P. Walczak, M. T. Mcmahon and P. C. M. van Zijl. Variable delay multi-pulse train for fast chemical exchange saturation transfer and relayed-nuclear Overhauser enhancement MRI. *Magn. Reson. Med. doi: 10.1002/mrm.24850.* 2013.

[42] A. X. Li, R. H. E. Hudson, J. W. Barrett, C. K. Jones, S. H. Pasternak and R. Bartha. Four-pool modeling of proton exchange processes in biological systems in the presence of MRI-paramagnetic chemical exchange saturation transfer (PARACEST) agents. *Magn. Reson. Med. 60(5),* pp. 1197-1206. 2008.

[43] D. E. Woessner, S. Zhang, M. E. Merritt and A. D. Sherry. Numerical solution of the Bloch equations provides insights into the optimum design of PARACEST agents for MRI. *Magn. Reson. Med. 53(4),* pp. 790-799. 2005.

[44] M. A. Chappell, M. J. Donahue, Y. K. Tee, A. A. Khrapitchev, N. R. Sibson, P. Jezzard and S. J. Payne. Quantitative Bayesian model-based analysis of amide proton transfer MRI. *Magn. Reson. Med. 70(2),* pp. 556-567. 2012.

[45] K. Murase and N. Tanki. Numerical solutions to the time-dependent Bloch equations revisited. *Magn. Reson. Imaging 29(1),* pp. 126-131. 2011.

[46] J. Zhou, B. Lal, D. A. Wilson, J. Laterra and P. C. M. Van Zijl. Amide proton transfer (APT) contrast for imaging of brain tumors. *Magn. Reson. Med. 50(6),* pp. 1120-1126. 2003.

[47] J. Zhou, J. O. Blakeley, J. Hua, M. Kim, J. Laterra, M. G. Pomper and P. C. M. Van Zijl. Practical data acquisition method for human brain tumor amide proton transfer (APT) imaging. *Magn. Reson. Med. 60(4),* pp. 842-849. 2008.

[48] J. Zhou, E. Tryggestad, Z. Wen, B. Lal, T. Zhou, R. Grossman, S. Wang, K. Yan, D. X. Fu and E. Ford. Differentiation between glioma and radiation necrosis using molecular magnetic resonance imaging of endogenous proteins and peptides. *Nat. Med. 17(1),* pp. 130-134. 2010.

[49] Z. Wen, S. Hu, F. Huang, X. Wang, L. Guo, X. Quan, S. Wang and J. Zhou. MR imaging of high-grade brain tumors using endogenous protein and peptide-based contrast. *Neuroimage 51(2),* pp. 616-622. 2010.

[50] P. Z. Sun, J. Zhou, W. Sun, J. Huang and P. C. M. Van Zijl. Detection of the ischemic penumbra using pH-weighted MRI. *J. Cereb. Blood Flow Metab. 27(6),* pp. 1129-1136. 2007.

[51] P. Z. Sun, T. Benner, W. A. Copen and A. G. Sorensen. Early experience of translating pH-weighted MRI to image human subjects at 3 Tesla. *Stroke 41(10 SUPPL. 1),* pp. S147-S151. 2010.

[52] P. Z. Sun, J. S. Cheung, E. Wang and E. H. Lo. Association between pH-weighted endogenous amide proton chemical exchange saturation transfer MRI and tissue lactic acidosis during acute ischemic stroke. *J Cereb Blood Flow Metab 31(8),* pp. 1743-1750. 2011.

[53] X. Zhao, Z. Wen, F. Huang, S. Lu, X. Wang, S. Hu, D. Zu and J. Zhou. Saturation power dependence of amide proton transfer image contrasts in human brain tumors and strokes at 3 T. *Magn. Reson. Med. 66(4),* pp. 1033-1041. 2011.

[54] P. van Zijl, C. K. Jones, J. Ren, C. R. Malloy and A. D. Sherry. MRI detection of glycogen in vivo by using chemical exchange saturation transfer imaging (glycoCEST). *Proceedings of the National Academy of Sciences 104(11),* pp. 4359. 2007.

[55] M. Haris, K. Cai, A. Singh, H. Hariharan and R. Reddy. In vivo mapping of brain myo-inositol. *Neuroimage 54(3),* pp. 2079-2085. 2011.

[56] M. Haris, A. Singh, K. Cai, K. Nath, R. Crescenzi, F. Kogan, H. Hariharan and R. Reddy. MICEST: a potential tool for non-invasive detection of molecular changes in Alzheimer's disease. *J. Neurosci. Methods 212(1),* pp. 87-93. 2013.

[57] D. L. Longo, W. Dastrù, G. Digilio, J. Keupp, S. Langereis, S. Lanzardo, S. Prestigio, O. Steinbach, E. Terreno, F. Uggeri and S. Aime. Iopamidol as a responsive MRI-chemical exchange saturation transfer contrast agent for pH mapping of kidneys: in vivo studies in mice at 7 T. *Magn. Reson. Med. 65(1),* pp. 202-211. 2011.

[58] D. L. Longo, A. Busato, S. Lanzardo, F. Antico and S. Aime. Imaging the pH evolution of an acute kidney injury model by means of iopamidol, a MRI-CEST pH-responsive contrast agent. *Magn. Reson. Med. 70(3),* pp. 859-864. 2012.

[59] K. W. Y. Chan, G. Liu, X. Song, H. Kim, T. Yu, D. R. Arifin, A. A. Gilad, J. Hanes, P. Walczak, P. C. M. Van Zijl, J. W. M. Bulte and M. T. McMahon. MRI-detectable pH nanosensors incorporated into hydrogels for in vivo sensing of transplanted-cell viability. *Nat. Mater. 12(3),* pp. 268-275. 2013.

[60] G. Angelovski, T. Chauvin, R. Pohmann, N. K. Logothetis and E. Tóth. Calcium-responsive paramagnetic CEST agents. *Bioorg. Med. Chem. 19(3),* pp. 1097-1105. 2011.

[61] B. Yoo and M. D. Pagel. A PARACEST MRI contrast agent to detect enzyme activity. *J. Am. Chem. Soc. 128(43),* pp. 14032-14033. 2006.

[62] F. A. Nasrallah, G. Pagès, P. W. Kuchel, X. Golay and K. Chuang. Imaging brain deoxyglucose uptake and metabolism by glucoCEST MRI. *J. Cereb. Blood Flow Metab. 33(8),* pp. 1270-1278. 2013.

[63] S. Walker-Samuel, R. Ramasawmy, F. Torrealdea, M. Rega, V. Rajkumar, S. P. Johnson, S. Richardson, M. Gonçalves, H. G. Parkes, E. Årstad, D. L. Thomas, R. B. Pedley, M. F. Lythgoe and X. Golay. In vivo imaging of glucose uptake and metabolism in tumors. *Nat. Med. 19(8),* pp. 1067-1072. 2013.

[64] Y. Wu, C. E. Carney, M. Denton, E. Hart, P. Zhao, D. N. Streblow, A. D. Sherry and M. Woods. Polymeric PARACEST MRI contrast agents as potential reporters for gene therapy. *Org Biomol Chem 8(23),* pp. 5333-5338. 2010.

[65] A. A. Gilad, M. T. McMahon, P. Walczak, P. T. Winnard Jr., V. Raman, H. W. M. Van Laarhoven, C. M. Skoglund, J. W. M. Bulte and P. C. M. Van Zijl. Artificial reporter gene providing MRI contrast based on proton exchange. *Nat. Biotechnol. 25(2),* pp. 217-219. 2007.

[66] D. L. Polders and J. M. Hoogduin. Chemical exchange saturation transfer MR imaging: potential clinical applications. *PET Clin. 8(3),* pp. 245-257. 2013.

[67] C. K. Jones, M. J. Schlosser, P. C. M. Van Zijl, M. G. Pomper, X. Golay and J. Zhou. Amide proton transfer imaging of human brain tumors at 3T. *Magn. Reson. Med. 56(3),* pp. 585-592. 2006.

[68] A. N. Dula, E. M. Asche, B. A. Landman, E. B. Welch, S. Pawate, S. Sriram, J. C. Gore and S. A. Smith. Development of chemical exchange saturation transfer at 7T. *Magn. Reson. Med. 66(3),* pp. 831-838. 2011.

[69] D. Liu, J. Zhou, R. Xue, Z. Zuo, J. An and D. J. J. Wang. Quantitative characterization of nuclear Overhauser enhancement and amide proton transfer effects in the human brain at 7 Tesla. *Magn. Reson. Med. doi: 10.1002/mrm.24560.* 2012.

[70] O. E. Mougin, R. C. Coxon, A. Pitiot and P. A. Gowland. Magnetization transfer phenomenon in the human brain at 7 T. *Neuroimage 49(1),* pp. 272-281. 2010.

[71] G. Jia, R. Abaza, J. D. Williams, D. L. Zynger, J. Zhou, Z. K. Shah, M. Patel, S. Sammet, L. Wei, R. R. Bahnson and M. V. Knopp. Amide proton transfer MR imaging of prostate cancer: a preliminary study. *J. Magn. Reson. Imaging 33(3),* pp. 647-654. 2011.

[72] A. N. Dula, L. R. Arlinghaus, R. D. Dortch, B. E. Dewey, J. G. Whisenant, G. D. Ayers, T. E. Yankeelov and S. A. Smith. Amide proton transfer imaging of the breast at 3 T: establishing reproducibility and possible feasibility assessing chemotherapy response. *Magn. Reson. Med. 70(1),* pp. 216-224. 2012.

[73] L. Gerigk, B. Schmitt, B. Stieltjes, F. Röder, M. Essig, M. Bock, H. -. Schlemmer and M. Röthke. 7 Tesla imaging of cerebral radiation necrosis after arteriovenous malformations treatment using amide proton transfer (APT) imaging. *J. Magn. Reson. Imaging 35(5),* pp. 1207-1209. 2012.

[74] M. Kim, J. Gillen, B. A. Landman, J. Zhou and P. C. M. Van Zijl. Water saturation shift referencing (WASSR) for chemical exchange saturation transfer (CEST) experiments. *Magn. Reson. Med. 61(6),* pp. 1441-1450. 2009.

[75] M. Kim, Q. Chan, M. -. Anthony, K. M. Cheung, D. Samartzis and P. -. Khong. Assessment of glycosaminoglycan distribution in human lumbar intervertebral discs using chemical exchange saturation transfer at 3 T: Feasibility and initial experience. *NMR Biomed. 24(9),* pp. 1137-1144. 2011.

[76] A. Singh, M. Haris, K. Cai, V. B. Kassey, F. Kogan, D. Reddy, H. Hariharan and R. Reddy. Chemical exchange saturation transfer magnetic resonance imaging of human knee cartilage at 3 T and 7 T. *Magn. Reson. Med. 68(2),* pp. 588-594. 2012.

[77] G. Varma, R. E. Lenkinski and E. Vinogradov. Keyhole chemical exchange saturation transfer. *Magn. Reson. Med. 68(4),* pp. 1228-1233. 2012.

[78] I. Krusche-Mandl, B. Schmitt, L. Zak, S. Apprich, S. Aldrian, V. Juras, K. M. Friedrich, S. Marlovits, M. Weber and S. Trattnig. Long-term results 8 years after autologous osteochondral transplantation: 7 T gagCEST and sodium magnetic resonance imaging with morphological and clinical correlation. *Osteoarthritis Cartilage 20(5),* pp. 357-363. 2012.

[79] B. Schmitt, Š. Zbýn, D. Stelzeneder, V. Jellus, D. Paul, L. Lauer, P. Bachert and S. Trattnig. Cartilage quality assessment by using glycosaminoglycan chemical exchange saturation transfer and 23Na MR imaging at 7 T. *Radiology 260(1),* pp. 257-264. 2011.

[80] S. Haneder, S. R. Apprich, B. Schmitt, H. J. Michaely, S. O. Schoenberg, K. M. Friedrich and S. Trattnig. Assessment of glycosaminoglycan content in intervertebral discs using chemical exchange saturation transfer at 3.0 Tesla: preliminary results in patients with low-back pain. *Eur. Radiol. 23(3),* pp. 861-868. 2013.

[81] K. Cai, M. Haris, A. Singh, F. Kogan, J. H. Greenberg, H. Hariharan, J. A. Detre and R. Reddy. Magnetic resonance imaging of glutamate. *Nat. Med. 18(2),* pp. 302-306. 2012.

[82] A. Singh, K. Cai, M. Haris, H. Hariharan and R. Reddy. On B1 inhomogeneity correction of in vivo human brain glutamate chemical exchange saturation transfer contrast at 7T. *Magn. Reson. Med. 69(3),* pp. 818-824. 2013.

[83] F. Kogan, A. Singh, C. Debrosse, M. Haris, K. Cai, R. P. Nanga, M. Elliott, H. Hariharan and R. Reddy. Imaging of glutamate in the spinal cord using GluCEST. *Neuroimage 77,* pp. 262-267. 2013.

[84] A. P. Dagher, A. Aletras, P. Choyke and R. S. Balaban. Imaging of urea using chemical exchange-dependent saturation transfer at 1.5 T. *J. Magn. Reson. Imaging 12(5),* pp. 745-748. 2000.

[85] M. Chesler. Regulation and modulation of pH in the brain. *Physiol. Rev. 83(4),* pp. 1183-1221. 2003.

[86] K. Wüthrich and G. Wagner. Nuclear magnetic resonance of labile protons in the basic pancreatic trypsin inhibitor. *J. Mol. Biol. 130(1),* pp. 1-18. 1979.

[87] A. K. Covington, R. A. Robinson and R. G. Bates. The ionization constant of deuterium oxide from 5 to 50°. *J. Phys. Chem. 70(12),* pp. 3820-3824. 1966.

[88] P. Z. Sun, J. Zhou, J. Huang and P. Van Zijl. Simplified quantitative description of amide proton transfer (APT) imaging during acute ischemia. *Magn. Reson. Med. 57(2),* pp. 405-410. 2007.

[89] P. Z. Sun, Y. Murata, J. Lu, X. Wang, E. H. Lo and A. G. Sorensen. Relaxation-compensated fast multi-slice amide proton transfer (APT) imaging of acute ischemic stroke. *Magn. Reson. Med. 59(5),* pp. 1175-1182. 2008.

[90] P. Z. Sun, J. S. Cheung, E. Wang, T. Benner and A. G. Sorensen. Fast multi-slice pH-weighted chemical exchange saturation transfer (CEST) MRI with unevenly segmented RF irradiation. *Magn. Reson. Med. 65(2),* pp. 588-594. 2011.

[91] P. Z. Sun, E. Wang and J. S. Cheung. Imaging acute ischemic tissue acidosis with pH-sensitive endogenous amide proton transfer (APT) MRI-correction of tissue relaxation and concomitant RF irradiation effects toward mapping quantitative cerebral tissue pH. *Neuroimage 60(1),* pp. 1-6. 2012.

[92] K. T. Jokivarsi, Y. Hiltunen, P. I. Tuunanen, R. A. Kauppinen and O. H. J. Gröhn. Correlating tissue outcome with quantitative multi-parametric MRI of acute cerebral ischemia in rats. *Journal of Cerebral Blood Flow & Metabolism 30(2),* pp. 415-427. 2010.

[93] K. T. Jokivarsi, H. I. Gröhn, O. H. Gröhn and R. A. Kauppinen. Proton transfer ratio, lactate, and intracellular pH in acute cerebral ischemia. *Magn. Reson. Med. 57(4),* pp. 647-653. 2007.

[94] A. J. Huang, C. Jones, R. Leigh, S. Jarso and P. van Zijl, "Initial application of pH-weighted imaging with pulsed CEST to image an acute ischemic stroke patient," *In: Proceedings of the 20th Annual Meeting of ISMRM,* Melbourne, Australia 2012. p 1007.

[95] C. Xu, C. Labadie, A. Pampel, J. B. Fiebach and H. E. Möller, "Development of a 3D CEST pulse sequence with embedded field map and low SAR for pH-weighted contrast in stroke patients," *In: Proceedings of the 20th Annual Meeting of ISMRM,* Melbourne, Australia 2012. p 4266.

[96] T. Yoshiura, A. Hiwatashi, O. Togao, J. Keupp, J. Yamashita, K. Kikuchi, Y. Suzuki, M. Obara and H. Honda, "Amide proton transfer (APT) imaging of acute cerebral infarction: a

preliminary study on clinical patients," *In: Proceedings of the 21th Annual Meeting of ISMRM,* Salt Lake City, USA 2013. p 213.

[97] M. J. Donahue, A. Tietze, I. K. Mikkelsen, L. Ostergaard, M. Strother, S. Smith and J. Blicher, "Application of chemical exchange saturation transfer (CEST) MRI in acute human stroke patients demonstrates new potential for visualization of tissue acidosis and infarction risk," *In: Proceedings of the 21th Annual Meeting of ISMRM,* Salt Lake City, USA 2013. p 427.

[98] G. Harston, Y. K. Tee, M. Chappell, N. Blockley, T. Okell, J. Levman, F. Sheerin, M. Cellerini, P. Jezzard, S. Payne and J. Kennedy, "pH-weighted imaging in acute stroke: how does it compare to conventional techniques?" *The XXVIth International Symposium on Cerebral Blood Flow, Metabolism and Function & XIth International Conference on Quantification of Brain Function with PET,* Shanghai, China 2013.

[99] P. Z. Sun, P. C. M. Van Zijl and J. Zhou. Optimization of the irradiation power in chemical exchange dependent saturation transfer experiments. *J. Magn. Reson. 175(2),* pp. 193-200. 2005.

[100] M. T. McMahon, A. A. Gilad, J. Zhou, P. Z. Sun, J. W. M. Bulte and P. C. M. Van Zijl. Quantifying exchange rates in chemical exchange saturation transfer agents using the saturation time and saturation power dependencies of the magnetization transfer effect on the magnetic resonance imaging signal (QUEST and QUESP): pH calibration for poly-L-lysine and a starburst dendrimer. *Magn. Reson. Med. 55(4),* pp. 836-847. 2006.

[101] E. Terreno, J. Stancanello, D. Longo, D. Delli Castelli, L. Milone, H. M. H. F. Sanders, M. B. Kok, F. Uggeri and S. Aime. Methods for an improved detection of the MRI-CEST effect. *Contrast Media Mol. Imaging 4(5),* pp. 237-247. 2009.

[102] T. Jin, P. Wang, X. Zong and S. Kim. MR imaging of the amide-proton transfer effect and the pH-insensitive nuclear Overhauser effect at 9.4 T. *Magn. Reson. Med. 69(3),* pp. 760-770. 2012.

[103] R. V. Mulkern and M. L. Williams. The general solution to the Bloch equation with constant RF and relaxation terms: application to saturation and slice selection. *Med. Phys. 20(1),* pp. 5-13. 1993.

[104] C. K. Jones, D. Polders, J. Hua, H. Zhu, H. J. Hoogduin, J. Zhou, P. Luijten and P. C. van Zijl. In vivo three-dimensional whole-brain pulsed steady-state chemical exchange saturation transfer at 7 T. *Magn. Reson. Med. 67(6),* pp. 1579-1589. 2012.

[105] P. Z. Sun, C. T. Farrar and A. G. Sorensen. Correction for artifacts induced by $B_0$ and $B_1$ field inhomogeneities in pH-sensitive chemical exchange saturation transfer (CEST) imaging. *Magn. Reson. Med. 58(6),* pp. 1207-1215. 2007.

[106] Y. K. Tee, A. A. Khrapitchev, N. R. Sibson, S. J. Payne and M. A. Chappell. Evaluating the use of a continuous approximation for model-based quantification of pulsed chemical exchange saturation transfer (CEST). *J. Magn. Reson. 222,* pp. 88-95. 2012.

[107] J. Stancanello, E. Terreno, D. Delli Castelli, C. Cabella, F. Uggeri and S. Aime. Development and validation of a smoothing-splines-based correction method for improving the analysis of CEST-MR images. *Contrast Media Mol. Imaging 3(4),* pp. 136-149. 2008.

[108] C. H. Cunningham, J. M. Pauly and K. S. Nayak. Saturated double-angle method for rapid B1+ mapping. *Magn. Reson. Med. 55(6),* pp. 1326-1333. 2006.

[109] R. Stollberger and P. Wach. Imaging of the active B1 field in vivo. *Magn. Reson. Med. 35(2),* pp. 245-251. 1996.

[110] K. L. Desmond and G. J. Stanisz. Understanding quantitative pulsed CEST in the presence of MT. *Magn. Reson. Med. 67(4),* pp. 979-990. 2012.

[111] R. M. Henkelman, G. J. Stanisz and S. J. Graham. Magnetization transfer in MRI: a review. *NMR Biomed. 14(2),* pp. 57-64. 2001.

[112] R. M. Henkelman, X. Huang, G. Qing-San Xiang, S. D. Swanson and M. J. Bronskill. Quantitative interpretation of magnetization transfer. *Magn. Reson. Med. 29(6),* pp. 759-766. 1993.

[113] C. K. Jones, A. Huang, J. Xu, R. A. E. Edden, M. Schär, J. Hua, N. Oskolkov, D. Zacà, J. Zhou, M. T. McMahon, J. J. Pillai and P. C. M. van Zijl. Nuclear Overhauser enhancement (NOE) imaging in the human brain at 7T. *Neuroimage 77,* pp. 114-124. 2013.

[114] W. T. Dixon, J. Ren, A. J. M. Lubag, J. Ratnakar, E. Vinogradov, I. Hancu, R. E. Lenkinski and A. D. Sherry. A concentration-independent method to measure exchange rates in PARACEST agents. *Magn. Reson. Med. 63(3),* pp. 625-632. 2010.

[115] P. Z. Sun. Simultaneous determination of labile proton concentration and exchange rate utilizing optimal RF power: radio frequency power (RFP) dependence of chemical exchange saturation transfer (CEST) MRI. *J. Magn. Reson. 202(2),* pp. 155-161. 2010.

[116] P. Z. Sun, Y. Wang, G. Xiao and R. Wu. Simultaneous experimental determination of labile proton fraction ratio and exchange rate with irradiation radio frequency power-dependent quantitative CEST MRI analysis. *Contrast Media Mol. Imaging 8(3),* pp. 246-251. 2013.

[117] P. Z. Sun and A. Gregory Sorensen. Imaging pH using the chemical exchange saturation transfer (CEST) MRI: correction of concomitant RF irradiation effects to quantify cest MRI for chemical exchange rate and pH. *Magn. Reson. Med. 60(2),* pp. 390-397. 2008.

[118] M. Cercignani and D. C. Alexander. Optimal acquisition schemes for in vivo quantitative magnetization transfer MRI. *Magn. Reson. Med. 56(4),* pp. 803-810. 2006.

[119] J. Xie, D. Gallichan, R. N. Gunn and P. Jezzard. Optimal design of pulsed arterial spin labeling MRI experiments. *Magn. Reson. Med. 59(4),* pp. 826-834. 2008.

[120] P. Z. Sun, J. Zhou, W. Sun, J. Huang and P. C. M. Van Zijl. Suppression of lipid artifacts in amide proton transfer imaging. *Magn. Reson. Med. 54(1),* pp. 222-225. 2005.

[121] H. Zhu, C. K. Jones, P. C. M. Van Zijl, P. B. Barker and J. Zhou. Fast 3D chemical exchange saturation transfer (CEST) imaging of the human brain. *Magn. Reson. Med. 64(3),* pp. 638-644. 2010.

[122] J. Hua, C. K. Jones, J. Blakeley, S. A. Smith, P. C. M. Van Zijl and J. Zhou. Quantitative description of the asymmetry in magnetization transfer effects around the water resonance in the human brain. *Magn. Reson. Med. 58(4),* pp. 786-793. 2007.

[123] J. Zhou, D. A. Wilson, P. Z. Sun, J. A. Klaus and P. C. M. Van Zijl. Quantitative description of proton exchange processes between water and endogenous and exogenous agents for WEX, CEST, and APT experiments. *Magn. Reson. Med. 51(5),* pp. 945-952. 2004.

[124] P. Z. Sun, T. Benner, A. Kumar and A. G. Sorensen. Investigation of optimizing and translating pH-sensitive pulsed-chemical exchange saturation transfer (CEST) imaging to a 3T clinical scanner. *Magn. Reson. Med. 60(4),* pp. 834-841. 2008.

[125] Y. K. Tee, A. A. Khrapitchev, N. R. Sibson, S. J. Payne and M. A. Chappell. Optimal sampling schedule for chemical exchange saturation transfer. *Magn. Reson. Med.* 70, pp. 1251-1262, 2013.

[126] P. Z. Sun. Simplified and scalable numerical solution for describing multi-pool chemical exchange saturation transfer (CEST) MRI contrast. *J. Magn. Reson. 205(2),* pp. 235-241. 2010.

[127] T. W. Okell, M. A. Chappell, M. E. Kelly and P. Jezzard. Cerebral blood flow quantification using vessel-encoded arterial spin labeling. *J. Cereb. Blood Flow Metab. doi: 10.1038/jcbfm.2013.129.* 2013.

[128] S. M. Smith. Fast robust automated brain extraction. *Hum. Brain Mapp. 17(3),* pp. 143-155. 2002.

[129] M. Jenkinson, P. Bannister, M. Brady and S. Smith. Improved optimization for the robust and accurate linear registration and motion correction of brain images. *Neuroimage 17(2),* pp. 825-841. 2002.

[130] M. A. Chappell, A. R. Groves, B. Whitcher and M. W. Woolrich. Variational Bayesian inference for a nonlinear forward model. *IEEE Trans Signal Process 57(1),* pp. 223-236. 2009.

[131] Y. Zhang, M. Brady and S. Smith. Segmentation of brain MR images through a hidden Markov random field model and the expectation-maximization algorithm. *IEEE Trans. Med. Imaging 20(1),* pp. 45-57. 2001.

[132] J. Zhou, X. Hong, X. Zhao, J. Gao and J. Yuan. APT-weighted and NOE-weighted image contrasts in glioma with different RF saturation powers based on magnetization transfer ratio asymmetry analyses. *Magn. Reson. Med. 70(2),* pp. 320-327. 2013.

[133] J. M. Hakumäki, O. H. J. Gröhn, T. M. Pirttilä and R. A. Kauppinen. Increased macromolecular resonances in the rat cerebral cortex during severe energy failure as detected by 1H nuclear magnetic resonance spectroscopy. *Neurosci. Lett. 212(3),* pp. 151-154. 1996.

[134] C. Gasparovic, G. A. Rosenberg, J. A. Wallace, E. Y. Estrada, K. Roberts, A. Pastuszyn, W. Ahmed and G. D. Graham. Magnetic resonance lipid signals in rat brain after experimental stroke correlate with neutral lipid accumulation. *Neurosci. Lett. 301(2),* pp. 87-90. 2001.

[135] K. Hossmann. The two pathophysiologies of focal brain ischemia: implications for translational stroke research. *J. Cereb. Blood Flow Metab. 32(7),* pp. 1310-1316. 2012.

[136] K. L. Desmond, F. Moosvi and G. J. Stanisz. Mapping of amide, amine, and aliphatic peaks in the CEST spectra of murine xenografts at 7 T. *Magn. Reson. Med. doi: 10.1002/mrm.24822.* 2013.

[137] S. Wang, E. Tryggestad, T. Zhou, M. Armour, Z. Wen, D. -. Fu, E. Ford, P. C. M. Van Zijl and J. Zhou. Assessment of MRI parameters as imaging biomarkers for radiation necrosis in the rat brain. *Int. J. Radiat. Oncol. Biol. Phys. 83(3),* pp. e431-e436. 2012.

[138] J. Zhou, H. Zhu, M. Lim, L. Blair, A. Quinones-Hinojosa, S. A. Messina, C. G. Eberhart, M. G. Pomper, J. Laterra, P. B. Barker, P. C. M. van Zijl and J. O. Blakeley. Three-dimensional amide proton transfer MR imaging of gliomas: Initial experience and comparison with gadolinium enhancement. *J. Magn. Reson. Imaging doi: 10.1002/jmri.24067.* 2013.

[139] I. C. Kiricuta Jr. and V. Simplaceanu. Tissue water content and nuclear magnetic resonance in normal and tumor tissues. *Cancer Res. 35(5),* pp. 1164-1167. 1975.

[140] R. A. Jones, O. Haraldseth, J. Schjøtt, H. Brurok, P. Jynge, A. N. Oksendal and P. A. Rinck. Effect of Gd-DTPA-BMA on magnetization transfer: application to rapid imaging of cardiac ischemia. *J. Magn. Reson. Imaging 3(1),* pp. 31-39. 1993.

[141] P. Sharma, J. Socolow, S. Patel, R. I. Pettigrew and J. N. Oshinski. Effect of Gd-DTPA-BMA on blood and myocardial T 1 at 1.5T and 3T in humans. *J. Magn. Reson. Imaging 23(3),* pp. 323-330. 2006.

[142] S. C. L. Deoni. High-resolution T1 mapping of the brain at 3T with driven equilibrium single pulse observation of T1 with high-speed incorporation of RF field inhomogeneities (DESPOT1-HIFI). *Journal of Magnetic Resonance Imaging 26(4),* pp. 1106-1111. 2007.

[143] P. Caravan. Strategies for increasing the sensitivity of gadolinium based MRI contrast agents. *Chem. Soc. Rev. 35(6),* pp. 512-523. 2006.

# Appendix

## A1 2-pool Exchange Model

A 2-pool exchange model (water and amine protons labelled as w and cest, respectively) was used to perform the numerical simulation. The model consists of six differential equations with respect to time:

$$\frac{dM_{wx}}{dt} = -\Delta_w M_{wy} - K_{2w} M_{wx} + k_{cest} M_{cestx},$$

$$\frac{dM_{wy}}{dt} = \Delta_w M_{wx} - K_{2w} M_{wy} + k_{cest} M_{cesty} - \omega_1 M_{wz},$$

$$\frac{dM_{wz}}{dt} = \frac{M_{w0}}{T_{1w}} - K_{1w} M_{wz} + k_{cest} M_{cestz} + \omega_1 M_{wy},$$

$$\frac{dM_{cestx}}{dt} = -\Delta_{cest} M_{cesty} - K_{2cest} M_{cestx} + k_w M_{wx},$$

$$\frac{dM_{cesty}}{dt} = \Delta_{cest} M_{cestx} - K_{2cest} M_{cesty} + k_w M_{wy} - \omega_1 M_{cestz},$$

$$\frac{dM_{cestz}}{dt} = \frac{M_{cest0}}{T_{1cest}} - K_{1cest} M_{cestz} + k_w M_{wz} + \omega_1 M_{cesty}. \quad \text{(A1)}$$

where the subscripts *x*, *y* and *z* refer to the direction; $\omega_1$ refers to the amplitude of the RF irradiation (1μT ~= 42.6Hz); $M_{q0}$ is the initial magnetization, $\Delta_q = \omega_q - \omega$, ($\omega$ denotes the frequency offset of the applied RF saturation pulse and $\omega_q$ is the resonance frequency of the pool), $k_q$ is the exchange rate, $T_{1 \text{ or } 2\,q}$ is the longitudinal or transverse relaxation time, respectively, and $K_{1 \text{ or } 2\,q} = 1/T_{1 \text{ or } 2\,q} + k_q$, where subscript $q$ refers to either pool w or

cest, and all the $\omega$ terms are expressed in radians. These coupled equations are linear and can be arranged in the form of $d\boldsymbol{M}/dt = \boldsymbol{AM} + \boldsymbol{B}$, where:

$$\boldsymbol{A_{2pools}} = \begin{bmatrix} -K_{2w} & -\Delta_w & 0 & k_{cest} & 0 & 0 \\ \Delta_w & -K_{2w} & -\omega_1 & 0 & k_{cest} & 0 \\ 0 & \omega_1 & -K_{1w} & 0 & 0 & k_{cest} \\ k_w & 0 & 0 & -K_{2cest} & -\Delta_{cest} & 0 \\ 0 & k_w & 0 & \Delta_{cest} & -K_{2cest} & -\omega_1 \\ 0 & 0 & k_w & 0 & \omega_1 & -K_{1cest} \end{bmatrix},$$

$$\boldsymbol{B_{2pools}} = \begin{bmatrix} 0 & 0 & \frac{M_{w0}}{T_{1w}} & 0 & 0 & \frac{M_{cest0}}{T_{1cest}} \end{bmatrix}^T,$$

$$\boldsymbol{M_{2pools}} = [M_{wx} \quad M_{wy} \quad M_{wz} \quad M_{cestx} \quad M_{cesty} \quad M_{cestz}]^T.$$

The subscript *2pools* denotes the variables shown are for a 2-pool exchange model. The analytical solution of the coupled equations in Eqn. (A1) is:

$$\boldsymbol{M} = e^{(\boldsymbol{A}*T_{sat})} * (\boldsymbol{M_0} + \boldsymbol{A^{-1}B}) - \boldsymbol{A^{-1}B},$$

where $T_{sat}$ is the total saturation time and $\boldsymbol{M_{0_2pools}} = [0 \quad 0 \quad M_{w0} \quad 0 \quad 0 \quad M_{cest0}]^T$.

# A2 3-pool Exchange Model

For quantitative analysis of the *in vitro* data, a 3-pool model was used – w, cest and magnetization transfer (MT) effect. The third pool was added because agarose exhibited MT effect which could be represented by a Gaussian lineshape (32). In order to model the MR behaviour of a 3-pool exchange system, there should be nine coupled equations. However, several studies (19, 25, 32) have shown that it is not necessary to include the *x* and *y* components of the MT pool and that there is negligible exchange between CEST and MT pool. As a result, seven differential equations are deemed adequate for the model-based analysis. They are quite similar to Eqn. (A1) with one additional differential equation for the MT pool,

with an extra term added to $dM_{wz}/dt$ and $k_w$ in $dM_{cest\ x,y,z}/dt$ changed to $k_{cest_w} = M_{cest0}k_{cest}/M_{w0}$:

$$\frac{dM_{wz}}{dt} = \frac{M_{w0}}{T_{1w}} - K_{1w}M_{wz} + k_{cest}M_{cestz} + \omega_1 M_{wy} + k_{MT}M_{MTz}\,,$$

$$\frac{dM_{MTz}}{dt} = \frac{M_{MT0}}{T_{1MT}} - (K_{1MT} + R_{rfb})M_{MTz} + k_{MT}M_{wz}\,,$$

where $R_{rfb} = \pi{\omega_1}^2 g_c\big(2\pi(\omega_{MT} - \omega)\big)$; $g_c\big(2\pi(\omega_{MT} - \omega)\big)$ is the Gaussian lineshape which can be defined as $T_{2MT}/[\pi(1 + (2\pi(\omega_{MT} - \omega)T_{2MT})^2)]$. These coupled equations can also be arranged in the form of $d\boldsymbol{M}/dt = \boldsymbol{AM} + \boldsymbol{B}$, where:

$$\boldsymbol{A_{3pools}} = \begin{bmatrix} -K_{2w} & -\Delta_w & 0 & k_{cest} & 0 & 0 & 0 \\ \Delta_w & -K_{2w} & -\omega_1 & 0 & k_{cest} & 0 & 0 \\ 0 & \omega_1 & -K_{1w} & 0 & 0 & k_{cest} & k_{MT} \\ k_{cest_w} & 0 & 0 & -K_{2cest} & -\Delta_{cest} & 0 & 0 \\ 0 & k_{cest_w} & 0 & \Delta_{cest} & -K_{2cest} & -\omega_1 & 0 \\ 0 & 0 & k_{cest_w} & 0 & \omega_1 & -K_{1cest} & 0 \\ 0 & 0 & k_{MT_w} & 0 & 0 & 0 & -l_{MT} \end{bmatrix},$$

$$\boldsymbol{B_{3pools}} = \begin{bmatrix} 0 & 0 & \frac{M_{w0}}{T_{1w}} & 0 & 0 & \frac{M_{cest0}}{T_{1cest}} & \frac{M_{MT0}}{T_{1MT}} \end{bmatrix}^T,$$

$$\boldsymbol{M_{3pools}} = [M_{wx} \quad M_{wy} \quad M_{wz} \quad M_{cestx} \quad M_{cesty} \quad M_{cestz} \quad M_{MTz}]^T\,,$$

$k_{MT_w} = M_{MT0}k_{MT}/M_{w0}$ and $l_{MT} = (K_{1MT} + R_{rfb})$. The analytical solution of the 3-pool exchange model is the same as the 2-pool case:

$$\boldsymbol{M} = e^{(\boldsymbol{A}*T_{sat})} * (\boldsymbol{M_0} + \boldsymbol{A^{-1}B}) - \boldsymbol{A^{-1}B}\,,$$

where $\boldsymbol{M_{0_3pools}} = [0 \quad 0 \quad M_{w0} \quad 0 \quad 0 \quad M_{cest0}\ M_{MT0}]^T$.

# A3 Quantification of Amide Proton Transfer Effect Pre- and Post-Gadolinium Contrast Agent Administration[§]

## A3.1 Introduction

Gadolinium contrast agents (Gd) are commonly used in clinical MRI to increase the contrast for angiography and tumour diagnosis, and to improve cerebral perfusion assessment. It is widely known that the administration of Gd will reduce the longitudinal relaxation time of water protons, $T_{1w}$ [140, 141]. A study of $T_{1w}$ pre- and post-Gd administration on blood showed that the reduction could be more than 50% of the pre-contrast value at 3T even 30 minutes after infusion [141].

Amide proton transfer (APT) imaging is an emerging chemical exchange saturation transfer (CEST) MRI technique for pH mapping that has potential clinical applications in penumbra identification following ischemic stroke [22, 50, 53, 91], in discrimination of tumour and radiation necrosis [48] or normal tissue [71], and tumour grading in brain tumour patients [25, 47].

The magnetization transfer ratio asymmetry analysis ($MTR_{asym}$) is $T_{1w}$ dependent [22], hence may be affected by the presence of residual Gd in post-contrast imaging. However, to date no study has compared the differences in APT imaging before and after Gd administration to determine whether the effect is significant or the sensitivity to contrast is of concern in clinical protocols since perfusion weighted imaging using Gd is often acquired

[§] Reproduced with permission from John Wiley and Sons. This appendix has been published in the Journal of Magnetic Resonance Imaging.
Y.K. Tee, M.J. Donahue, G. Harston, S.J. Payne, and M.A. Chappell, Quantification of amide proton transfer effect pre- and post-gadolinium contrast agent administration, Journal of Magnetic Resonance Imaging, in press.

in stroke assessment and Gd enhanced $T_1$-weighted imaging improves cancer diagnosis when used in conjunction with other conventional MRI techniques. This information is particularly pertinent to compare the efficacy of APT and Gd-based imaging since post-contrast APT imaging may be affected by the presence of residual Gd.

In this study, APT data were acquired in patients with internal carotid stenosis pre- and post-contrast to examine the extent of $T_{1w}$ change on $MTR_{asym}$ and to determine whether APT imaging should be performed pre-contrast to avoid potential misinterpretation of the APT effect.

## A3.2 Materials and Methods

### *A3.2.1 Simulation*

The modified Bloch equations were used to simulate the effect of $T_{1w}$ changes on the z-spectrum. A 3-pool model consisting of water protons (w), amide protons (cest) and magnetization transfer (MT) plus nuclear Overhauser effects (MT+NOE) following [44] was used to simulate the z-spectra in MATLAB (Mathworks, Natick, MA, USA). A pulsed saturation scheme was simulated at 3T with 50 Gaussian pulses, where each pulse had a flip angle of 184° and pulse cycle of 40 ms with 50% duty cycle. The pulses were discretized into 1024 segments and crusher gradients with alternating signs applied during the inter-pulse delays were modeled by setting the transverse magnetization to zero [106]. The saturation was applied from -4.5 to 4.5 ppm with 0.3 ppm increments. It was assumed that the readout was performed after all the pulses had been applied to match the 2D APT sequence used in the experimental data.

The water proton relaxation time, $T_{1w}$ was set to 1.3 s [142] for the pre-contrast value and different post-contrast times were simulated, varying from 10 to 50 % less than the pre-value. Root mean square (RMS) differences between the pre- and different post-contrast z-spectra were calculated to form a linear relationship between the percentage reduction in the $T_1$ of water and the effect on the z-spectrum. The remaining parameters in the model were assumed to be unaffected by the introduction of Gd and set according to the literature [44, 104, 122]: longitudinal relaxation times, $T_{1cest}$ = 0.77 s, $T_{1(MT+NOE)}$ = 1 s; transverse relaxation times, $T_{2w}$ = 50 ms, $T_{2cest}$ = 10 ms, $T_{2(MT+NOE)}$ = 0.2 ms; proton exchange rate, $k_{cest}$ = 28 $s^{-1}$, $k_{(MT+NOE)}$ = 40 $s^{-1}$; proton concentration, $M_{w0}$ = 111.2 M, $M_{cest0}$ = 72 mM, $M_{(MT+NOE)0}$ = 7.15 M; chemical shifts, $\omega_w$ = 0 ppm, $\omega_{cest}$ = 3.5 ppm, $\omega_{(MT+NOE)}$ = -2.41 ppm.

### *A3.2.2 MRI Experiment*

Four patients who were to undergo carotid endarterectomy provided informed consent and were scanned at 3T (Siemens Verio) using APT and diffusion-weighted imaging (DWI) sequences, according to a research protocol approved by the Institutional Review Board, both before and after surgery. A $T_1$ structural image with pixel dimensions = 1.72 x 1.72 x 2 mm was also acquired for each patient. The DWI data were acquired before the contrast infusion using b values of 0 and 1000 s/$mm^2$, matrix size = 128 x 128 x 27 and spatial dimensions = 1.5625 x 1.5625 x 4.5 $mm^3$.

APT data were collected pre and post intra-venous bolus injection of 0.1 mmol/kg 0.5M chelated Gd followed by a 20 ml saline flush. The post-contrast scan was acquired approximately 3 minutes after Gd administration given during a dynamic susceptibility contrast (DSC) scan, as would be typical in a clinical scenario. Single slice transverse imaging was performed mid brain for the APT data with TR/TE=4000/26 ms, matrix size = 80 x 80 and

pixel dimensions = 3 x 3 x 5 $mm^3$. The APT saturation was performed using the following RF parameters: 50 Gaussian pulses with flip angle = 184° and duration of 20 ms with 20 ms spacing each, to achieve an equivalent continuous saturation $B_1$ value of 0.55 µT (average power). Data were acquired for saturation frequency offsets from -4.5 to 4.5 ppm with 0.3 ppm increment plus an unsaturated image, resulting in 32 volumes acquired in 2 min 55 s.

*A3.2.3 Data Processing and Analysis*

Motion artefacts were corrected using FMRIB's Linear Image Registration Tool (FLIRT) in the FSL package [129]. The different frequency offset images were registered to the unsaturated APT image using 2D rigid body registration with three degrees of freedom. The brain extraction tool (BET) in the FSL package [128] was used to remove the skull and non-brain tissue in the $T_1$ structural scan. Since the field of view of the APT image in the z-direction was small, the brain of the unsaturated APT image was extracted by padding the end slices in both directions, copying the end slices several times, running the tool and then removing the added slices (option Z in BET). Subsequently the slice of the $T_1$ brain image which corresponded to the APT imaging plane was extracted and registered to the unsaturated APT brain using FLIRT.

The registered $T_1$ slice was then segmented using FMRIB's Automated Segmentation Tool (FAST) [131] into cerebrospinal fluid (CSF), grey and white matter (GM & WM) using a 0.1 Markov random field (MRF) beta value for main segmentation phase and bias field smoothing. The segmented brain regions were inspected after the automatic segmentation to remove regions of prior infarction, if any, by cross checking with the DWI data. The GM and WM marks were created using a 90% threshold on the partial volume estimates generated by FAST to obtain voxels that are as near as possible to pure GM or WM.

$B_0$ inhomogeneity was corrected using the shift in water centre frequency obtained by fitting the modified Bloch equations (3 pools following [44]) to the collected CEST data [106, 125]. RMS differences between the average measured pre- and post-contrast z-spectra in the GM and WM, respectively, were calculated after the shift correction to estimate the associated percentage of change in $T_{1w}$ in the post-contrast scans using the relationship derived from the simulations.

Magnetization transfer ratio (MTR) was calculated according to MTR = $1 - M(\Delta\omega)/M_0$, where $\Delta\omega$ refers to saturation frequency offsets at ± 3.5 ppm and $M_0$ is the unsaturated signal. Only values of pre- and post-contrast MTR greater than 0 were included when studying the effect of Gd on MTR to filter out the noise in the measurement and unmasked non-brain area if any. $MTR_{asym}$, defined as MTR(3.5ppm) – MTR(-3.5ppm), was also calculated. Differences in the images of pre- and post-contrast were shown by subtraction (pre – post) after aligning them using FLIRT to minimize the movements between the scans.

Two-tailed unpaired t-tests were performed between the pre- and post-contrast $MTR_{asym}$ in GM and WM respectively using the masks generated from FAST, to examine whether Gd had significant effect on the $MTR_{asym}$ calculated. The statistical evaluations were done to the APT data in the GM and WM acquired both before and after the surgery in individual patients, and also at a group level, where the pre- and post-contrast data from all the patients in the GM or WM were grouped accordingly and then the t-tests were performed on them as a whole. In order to exclude the artefacts and noise near the boundary of the brain area, the t-tests were performed for the $MTR_{asym}$ values from -0.05 to 0 (-5 to 0 %) only (the APT effect should be within this bound at 3T for the power used in this study [29, 104]).

## A3.3 Results

Simulated and example measured z-spectra are shown in Figure A.1, where the top left plot is the change of simulated z-spectra with different $T_{1w}$, and the remaining plots are measured post-surgery data: the first row shows the pre- and post-contrast average z-spectra in WM of representative patients 1 and 3, and their measured z-spectra in GM are shown in the bottom row. When the longitudinal relaxation of water pool $T_{1w}$ was reduced in the simulation, the degree of saturation decreased, resulting in a z-spectrum with higher magnitude. In general, the change of measured z-spectra *in vivo* after Gd administration was consistent with the simulation. This change was observed for all the post-contrast z-spectra in GM and WM both before and after the surgery (Suppl. Figure A.1 and Suppl. Figure A.2).

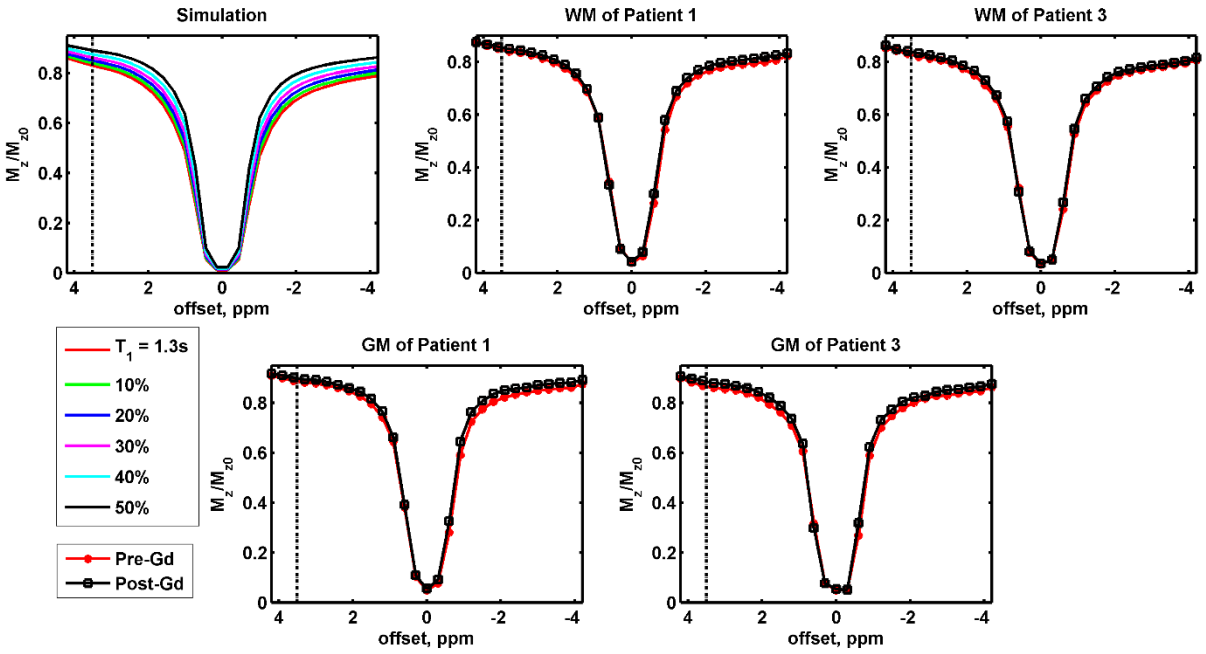


**Figure A.1: The top left plot is the simulated z-spectra with different $T_{1w}$ values, where $T_{1w}$ = 1.3 s was used as the reference and the different colours represented $T_{1w}$ was 10 to 50% less than the reference. The remaining plots in the first row are the experimentally measured z-spectra in WM of patient 1 and 3, and their z-spectra in GM are shown in the bottom row. All the measured results shown in this figure are the APT data collected after the surgery. The dot-dash lines are the chemical shift of amide protons (3.5 ppm).**

Figure A.2 (left) shows a linear relationship between the percentage of $T_{1w}$ reductions (y) and RMS differences of the simulated pre- and post-contrast z-spectra formed using simulations, where y = 576.4 * RMS + 0.05783. The post-contrast $T_{1w}$ reductions in the GM and WM of each patient before and after surgery estimated using the relationship found are presented in Figure A.2 (middle and right). The after surgery $T_{1w}$ reductions were consistently higher in the GM and WM of all the patients when compared to the before surgery reductions. When assessing the $T_{1w}$ change in the different compartment of the brain either before or after surgery, the percentage of reductions were always larger in the GM when compared to the WM. Before surgery, the post-contrast $T_{1w}$ reductions were mostly below 10% across the brain for all the patients, except the change in GM of patient 4. After surgery, the reduction in the WM of all the patients was below 10% whereas the decrease was more than 10% but less than 20% in the GM.

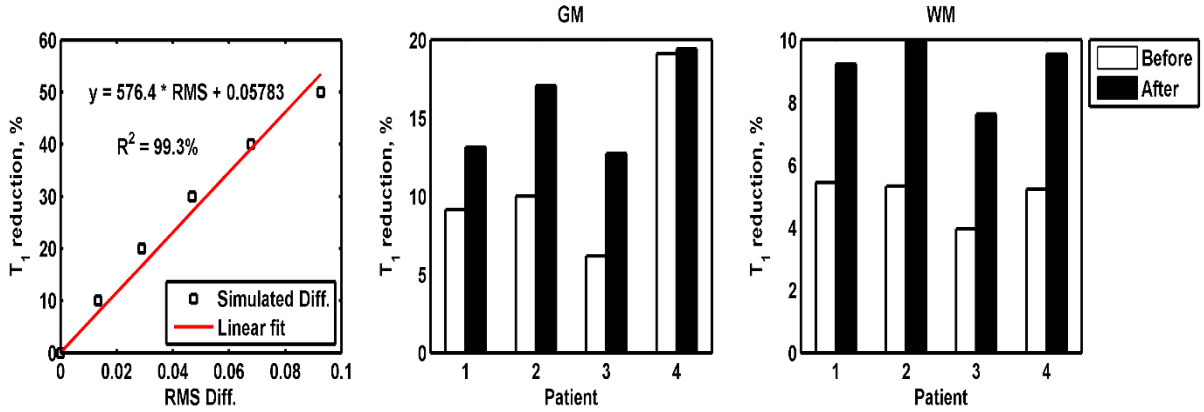


**Figure A.2: (left) A linear relationship between the percentage of $T_{1w}$ change and RMS differences of the simulated pre- and post-contrast z-spectra was formed using simulation. Estimated post-contrast $T_{1w}$ change in the GM (middle) and WM (right) of each patient before and after surgery based on the linear relationship found.**

Figure A.3 shows the pre- and post-contrast, and pre- minus post-contrast difference in MTR and $MTR_{asym}$ of all the patients both before and after the surgery. The red arrows in the figure indicate a prior infarct in patient 4 (cross-checked with DWI). In this region, both the MTR and $MTR_{asym}$ had values similar to CSF in their respective measures.

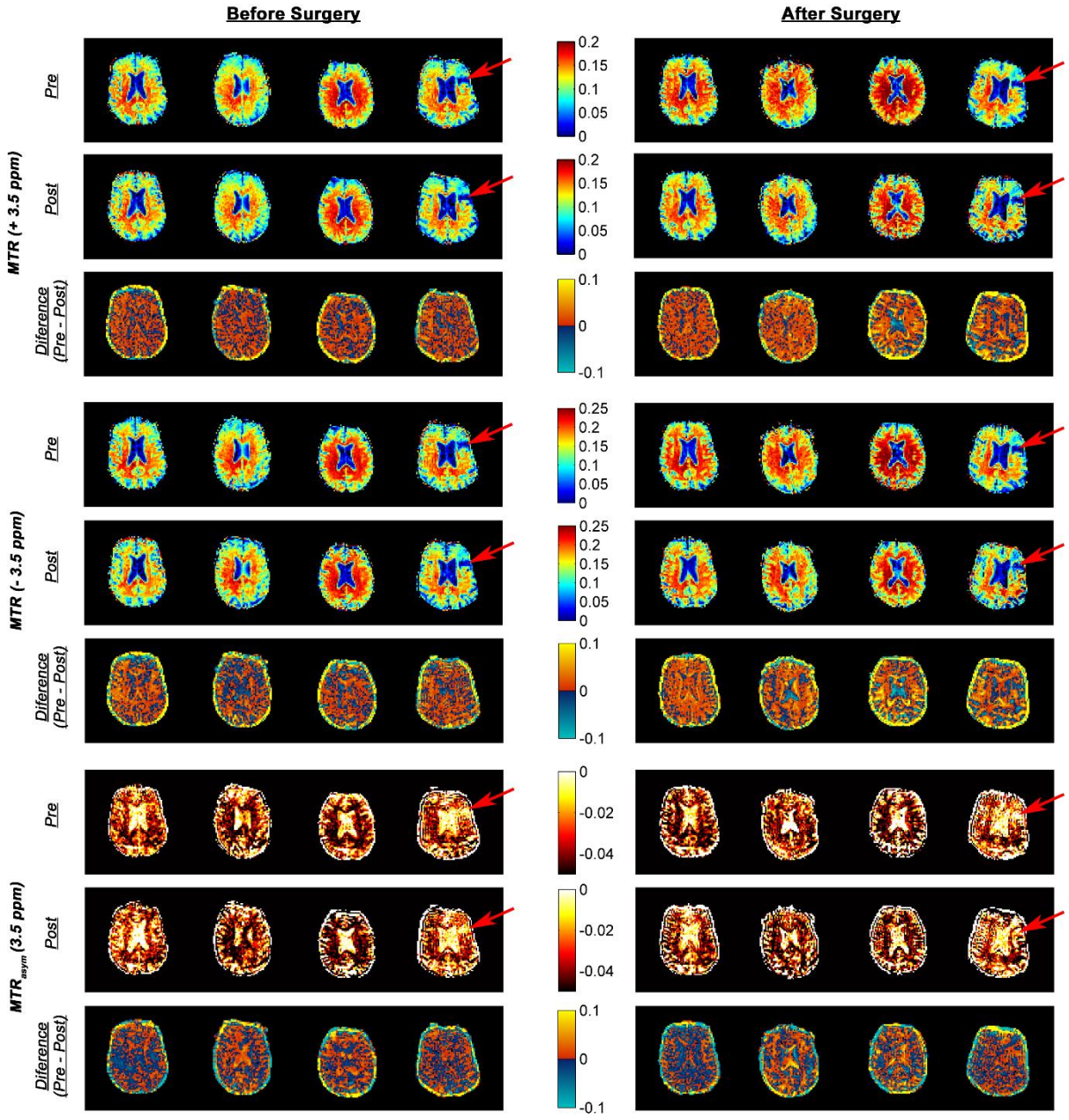


**Figure A.3: Pre- and post-contrast MTR (± 3.5 ppm) and $MTR_{asym}$ (3.5 ppm) of each patient before and after surgery. The difference of MTRs and $MTR_{asym}$ pre- and post-Gd administration were plotted directly below their respective post-images. The red arrows show a prior infarct in patient 4 (cross-checked with DWI data and found CSF-like signal in the area).**

Pre- and post-contrast MTR at ± 3.5 ppm in the segmented GM and WM of each patient before and after surgery are shown in Figure A.4. The mean of post-contrast MTR values showed a decrease when compared to the pre-values, except before surgery MTR (-3.5ppm) in GM of patient 3. This was in good agreement with the observed z-spectra change in Figure A.1.

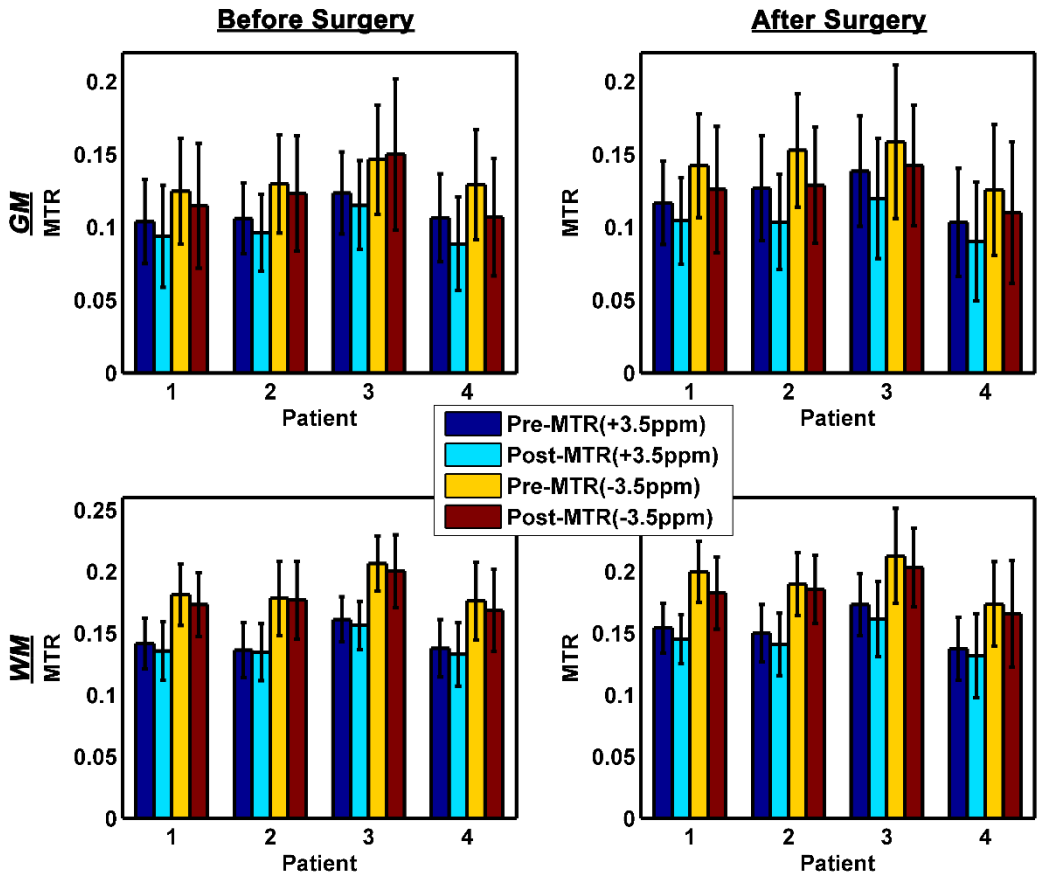


**Figure A.4: Bar graphs with error bars showing the means and standard deviations of pre- and post-contrast MTR values at ± 3.5 ppm, respectively, in the GM and WM of each patient. In order to minimize the noise in the measurement and imperfect segmentation, only MTR values greater than 0 were included.**

The mean and standard deviation of $MTR_{asym}$ in the GM and WM of each patient pre- and post-contrast are shown in Figure A.5, along with the results of the t-tests. Significant differences between pre- and post-contrast $MTR_{asym}$ at a 5% significance level were found in 25% of the patients recruited. Significance was also detected in WM at the group level both before and after surgery, but only in GM after surgery. Before surgery, GM of patient 4 and WM of patient 3 showed significant difference and after surgery, it was observed in GM and WM of patient 1. In the simulation, $MTR_{asym}$ became less negative when $T_{1w}$ reduced. The majority of the post-contrast values were less negative than the pre-contrast which is in agreement with the simulation but in a few cases (GM of patient 1 to 3 before surgery), the

reverse was observed. Regardless of the presence or absence of Gd, the $MTR_{asym}$ values were always more negative in the WM when compared to the GM.

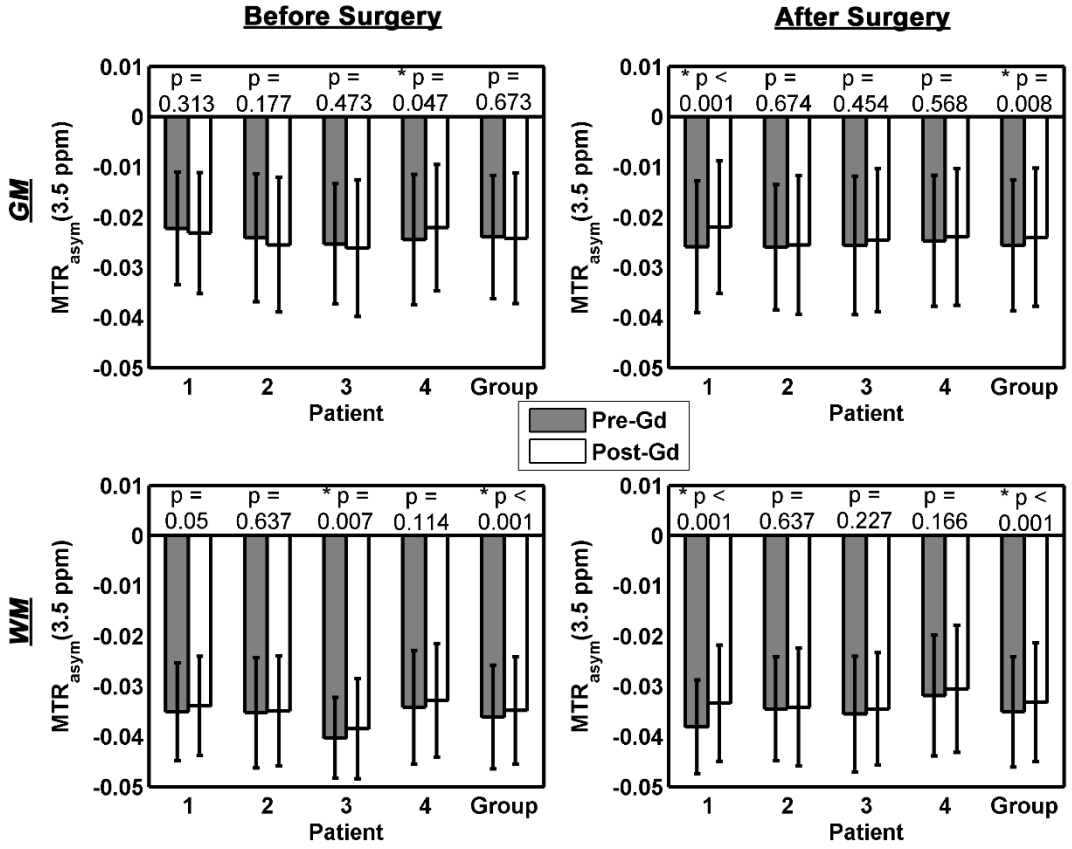


**Figure A.5: The bar graphs and error bars are the means and standard deviations of $MTR_{asym}$ values respectively, within -5 to 0 %, before and after surgery in the GM and WM of each patient. Two-tailed unpaired t-tests were performed on the pre- and post-contrast $MTR_{asym}$ values in different region of the patient brain and also at the group level, where asterisks (*) refer to a significant difference found at a 5% significance level.**

## A3.4 Discussion

This study analysed the change of APT signal after the administration of Gd and performed statistical evaluations to examine whether the presence of residual Gd in the post-contrast APT imaging can cause quantification of the effect to be significantly different from its pre-contrast values. According to the simulations, when the longitudinal relaxation time of water protons decreases, the degree of saturation decreased, resulting in a z-spectrum with higher magnitude. In general, all the post-contrast z-spectra acquired *in vivo* both before and

after the surgery were in agreement with the simulations. The change resulted in a pre- and post-contrast difference in the MTR images, with the majority of brain regions exhibited a positive difference.

Although APT imaging was performed some time after the Gd infusion, residual Gd would be present within the blood stream and thus appeared to affect the quantification of $MTR_{asym}$. A previous work [140] has shown that MTR is sensitive to the changes in $T_{1w}$ induced by Gd; this has also been observed in our results. In theory, $MTR_{asym}$, defined as the difference of MTR at ± 3.5 ppm, should be less sensitive to this effect because it is an asymmetry measure, but the results in this study suggest that Gd may asymmetrically affect the APT spectrum, possibly related to the presence of NOE and/or dynamic spatial-temporal distribution of Gd in the brain during the post-contrast scan.

The $MTR_{asym}$ values were found to be negative, contrary to the pure CEST saturation effect that would in theory result in a positive difference. This phenomenon has been widely observed and occurs due to a broad saturation effect at the negative frequency offsets of the z-spectrum attributed to NOE [29]. A 3-pool model was used in the simulation with NOE and classical MT grouped as a single asymmetric pool in this study following [44, 122]. Although some studies modelled the effect using a fourth pool [69, 102], it is still unclear how NOE might respond to Gd or be affected by the decrease of $T_{1w}$. This could modulate the $MTR_{asym}$, thus potentially explaining the variability in our results.

The differences of pre- and post-contrast z-spectra, and the estimated $T_{1w}$ reductions were found to be larger in the GM when compared to the WM both before and after surgery. This is because GM is normally more perfused than WM, leading to higher quantity of Gd in the former and thus a larger influence on $T_{1w}$. When comparing the differences of pre- and

post-contrast z-spectra, and the estimated $T_{1w}$ reductions before and after surgery, it was found that the differences and relaxation time reductions were greater after the surgery, most probably because the surgery would have increased the cerebral perfusion, leading to a higher residual of Gd in the post-contrast imaging.

In this study, data from 4 patients were analysed both before and after the surgery. Although the sample size was not big, significant differences in $MTR_{asym}$ pre- and post-Gd administration were found in WM at the group level and in 25% of the patient results. Variability between individuals may arise due to the differences in perfusion as well as Gd clearance. The lower consistency of the results in the GM may be caused by the practical difficulty in segmenting the pure GM pixels. If the most conservative Bonferroni correction defined as $\alpha/n$, where $\alpha$ is the significance level used - 5%, and $n$ is the number of samples - 16, were applied to rule out significant differences in individuals within the group that arise by chance, $p$ would need to be smaller than 0.0031. Using this more stringent $p$ value for the statistical tests, there were still two cases where significance would be found at the individual level.

Consequently, the potential influence of Gd should be carefully considered when designing clinical protocols involving the contrast agents and APT imaging. This may be especially important for brain tumour imaging since there is a likelihood of Gd uptake in the cerebral tissue due to blood brain barrier breakdown and in acute ischemic stroke assessment since Gd will be lower in regions of low perfusion resulting from the blockage. Thus, if APT images are acquired after Gd infusion in these clinical scenarios, interpretation of the APT effect using the widely used asymmetry measure would potentially be more complex, unless the $T_{1w}$ change can be properly accounted for which is not the scope of this work.

Besides causing a reduction in $T_{1w}$, Gd also affects the transverse relaxation time of the water protons, $T_{2w}$, but its effect is less marked compared to the effect on $T_{1w}$ [143]. A decrease in $T_{2w}$ broadens the linewidth of z-spectrum [43] and thus would affect the $MTR_{asym}$. However, the $T_{2w}$ change is unlikely to substantially influence the results obtained in this study because there is minimal change on the linewidth of the measured z-spectra which suggests that the decrease of $T_{2w}$ is negligible.

In this study, a single slice APT acquisition was used. Due to the patient movement between pre- and post-contrast APT scan and also differences in positioning before and after surgery, pixel-by-pixel comparison could not be performed to study the effect of residual Gd in the blood stream. Thus, the statistical evaluations had to be performed on the segmented GM and WM. It is likely that there will be spatial variations in the Gd effect on $T_{1w}$ and thus $MTR_{asym}$ due to local variations in perfusion as well as vascular topology.

## A3.5 Conclusion

This study suggests that $MTR_{asym}$ values after the passage of Gd do not necessarily match those observed pre-contrast even though by being an asymmetry measure, it might be assumed to be insensitive to changes in $T_{1w}$. For quantitative APT imaging, this implies that it will be better to acquire APT data prior to the contrast agent administration to avoid potential misinterpretation of the APT effect, for inter-subject comparison or follow-up study.

## A3.6 Supplementary Figures

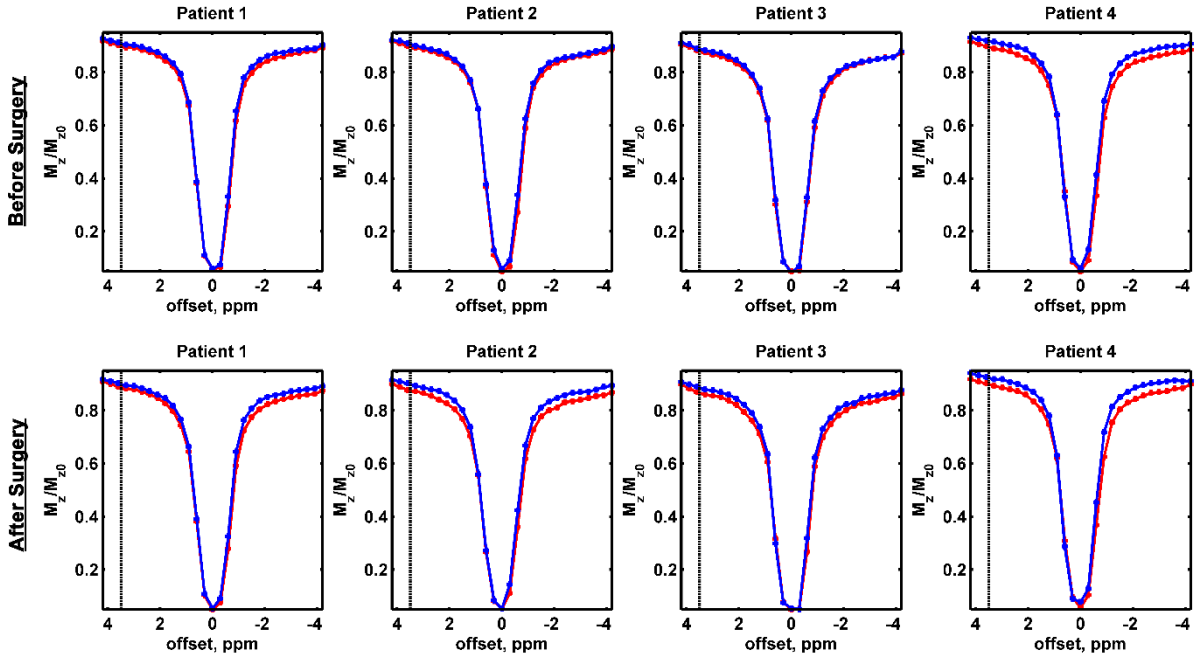


**Suppl. Figure A.1: Average measured z-spectra in GM of all the patients after water shift correction, where the red plots are the pre-contrast results and the blue plots are the post-contrast spectra. The differences between pre- and post-contrast are consistent with the simulation, where the decrease of water longitudinal relaxation time after Gd administration causes an increase in the magnitude of post-contrast measured signal.**

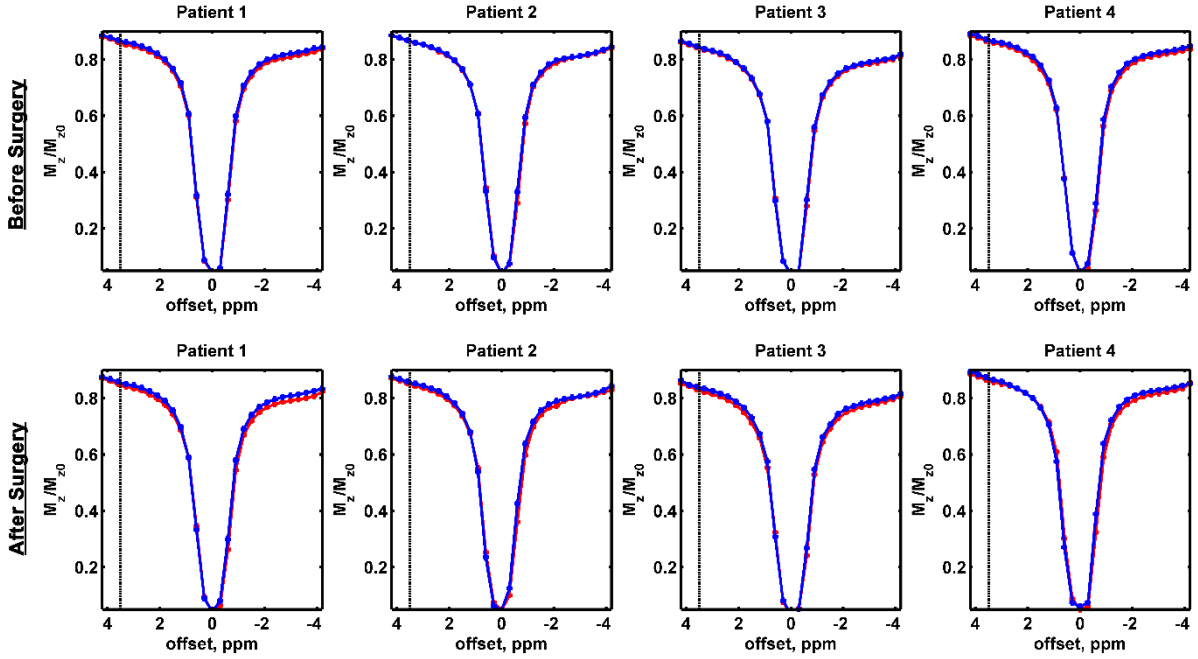


**Suppl. Figure A.2: Average measured z-spectra in WM of all the patients after water shift correction, where the red plots are the pre-contrast results and the blue plots are the post-contrast spectra. In general, the differences are in agreement with the simulation and GM but the magnitude of difference is smaller when compared to the change in GM.**